A METHOD FOR DIAGNOSIS OF MULTISTAGE FRACTURE TREATMENTS IN HORIZONTAL WELLS USING TEMPERATURE MODELING

A Dissertation

by

XINYANG LI

Submitted to the Office of Graduate and Professional Studies of
Texas A&M University
in partial fulfillment of the requirements for the degree of

DOCTOR OF PHILOSOPHY

Chair of Committee,	Ding Zhu
Co-Chair of Committee,	A. Daniel Hill
Committee Members,	Eduardo Gildin
	Charles J. Glover
Head of Department,	A. Daniel Hill

December 2016

Major Subject: Petroleum Engineering

ABSTRACT

Downhole temperature measured by distributed temperature sensors shows distinct response during multi-stage fracture treatments. A forward model is needed to interpret the measured dynamic temperature data during injection and shut-in of a well in complex flow systems to quantitatively diagnose fracturing treatments and characterize created fractures.

In this study, a forward thermal model predicting temperature distribution along a wellbore is established considering formation, wellbore, and fracture heat transfer. The fracture model can predict fracture propagation, fluid distribution, and fracture temperature based on mass and energy conservation equations. Temperature distribution in the reservoir can also be obtained by coupling a reservoir model with fracture model and wellbore model. For multi-stage fracture treatments, a sequential simulation method is applied by introducing real time control. Using the algorithm from single-stage treatment, a work flow for multi-stage fracture simulation is created by performing a single-stage stimulation, shutting in the stage, and moving along the wellbore to the next stage. Warm-up of the entrained fracturing fluid during shut-in periods is simulated by removing the fluid injection term and implementing different boundary conditions.

Due to the large temperature difference between the injection fluid and the surrounding formation, simulated results show temperature signal change occurs at fracture locations during the injection period. Warm-back behavior is also obvious at

fracture locations after shut-in the well. The effect of injection flowrate, fluid distribution, fluid properties, and reservoir characteristics on temperature behavior are investigated. At first initiation of the fracture, injection flowrate plays an important role on fracture half-length and leak-off front. Heat conduction is the dominant mechanism governing temperature response during shut-in. For a shale formation, the time to reach thermal equilibrium is on the order of weeks. Sensitivity of observed temperature to fluid distribution, and reservoir parameters in the simulation allow for fracture diagnosis using distributed temperature data during stimulation operations.

DEDICATION

Dedicated to my parents and Sufeng.

ACKNOWLEDGEMENTS

I would like to express my gratitude to my supervisors, Dr. Zhu and Dr. Hill for their support, guidance and encouragement throughout my graduate studies. They are my mentors not only in this research, in my future career also.

I also thank my committee members, Dr. Gildin, and Dr. Glover, for their precious advice and help throughout the course of this research.

Appreciation also go to my friends and colleagues, and the department faculty, and staff for making my time at Texas A&M University a great experience.

NOMENCLATURE

AC	Center spatial coefficient
AE	East spatial coefficient
AN	North spatial coefficient
AP	Local spatial coefficient
AS	South spatial coefficient
AW	West spatial coefficient
c	Injection fluid compressibility
C	Overall leak-off coefficient
C_c	Compressibility effect leak-off coefficient
C_{lk}	Average leak-off coefficient used in case studies
$\hat{C}_p$	Specific heat capacity per unit volume
$\hat{C}_{pf}$	Reservoir fluid heat capacity per unit volume
$\hat{C}_{pl}$	Injection fluid heat capacity per unit volume
$\hat{C}_{pr}$	Reservoir rock heat capacity per unit volume
C_{pcm}	Cement heat capacity
C_{pcs}	Casing heat capacity
C_v	Fluid viscosity effect leak-off coefficient
C_w	Wall building effect leak-off coefficient
e_r	Component of combined energy flux in r direction

e_x	Component of combined energy flux in *x* direction
e_y	Component of combined energy flux in *y* direction
e_z	Component of combined energy flux in *z* direction
$\boldsymbol{e}$	Combined energy flux vector
g	Gravitational constant
G	Green's function
h	Fracture height
h_l	Newton's cooling heat transfer coefficient
$\widehat{H}$	Enthalpy per unit volume
$\widehat{H}_r$	Reservoir rock enthalpy per unit volume
k	Reservoir permeability
K_{cm}	Cement thermal conductivity
K_{cs}	Casing thermal conductivity
K_e	Effective thermal conductivity
K_f	Reservoir fluid thermal conductivity
K_{JT}	Joule-Thomson coefficient
K_l	Injection fluid thermal conductivity
K_r	Reservoir rock thermal conductivity
m_w	Slope of the filtrate volume change with square root of time
N	Empirical constant
N_c	Number of clusters per stage

p	Pressure
ΔP	Pressure difference across fracture face
q	General fluid flow rate
q_{inj}	Injection flow rate
q_{inj_λ}	Injection flow rate at cluster λ
q_{lk}	Leak-off flow rate
$\boldsymbol{q}$	Energy source
Q_{inj}	Total injection flow rate per stage
$\dot{Q}\vert_{\ res-f}$	Energy source transferred from reservoir to fracture
R	Wellbore diameter
R_{cs}	Casing inner diameter
R_o	Hole inner diameter
R_{oca}	Casing outer diameter
s	Empirical constant
t	Time
t_{inj}	Injection time
Δt	Time step size
T	Wellbore temperature
T_D	Dimensionless temperature
$\widetilde{T_D}$	Dimensionless temperature in η domain

T_i	Reservoir initial geothermal temperature
T_{inj}	Injection fluid temperature
T_I	Reservoir and wellbore interface temperature
T_l	Injection fluid temperature in fracture
T_r	Reservoir temperature
U	Component of velocity vector
$\widehat{U}$	Total internal energy per unit volume
U_f	Reservoir fluid internal energy
$\widehat{U}_r$	Reservoir rock internal energy per unit volume
U_T	Overall heat transfer coefficient
v	Injection fluid velocity in wellbore
v_I	Injection fluid velocity into the fracture at perforation location
v_{lk}	Fluid-loss velocity
v_x	Fluid velocity in *x* direction
v_y	Fluid velocity in *y* direction
V	Component of velocity vector
$\hat{V}$	Unit volume
w	Average fracture width
W	Component of velocity vector
x	Fracture propagation direction
Δx	Grid block size in *x* direction

$x_{res/wb}$	x position at reservoir and wellbore interface
X_f	Fracture half-length
Y_{lk}	Fluid-loss front

Greek

α	A point in $(-\infty, \infty)$
β	Thermal expansion coefficient
γ	Pipe open ratio
$\delta(y)$	Singular initial data
η	Laplace transform domain
θ	Well inclination angle
μ_f	Fluid viscosity
$\boldsymbol{v}$	Velocity vector
ξ	Laplace transform variable
$\boldsymbol{\pi}$	Molecular stress tensor
ρ_{cm}	Cement density
ρ_{cs}	Casing density
ρ_f	Reservoir fluid density
ρ_l	Injection fluid density
ρ_r	Reservoir rock density
$\tau(x)$	Time for fracture to propagate to x
ϕ	Reservoir porosity

Subscripts

f	Reservoir fluid
i	Position index
I	Interface index
j	Position index
l	Injection fluid
m	Stage index
n	Time step index
N_x	Number of grid blocks in x direction
N_y	Number of grid blocks in y direction
res/wb	Reservoir and wellbore interface
λ	Cluster index

TABLE OF CONTENTS

Page

LIST OF FIGURES

Page

LIST OF TABLES

Page

1. INTRODUCTION

1.1 Background

Multistage hydraulic fracturing is one of the popular and key methods in horizontal wells to the success of unconventional oil and gas reservoirs. In past decades, techniques were designed to monitor and diagnose the effectiveness of fracture treatments and fractured well performance, such as fiber optic distributed sensing, non-radioactive tracers, and production logs. However, such techniques are limited and fracture stimulation analysis based on available techniques has large uncertainties. Complementary diagnostics can significantly reduce uncertainties of fracture stimulation analysis, help to calibrate fracture models, and improve completion design of multistage wells (Ugueto et al., 2014). Recently, the fiber optic distributed temperature sensor (DTS) has been widely used in fracture completion, and it allows us to observe real-time dynamic temperature profiles during fracture treatment. Temperature datum is being used along with other well information for fracture diagnostics (Sierra et al., 2008 and Huckabee, 2009), and it can provide insights on identifying fracture locations and flow rate profiling.

During the injection period for a hydraulic fracture treatment, cold fluids is injected into reservoir under high pressure. This causes cooling effect near the wellbore region that can be captured by DTS measurements. When fracture job is completed and the well is shut-in, warm back happens due to heat conduction from the surrounding formation. This involves complex physical processes, such as fracture initiation and propagation, fluid-loss into the formation, and energy exchange between the wellbore and

the formation. Temperature responses to the flow highly depend on these mechanisms. By using a forward thermal model, we can simulate the temperature distribution to identify fracture locations, to estimate the flow rate distribution, and to evaluate fractured well performance.

1.2 Literature Review

1.2.1 Multistage Hydraulic Fracture Stimulation Techniques

Unconventional oil and gas reservoirs are widespread throughout the United States, as shown in **Fig. 1.1**. Hydraulic fracturing becomes critical for taking advantage of these shale and tight reservoirs. Natural gas production has tremendously increased in the past decade mainly contributed by unconventional gas reservoirs, and is expected to continue to grow. This is largely related to the effectively use of multistage hydraulic fracturing technology and horizontal drilling. Multistage fracturing is a commonly used stimulation operation usually performed on low permeability formations. The complex formations and extreme conditions require several individual zones to be completed and fractured to access the entire horizontal interval. Multistage fracturing has offered one of the best solutions to save money and time in such complex reservoirs (Stanojcic et al., 2009).

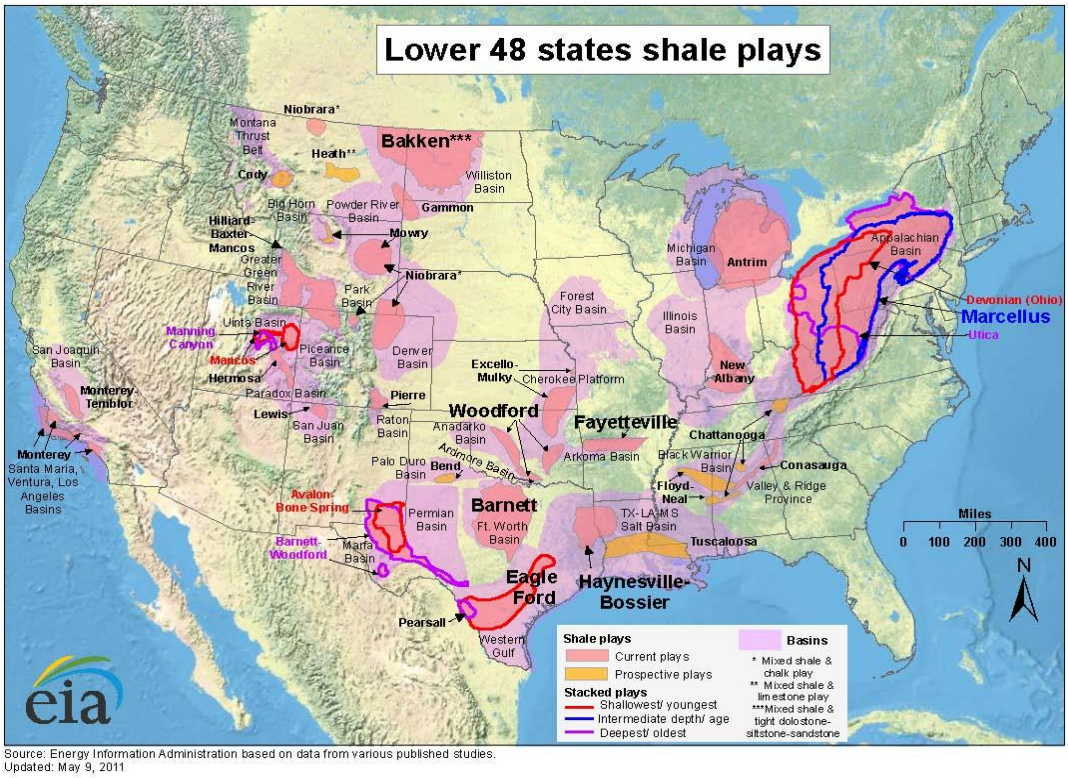

Source: Energy Information Administration based on data from various published studies.
Updated: May 9, 2011

Fig. 1.1 Shale plays in United States (Energy Information Administration)

There are several ways to perform multistage fracturing, such as perf-and plug, coiled tubing, and sliding-sleeve, which is selected depending on the well design and completions. It is also works in the opposite way, to best access the reservoir efficiently, companies are designing the well and selecting completion methods based on the multistage fracturing technique which fits the specific condition the best. **Figure 1.2** shows an example for perf-and plug multistage fracturing in a shale gas reservoir.

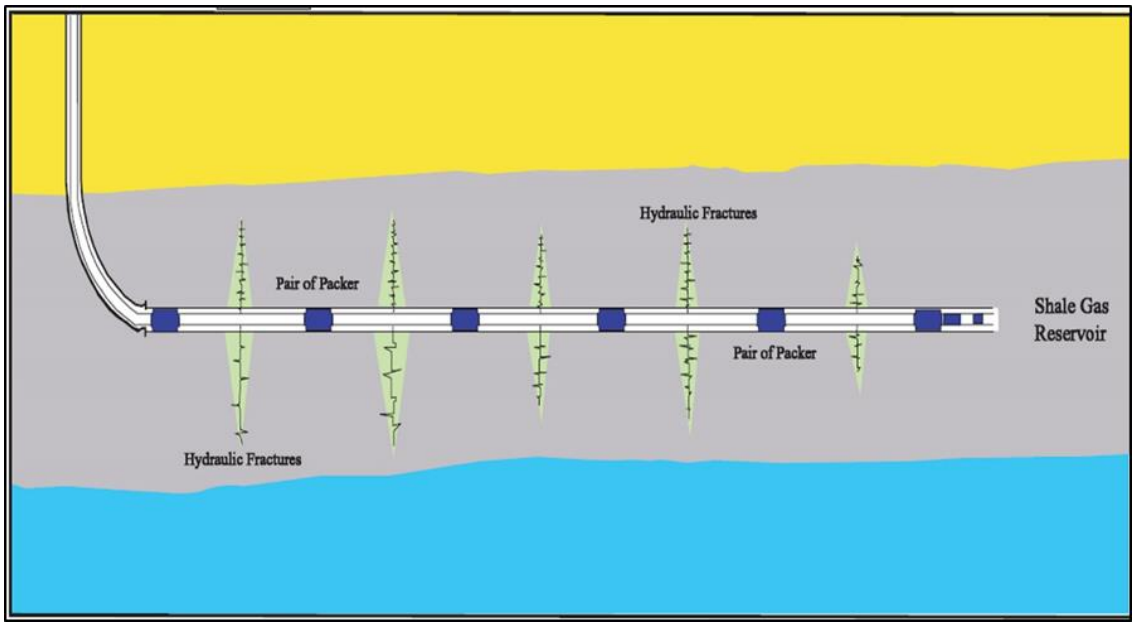

Fig. 1.2 Multistage hydraulic fracturing through different ports separated by pairs of packers (Abdulaziz, 2013)

1.2.2 Hydraulic Fracture Diagnostic Technologies

Since the first known commercial hydraulic fracturing operation done in 1949, the industry have tried to better understand and optimize hydraulic fracturing treatment. There are numerous fracture diagnostic technologies shows in **Table 1.1**. The ability and main limitation of each technique is also listed in the table. Indirect techniques include well testing, net pressure and production data analysis. While direct diagnosis near wellbore can provide a local measurement of the fracture at the wellbore, such as radioactive tracers, temperature, caliper and production logs, and borehole imaging. Mapping fractures with microseismics and tiltmeters are techniques that directly image the fracture from far field.

Table 1.1 Hydraulic fracture diagnostic technologies (Halliburton)

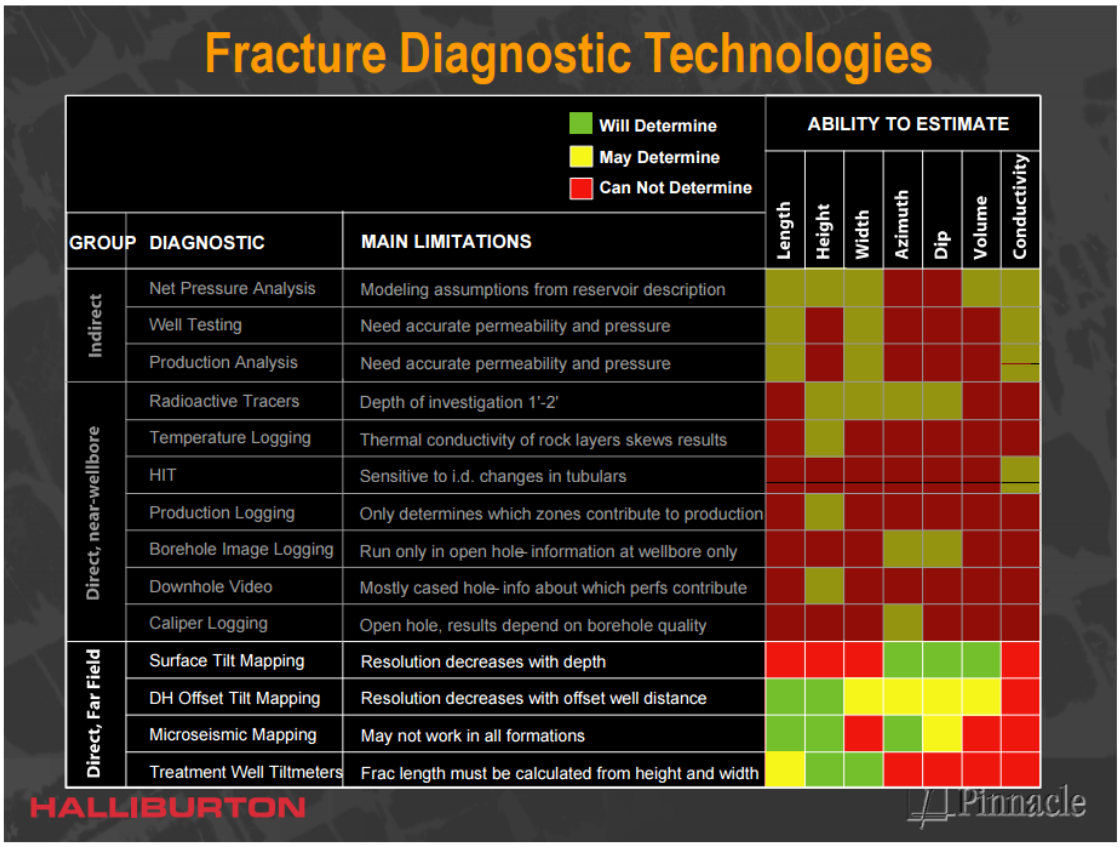

The following is a brief summary of the available diagnostic techniques, their capabilities and limitations.

Microseismic fracture mapping and downhole tiltmeter are far field techniques which can provide image and details about fractures orientation and dimensions by detecting induced microseisms and deformation. However, the limitation of these techniques is that they can only map the total extent of hydraulic fracture growth not the effective propped fracture length or conductivity. Additionally, the resolution will be affected by fracture treatment, reservoir properties and the distance to the detected wells.

The use of radioactive tracer and production logging have a long history in the oil industry. However, sometimes the test is expensive to run in horizontal wells and also rarely provides truly useful information.

In addition to the direct measurement techniques listed above, indirect fracture diagnosis is done by production data analysis and pressure transient analysis. These indirect techniques sometimes provide useful information by reservoir simulation, however, the drawback with such analysis is that there is a possibility of non-unique solutions. In other words, for example, there might be multiple fracture models with totally different fracture characteristics give the same production and pressure data. Therefore, calibration of reservoir and fracture models is required.

Recently, fiber optic distributed pressure and temperature sensors have been applied as a complementary tool to well logs for real-time fracture diagnostics. This technology not only offers continuous real-time monitoring for the entire wellbore which enables one to observe data profile during the hydraulic fracture treatment, it is also more affordable compared to fracture mapping techniques. DTS enables one to estimate the fracture initiation depth, vertical coverage, number of fractures generated, effects of diverting agents and undesired flow behind casing (Sierra et al., 2008). DTS measures dynamic temperature profile along the wellbore during multistage hydraulic fracturing treatments. One of the advantages is that DTS data acquisition systems generally do not interfere with flow. Compared to production logging tools, DTS is more flexible and can be used for both short-term and long-term scenarios (Johnson et al., 2006). Sierra et al. (2008) and Huckabee et al. (2009) used DTS data in several field applications to diagnose

hydraulic fracture stimulation and evaluate well performance. Molenaar et al. (2012) presented different horizontal well cases to illustrate how the combination of distributed temperature sensing and distributed acoustic sensing has potential to enhance the monitoring, assessment, and optimization of openhole and limited entry designed hydraulic fracture stimulation treatments. Holley et al. (2012) coupled fracture-treatment responses and openhole log characteristics with the near-wellbore DTS data during pumping, and during warm back to perform an integrated assessment of the stimulation effectiveness and efficiency. In the study, he also stated that DTS offers a real time monitoring for identifying, quantifying, and evaluating the near wellbore fracture geometry, the fracturing-fluid distribution, and overall stimulation effectiveness. Ugueto et al. (2014) evaluated the efficiency of hydraulic fracture simulation treatments by using DTS data considering both near-wellbore and far-field diagnostics. Later on, Ugueto et al. (2015) reviewed examples from multiple wells where fiber optics has been used to gain a better understanding of three highly debated fracture simulation distribution topics: diversion, stage isolation and overflushing.

Figure 1.3 (Ugueto, 2016) shows an example of an integrated display of three time-synchronized annotated panels for fiber optic distributed acoustic sensing (DAS), distributed temperature sensing (DTS), and hydraulic fracture stimulation (HFS) treatment data respectively for a single cemented plug and perforated stage. Warmer colors in the DAS color map on top represent higher acoustic energies corresponding to fluid and proppant distribution during treatment. Cooler colors in DTS map represent lower temperatures associated with the injection of stimulation fluid. These plots indicate that

the DAS and DTS data can provide valuable information of pressure and fluid distribution during fracturing treatment. Therefore, a thermal model predicting temperature distribution along the wellbore is essential to use the technology quantitatively diagnose the treatment.

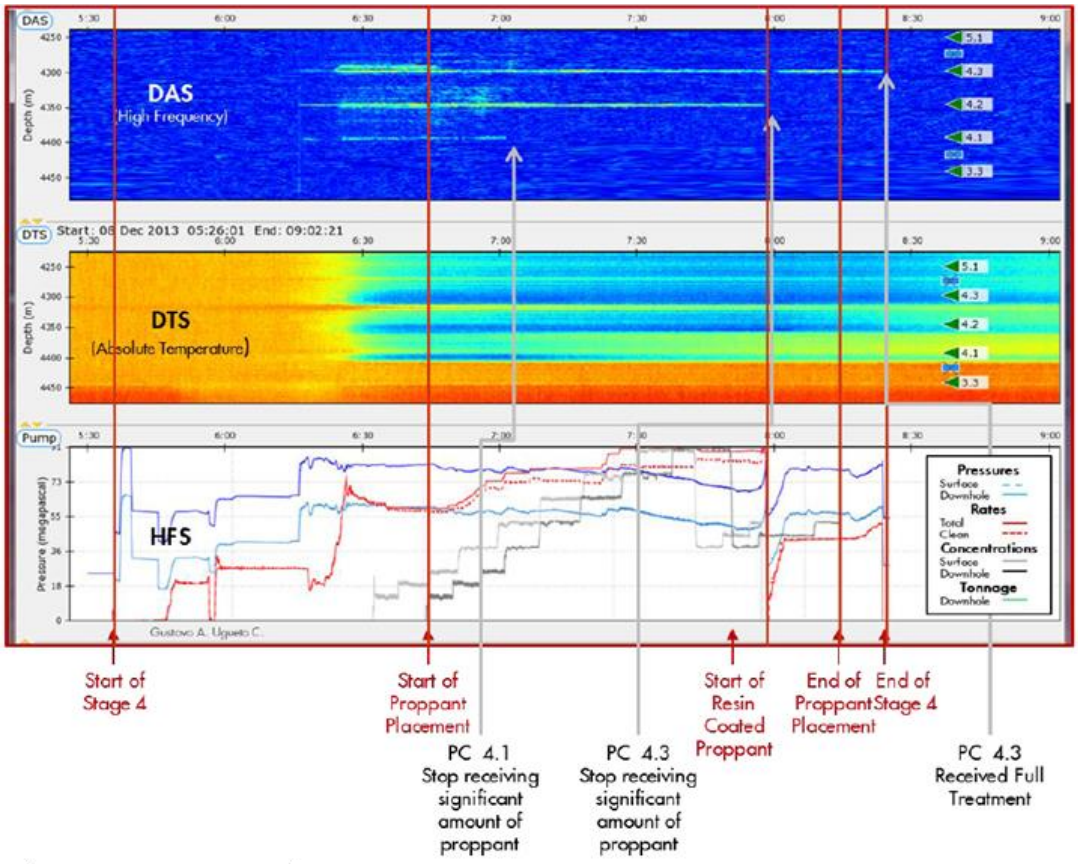

Fig. 1.3 Fracture monitoring using fiber optic DAS and DTS (Ugueto, 2016)

Tracer, temperature, and other near-wellbore diagnostics can pin-point fluid entry into the fracture and determine open perforation during each phase of the treatment. A modeling process is necessary to take this knowledge as a first constraint to obtain a

complete picture of the fracture growth and geometry (Cipolla et al., 2000 and Barree et al., 2002). With the combination of diagnostic technologies and modeling, the integrated approach can be used to prepare for fracture design. Calibration may be needed when using far field mapping, together with well logging, and reservoir information to optimize stimulation process. Integrated fracture diagnostics approach is showed in **Fig. 1.4** (Ugueto et al., 2014). Understanding the fracturing process properly can help us to optimize individual fracture treatment to obtain optimum interval coverage, and to optimize the entire field development in terms of well spacing and location.

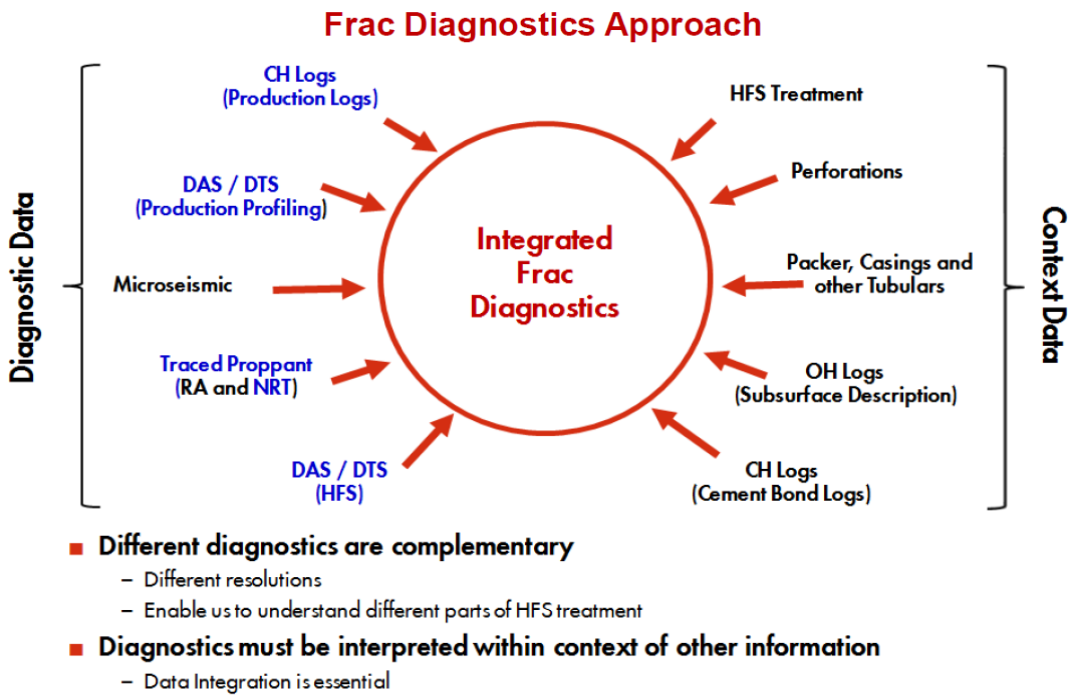

Fig. 1.4 Integrated fracture diagnostics approach (Ugueto et al., 2014)

1.2.3 Hydraulic Fracture Propagation Models

Fracture geometry is difficult to obtain with fracture growing thousands of feet deep in heterogeneous formation which normally has complex stress field. Based on the above discussion for fracture diagnostic techniques, we already know that it has to be combined with proper fracture modeling to truly understand the fracture geometry and conductivity. Shortly after fracturing technology was implemented, researchers started working on developing fracture propagation models.

Howard and Fast (1957) proposed a 2-D mathematical model to simulate fracture propagation incorporating the Carter Equation II. They assumed a constant fracture width and computed the fracture area based on fracturing fluid flow and leak-off to the formation. Two well-known fracture models were presented: Perkins-Kern-Nordgren (PKN) (Perkins and Kern, 1961; Nordgren, 1972) and Kristonovich-Geertsma-de Klerk (KGD) (Khristianovitch and Zheltov, 1955; Geertsma and de Klerk, 1969). The two models were commonly used for designing a fracture to have a length much greater than the fracture height or a fracture height that is more than the fracture length respectively.

A radial or penny-shaped fracture will be created when relatively small fracture treatments are applied in thick reservoirs, or in formations with little stress contract between layers to retard the vertical fracture growth. Valko and Economides (1995) extended the work of Nordgren (1972) and recommended an improved expression for the fracture width at the wellbore. Later on, pseudo-three-dimensional (P3D) models are proposed in order to idealize fracture growth in multi-layered formations (Simonson et al., 1978; Settari and Cleary, 1986; Warpinski and Smith, 1989). Meyer (1986) presented both

analytical and numerical solutions for 2-D and 3-D hydraulic fractures growth using Perkins-Kern-Nordgren and Kristonovich-Geertsma-de Klerk models. Recently, many commercial software has been developed considering a fully 3-D fracture model with coupled 2-D fluid flow to predict 3-D space fracture growth. These models are developed based on linear elastic fracture mechanics coupling with complex fluid flow patterns inside fractures (Hossain, 2001).

Fracture can propagate laterally and vertically, and change original planes, depending on induced perforation, well deviation, local stress distribution, rock properties and the presence of natural fractures (Economides et al., 1994; Hossain, 2001). The fracture propagation model in this study is simplified to reduce uncertain parameters for the forward model to be able to investigate fluid profiling using DTS measured temperature data. The assumptions made to develop the fracture propagation model are reasonable, and the model is proved to be sufficient to study temperature behavior near wellbore. In return, the study of DTS data can provide a first constraint for further hydraulic fracture propagation modeling.

1.2.4 Temperature Modeling and Interpretations

Wellbore and formation heat transfer modeling is one of the most important tasks in oil and gas industry since it has been identified to be helpful. Specifically, with the downhole temperature measurement technique developing rapidly, people started to try to interpret well performance and optimize fracture treatment design from direct monitored temperature data. Compare to pressure and other measured data, temperature is more reliable for the reason of there are no restrictions with temperature for different flow

conditions. In the past, there are many researchers devoted efforts to the thermal modeling of the wellbore, formation and fracture, thus, several temperature models have been developed.

One of the earliest temperature models was presented by Ramey (1962) to predict temperature profiles as a function of time and depth for vertical wells by considering single phase fluid flow. In his work, he assumed that heat conducted to the surrounding formation is transient, while the heat transfer in the wellbore is steady state. Later on, Satter (1965) modified Raney's model by considering phase changes during steam-injection. Sagar (1991) extended Ramey's model to multiphase flow in inclined wells. Others (Holst and Flock, 1966; Willhite, 1967; Farouq Ali, 1981; Griston and Willhite, 1987; Alves et al. 1992) also attempted to improve Ramey's model by limited assumptions. Among these works, Hagoort (2004) improved Ramey's model and provided solutions without assuming wellbore heat accumulation is negligible.

Yoshioka et al. (2005) presented methods to interpret measurements for complex wells by using downhole pressure and temperature sensor data. A steady state wellbore model has been developed for a horizontal well coupled with reservoir thermal model to predict temperature and pressure along the wellbore. Ouyang et al. (2006) developed a numerical model to obtain flow profile in horizontal wells by using downhole measurements. Ouyang's study presented single-phase production flow profile in lateral wells and vertical wells by interpreting DTS data. However, extra information is needed for estimation of the multiphase flow profile. Pinzon et al. (2007) also built a wellbore and reservoir coupled thermal model to interpret DTS data. Li et al. (2010) established a

forward model for wellbore and reservoir temperature simulation using downhole pressure and temperature data in order to solve for flow profile in a horizontal well. In Li's study, Yoshioka's wellbore model was combined with a 3-D multiphase reservoir thermal model. The wellbore flow profile then can be obtained by inversely interpreting the pressure and temperature data using the forward model.

In addition to the steady state wellbore thermal models, Hasan and Kabir (1991) contributed to wellbore thermal model by proposing early-time transient temperature behavior of fluid flow in the wellbore and adopting appropriate boundary condition between the formation and the wellbore. They also applied superposition principle to account for the gradual changes in heat transfer rate between the wellbore and the formation with respect to time. In the following years, Hasan and Kabir further modified wellbore thermal model for multiphase fluid flow in the wellbore and showed more application cases (Hasan and Kabir, 2010). Maubeuge et al. (1994a and 1994b) developed a numerical thermal model for the reservoir to solve for the transient temperature profile considering small thermal effects, such as Joule-Thomson effect and viscous dissipation. Duru and Horne (2008) and Sui (2008) proposed a transient wellbore thermal model as well as a transient reservoir thermal model. Sui also showed that the transient wellbore thermal model can be reduced to a steady state wellbore model if observed time is long enough, for example, days (Sui, 2009). Bahonar et al. (2010) presented a numerical non-isothermal two-phase wellbore simulator coupled with tubular, cement material, and surrounding formation. He compared this model with other five models for formation

temperature simulation. With the validation against field data, he showed the model's merits in predicting casing temperature.

Besides the development of thermal models in the wellbore and formation during transient and steady state period, fracturing fluid temperature inside various shape of fractures is also studied by researchers for many years, even though actual fracture temperature distribution is difficult to measure directly. Wheeler (1969) has presented analytical solutions considering convection heat transfer along the fracture, as well as conduction and convection of heat into the formation. Kamphuis et al. (1993) developed a temperature model within the fracture by calculating the heat transfer between the fracture and the formation. Meyer (1989) proposed analytical solutions of thermal models in PKN and KGD fractures coupled 2-D fracturing fluid flow. Schechter showed less rigorous approach to readily solve the temperature distribution for various fracture geometries, such as 1-D propagation of rectangular and penny shape fractures (Schechter, 1992). He considered constant injection fluid temperature and reservoir initial temperature as boundary conditions and constant fracture width. Seth et al. (2010) developed a fracture model for interpreting DTS data near perforation locations for a single fracture in vertical wells during fracture propagation and after shut-in the well. Recently, a 3-D thermal model for hydraulic fracturing is developed by Amini et al. (2015) to determine the temperature profile in and around the fracture based on a pseudo 3-D fracture propagation model. They concluded that the location of optical fiber cable is very important in DTS temperature measurement based on the simulated result of case study. Sierra et al. (2008) also

presented an analysis of the impact of fiber optic location on the temperature response based on DTS data in hydraulic fracturing.

Based on these previous works on thermal modeling of wellbore, formation and fracture respectively, thermal behavior is better understood. However, it is still very challenging to have a comprehensive thermal model to consider heat transfer between the fracture, the formation, and the wellbore during fracturing treatment to provide better optimization of fracture design and estimate the entire fractured wellbore performance, especially for multistage fracture treatments in horizontal wells. Yoshida et al. (2013) developed numerical flow and thermal models for horizontal wells with transverse fractures which have fixed geometry. Cui et al. (2014) presented a semi-analytical model to predict temperature and pressure behavior in a multiple-fractured horizontal well during production.

However, there is lack of complimentary studies focusing on quantitative temperature interpretation during the fracturing process, shut-in period and initial flow back in multistage fractured horizontal wells. Huckabee (2009) reviewed the applications of optic fiber temperature sensing technology for hydraulic fracturing that are used in stimulation diagnostics and well performance evaluation to demonstrate quantitative inflow distribution measurement. Both vertical and horizontal wells examples are included in the study. Tabatabaei (2011) presented a thermal model to simulate the temperature behavior along the wellbore during multiple hydraulic fracturing treatment as well as during the shut-in period with a fixed fracture geometry. Hoang et al. (2011) established a model for interpreting DTS data during hydraulic fracturing in a vertical well with

limited entry and a known fracture geometry. Ribeiro and Horne (2013) developed a comprehensive model to account for the pressure on the temperature response, as well as a dynamic fracture growth during and immediately after hydraulic fracturing in vertical wells. Later in 2014, they extended this model to detect fracture growth out of zone in multistage fractured horizontal well. In their study, a steady state well thermal model developed by Yoshioka (2007) is adopted.

1.3 Objective and Approach

Although numerous wellbore and fracture thermal models have been developed inspired by the development of DTS techniques, the temperature behavior in multistage fractured horizontal wells is not fully understood yet, especially during the fracturing treatment. The objective of this study is to establish a forward model for transient temperature data interpretation during multistage hydraulic fracturing treatments in horizontal wells. In the proposed study, a forward thermal model predicting temperature distribution along the wellbore is established considering reservoir, wellbore, and fracture heat transfer. The forward model can be used to simulate temperature profile with respect to real time during multistage fracturing treatments. It is accomplished by the following approaches:

(1) A single-phase wellbore flow model developed by Yoshika (2007) and a transient horizontal wellbore thermal model presented by Sui (2009) are adopted here to couple with the reservoir and fracture thermal model to estimate near wellbore temperature change during fracturing treatment.

(2) For a single-stage fracture treatment, a numerical fracture propagation model based on mass balance approach is used to predict the fracture growth and fluid distribution for a single traverse fracture in a horizontal well during injection.

(3) 2-D fracture and reservoir thermal models are developed and solved simultaneously, both of which are based on the energy conservation equation to calculate the fracturing fluid temperature profile inside the fracture, as well as the heat transfer in the formation at any time during treatment, including injection and shut-in of the well.

(4) A sequential simulation method is then applied for multistage fracture treatments by introducing real time control. Warm-up of the entrained fracture fluid during shut-in periods is simulated while other stages are run by removing the fluid injection term and implementing different boundary conditions.

This study is presented in six chapters. The literature review on related subjects and research objective and approach are discussed in Chapter 1. In chapter 2, the integrated forward thermal model is developed with assumptions. Chapter 3 shows the numerical solutions of the integrated forward model. Chapter 4 presents the forward model validation with analytical solutions and reservoir simulation results. In Chapter 5, case studies are proposed, and investigation of temperature sensitivity to various fluid distribution, reservoir properties and fracture parameters are also discussed. Last but not least, we draw conclusions based on results and discussions in Chapter 6.

2. FORWARD MODEL

2.1 Introduction

In this chapter, a coupled forward model is established to predict transient temperature behavior along the wellbore during multistage fracturing treatments. This forward model consists of a wellbore model, a fracture model, and a reservoir model, as shown in **Fig. 2.1**.

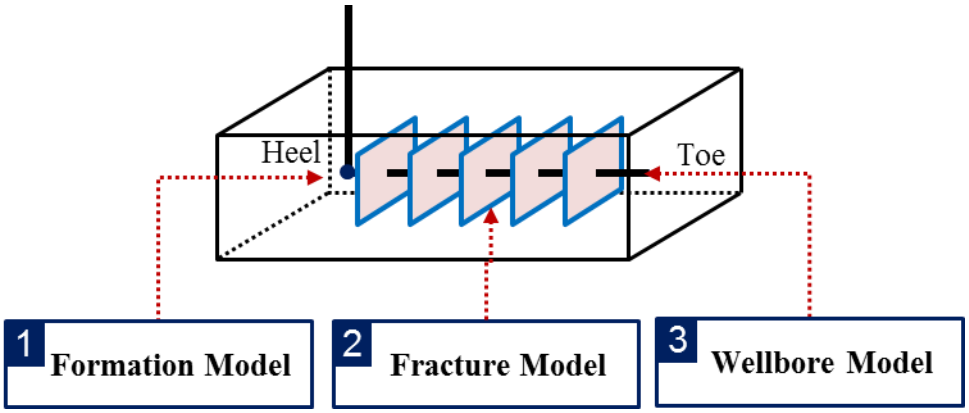

Fig. 2.1 Schematic of the forward model

The fracture model includes fracture flow model and fracture thermal model. The fracture flow model is developed based on mass conservation equation and it allows one to predict the fracture half-length and injection fluid distribution. The fracture thermal model is formulated by energy conservation equation and solved by coupling the wellbore and reservoir thermal model with applying proper boundary conditions at perforation locations and the fracture/formation interface during injection and shut-in.

Reservoir flow model considers fracturing fluid leaks off through fracture faces into the formation, and the leak-off front is calculated. The 2-D reservoir thermal model is also derived based on the energy conservation equation.

The single-phase wellbore flow model developed by Yoshioka (2007) and the transient wellbore thermal model presented by Sui (2009) are adopted directly. During injection periods, the wellbore is assumed to have the same temperature as injection fluid, and the wellbore fluid temperature increases during shut-in because of heat conduction from the surrounding reservoir which has higher temperature.

The wellbore, reservoir and fracture model are coupled by introducing appropriate boundary conditions. For multistage fracture treatments, the wellbore model is coupled with the fracture and reservoir model sequentially for each stage due to the stage isolation. A fully implicit finite difference method is used to solve the mass and energy conservation equations which is discussed in Chapter 3.

The fluid flow directions during fracture stimulation in a horizontal well with single fracture in Cartesian coordinate is shown in **Fig. 2.2**.

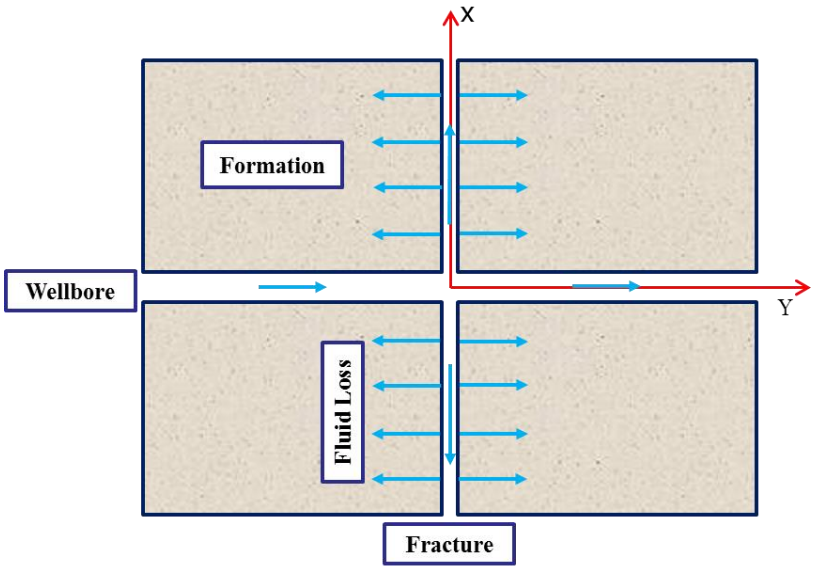

Fig. 2.2 Top view of flow directions during single fracture propagation

2.2 Wellbore Model

The single-phase wellbore flow model presented by Yoshioka (2007) is adopted. And the transient wellbore thermal model developed by Sui (2009) is also adopted here to describe transient temperature behavior and provide information to update reservoir and fracture temperature. A wellbore differential volume element is shown in **Fig. 2.3**.

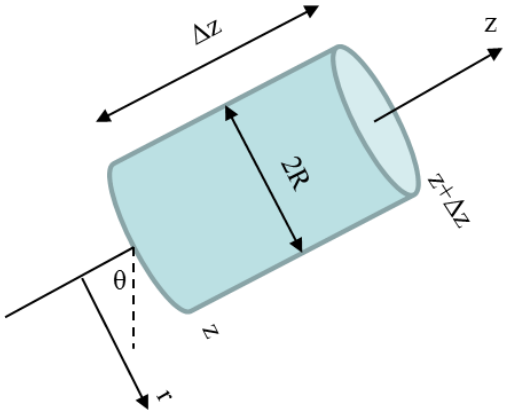

Fig. 2.3 A differential volume element in the wellbore

2.2.1 Wellbore Flow Model

The mass conservation equation proposed by Yoshioka (2007) during production period is,

$$\frac{\partial \rho_f}{\partial t} = \frac{2\gamma}{R}\rho_I v_I - \frac{\partial \rho_f v}{\partial y} \tag{2.1}$$

Where, ρ_f is the reservoir fluid density in the wellbore, t is injection time, R is the wellbore or casing radius, ρ_I and v_I are the density and the velocity of fluid flowing into the wellbore from the fracture. v is the fluid velocity in the wellbore. γ is the pipe open ratio. When generating wellbore grids, the location where existing a fracture is taken as one grid, and for this grid, γ = 1, for other grids γ = 0.

Assume incompressible fracturing fluid is used. Additionally, this study is focusing on fracturing treatment, thus, the direction of v_I is inverse of the production process, ρ_I equals to the injection fluid density ρ_l in the wellbore. Therefore, the mass balance equation during injection process becomes to,

$$0 = \frac{2\gamma}{R} v_I - \frac{\partial v}{\partial y} \tag{2.2}$$

In which, v_I is the injection fluid velocity flows into the fracture at the perforation location which is calculated by the wellbore flow model and used as input in the fracture flow model.

The initial and boundary conditions applied to solve for the wellbore flow model are,

$$I.C. \quad v_I = v = 0, \quad at\ t = 0 \tag{2.3}$$

$$B.C.s \quad \begin{cases} v_I = 0, & at\ \gamma = 0 \\ v_I \neq 0, & at\ \gamma = 1 \end{cases} \tag{2.4}$$

For multi-stage fracturing treatment, there are normally multiple clusters in each stage. The total injection flow rate in the wellbore at each stage can be expressed as,

$$Q_{inj} = \sum_{\lambda=1}^{N_c} q_{inj,\lambda} \tag{2.5}$$

Where, N_c is number of clusters at each stage, assuming single perforation/fracture per cluster. And q_{inj_k} is the injection flow rate at cluster λ. For simplicity, the injection rate at each stage and each fracture is represented by q under specific condition. Multiple fractures within the same stage are created simultaneously, and fractures in different stages are created consecutively.

2.2.2 Wellbore Thermal Model

Energy conservation over a wellbore volume element can be described as the following equation,

$$\begin{bmatrix} Increasing \\ rate \\ of\ energy \end{bmatrix} = \begin{bmatrix} rate\ of \\ energy\ in \end{bmatrix} - \begin{bmatrix} rate\ of \\ energy\ out \end{bmatrix} + \begin{bmatrix} rate\ of \\ work\ done\ by \\ external\ forces \end{bmatrix} + [source] \tag{2.6}$$

The summation of energy transported by the convective mechanism, the work done, and the heat transported by molecular mechanisms equals to the total increasing energy. The energy balance equation is derived based on the combined energy flux vector **e**, which is defined as (Bird et al., 2002),

$$\boldsymbol{e} = \left(\frac{1}{2}\rho v^2 + \rho\widehat{U}\right)\boldsymbol{V} + [\boldsymbol{\pi}\cdot\boldsymbol{V}] + \boldsymbol{q} \tag{2.7}$$

Where, $\frac{1}{2}\rho v^2$ is the kinetic energy per unit volume, $\rho\widehat{U}$ is the internal energy per unit volume, $[\boldsymbol{\pi}\cdot\boldsymbol{V}]$ represents the energy transported by molecular mechanisms, in which $\boldsymbol{\pi}$ denotes the molecular stress tensor, $\boldsymbol{q}$ means the energy source transported into the system.

Accordingly, Eq. (2.6) can be expressed as,

$$\begin{aligned} \pi R^2 \Delta z \frac{\partial}{\partial t}\left(\frac{1}{2}\rho v^2 + \rho\widehat{U}\right) \\ = 2\pi R \Delta z (e_r)_R + \pi R^2 (e_z)_z - \pi R^2 (e_z)_{z+\Delta z} \\ - \pi R^2 \Delta z \rho v g \sin\theta \end{aligned} \tag{2.8}$$

The final form of the transient wellbore thermal model presented by Sui (2009) is,

$$\frac{1}{v}\frac{\partial T}{\partial t} - \frac{\beta T}{\rho v \hat{C}_p}\frac{\partial p}{\partial t}$$

$$= \frac{2\gamma}{R}\frac{\rho_I v_I}{\rho v}(T_I - T) + \frac{2(1-\gamma)}{R\rho v \hat{C}_p} U_T\left(T_r|_{\ r=r_w} - T\right) \qquad (2.9)$$

$$- \frac{\partial T}{\partial z} + K_{JT}\frac{\partial p}{\partial z} - \frac{g\sin\theta}{\hat{C}_p}$$

Where, β is the thermal expansion coefficient and $\hat{C}_p$ is the fluid heat capacity, and K_{JT} is the Joule-Thomson coefficient. The derivation details from Eq. (2.8) to Eq. (2.9) can be found in Sui's work (2009).

In this study, z, which along the well flow direction is equivalent as y coordinate, and r falls in x direction in a 2-D flow system. Moreover, for water based injection fluid, the thermal expansion and Joule-Thomson effect can be neglected. Hence, we can rewrite Eq. (2.9) as the following expression in this specific case,

$$\frac{1}{v}\frac{\partial T}{\partial t} = \frac{2\gamma}{R}\frac{\rho_I v_I}{\rho v}(T_I - T) + \frac{2(1-\gamma)}{R\rho v \hat{C}_p} U_T(T_r - T) - \frac{\partial T}{\partial y} - \frac{g\sin\theta}{\hat{C}_p} \qquad (2.10)$$

Where, T_r represents the reservoir temperature and is calculated by reservoir thermal model.

The initial and boundary conditions are,

$$I.C. \qquad T = T_{inj}, \qquad at\ t = 0 \qquad (2.11)$$

$$B.C.s \quad \begin{cases} T = T_{inj}, & at\ x = 0, t \le t_{inj} \\ K_e \dfrac{\partial T_r}{\partial x} = U_T(T_r - T), & at\ x = x_{res/wb} \end{cases} \qquad (2.12)$$

2.3 Fracture Model

The fracture flow model and fracture thermal model presented here are derived based on mass and energy conservation equations for a single fracture in horizontal wells. Over a differential volume element showing in **Fig. 2.4**, the continuity equation and general energy balance equation are derived in the following.

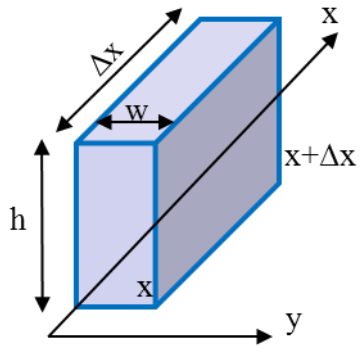

Fig. 2.4 A differential volume element in the fracture

2.3.1 Fracture Flow Model

For simplicity, assumptions have been made to the fracture geometry in order to reduce uncertain parameters in the complex flow system. The fracture is assumed to have uniform width and height and is propagating in *x* direction. In addition to this, the following assumptions are also made to model the fracture propagating process.

(1) Fluid-loss is linearly perpendicular to fracture faces and happens at fracture faces.

(2) The fracture has an infinite conductivity during injection.

(3) Fracturing fluid is incompressible.

The mass conservation can be expressed as,

$$\begin{bmatrix} Mass \\ increasing \\ rate \end{bmatrix} = \begin{bmatrix} Rate\ of \\ Mass \\ in \end{bmatrix} - \begin{bmatrix} Rate\ of \\ Mass \\ out \end{bmatrix} \tag{2.13}$$

Which in terms of fluid entering into the differential volume element, the mass balance equation can be written as,

$$2wh\frac{dX_f}{dt} = q_{inj}(x,t) - q_{lk}(x,t) \tag{2.14}$$

Where, q_{inj} is the volumetric flow rate flows into the element, X_f is the fracture half-length and q_{lk} is the volumetric leak-off flow rate flows out of the element. This equation shows that the fracture volume growing depends on the injection flow rate and leak-off amount.

The overall fluid-loss per unit time can be calculated by integrating the fluid-loss velocity over the leaks-off area. In this case it is convenient to use an average fluid-loss velocity instead of the local value. The fluid-loss velocity depends on both time and position in accordance with the equation (Schechter, 1992),

$$v_{lk} = \frac{C}{\sqrt{t - \tau(x)}} \tag{2.15}$$

Where, $\tau(x)$ is the time for facture to propagate to a distance *x*, after which fluid-loss starts. C is the overall fluid-loss coefficient considering fluid compressibility effect C_c, fluid viscosity effect C_v, and wall building effect C_w and can be calculated as,

$$C = \frac{-\frac{1}{C_c} + \sqrt{\frac{1}{C_c^2} + 4(\frac{1}{C_v^2} + \frac{1}{C_w^2})}}{2(\frac{1}{C_v^2} + \frac{1}{C_w^2})} \tag{2.16}$$

Where, C_c, C_v and C_w can be calculated by,

$$C_c = \sqrt{\frac{\phi c k}{\pi \mu}} \Delta P \tag{2.17}$$

$$C_v = \sqrt{\frac{\phi k}{2\mu}} (\Delta P)^{\frac{1}{2}} \tag{2.18}$$

And,

$$C_w = \frac{m_w}{2} \tag{2.19}$$

In which, ϕ is reservoir porosity, c is the fluid compressibility, μ is fluid viscosity, k is reservoir permeability, ΔP is the differential pressure and m_w is the slope of the filtrate volume through change with respect to square root of time.

Thus, by substituting Eq. (2.15), we can rewrite Eq. (2.14) as,

$$2wh\frac{dX_f}{dt} = whv_x(x,t) - 2h\int_0^{2X_f(t)} \frac{C(t)}{\sqrt{t-\tau(x)}} dx \tag{2.20}$$

The initial and boundary conditions are,

$$I.C.\ \ X_f = 0, \qquad at\ t = 0 \tag{2.21}$$

$$B.C. \begin{cases} v_x = v_I, & at\ x = R, t \le t_{inj}, \gamma = 1 \\ X_f = Const, & at\ t > t_{inj} \end{cases} \tag{2.22}$$

In which, t_{inj} is the injection time and the fracture half-length remains constant during shut-in. The discretized form of Eq. (2.20) is shown in Chapter 3 and finite difference approach is used to solve for fracturing fluid velocity and fracture half-length.

2.3.2 Fracture Thermal Model

The fracture thermal model is developed to calculate fracturing fluid temperature distribution in fracture during fracture propagation and shut-in. Conservation of energy is considered similarly as the fracture flow model over a differential volume element.

$$\begin{bmatrix} Accumulation \\ rate\ of\ energy \end{bmatrix} = \begin{bmatrix} Rate\ of \\ energy \\ in \end{bmatrix} - \begin{bmatrix} Rate\ of \\ energy \\ out \end{bmatrix} + [Source] \tag{2.23}$$

The energy balance equation is derived based on the combined energy flux vector **e**, which is defined the same as Eq. (2.7).

The accumulation rate of energy within the differential volume element is,

$$\begin{bmatrix} Accumulation \\ rate\ of\ energy \end{bmatrix} = wh\Delta x \frac{\partial}{\partial t}\left(\frac{1}{2}\rho v^2 + \rho \widehat{U}\right) \tag{2.24}$$

The rate of energy transport into the system is described as,

$$\begin{bmatrix} Rate\ of \\ energy\ in \end{bmatrix} = wh(e_x)_x + h\Delta x\left(e_y\right)_y \tag{2.25}$$

Similarly, the rate of energy transport out of the system is described as,

$$\begin{bmatrix} Rate\ of \\ energy\ out \end{bmatrix} = wh(e_x)_{x+\Delta x} + h\Delta x\left(e_y\right)_{y+\Delta y} \tag{2.26}$$

The heat transfer between the fracture and the reservoir at the fracture face is considered as a source term,

$$[Source] = \dot{Q}|_{\ res-f} \tag{2.27}$$

Thus, Eq. (2.23) can be rewritten in terms of energy flux vector ***e*** as the following,

$$wh\Delta x\frac{\partial}{\partial t}\left(\frac{1}{2}\rho v^2+\rho\widehat{U}\right)$$

$$=wh(e_x)_x-wh(e_x)_{x+\Delta x}+2h\Delta x\left(e_y\right)_y \tag{2.28}$$

$$-2h\Delta x\left(e_y\right)_{y+\Delta y}+2h\Delta x\dot{Q}|_{\ res-f}$$

Where, " 2 " comes from the two symmetrical fracture faces.

From the definition of internal energy and enthalpy for single phase incompressible fracturing fluid, we have,

$$\widehat{U}=\widehat{H}-\frac{p}{\rho} \tag{2.29}$$

And,

$$d\widehat{H}=\left(\frac{\partial\widehat{H}}{\partial T}\right)_p dT+\left(\frac{\partial\widehat{H}}{\partial p}\right)_T dp=\hat{C}_p dT+\left[\widehat{V}-T\left(\frac{\partial\widehat{V}}{\partial T}\right)_p\right]dp \tag{2.30}$$

In the fracture, the fracturing fluid flow in *x* direction and meanwhile leaks off into the reservoir in *y* direction during injection period. Therefore, the energy flux e_x and e_y are used for heat convection and can be simplified to the following expressions,

$$e_x=\left(\rho\widehat{U}\right)\boldsymbol{v_x}=\left(\rho\widehat{H}\right)\boldsymbol{v_x} \tag{2.31}$$

And,

$$e_y=\left(\rho\widehat{U}\right)\boldsymbol{v_y}=\left(\rho\widehat{H}\right)\boldsymbol{v_y} \tag{2.32}$$

Term $h\Delta x\left(e_y\right)_y$ is zero as there is no reservoir fluid flows into the fracture during injection and shut-in of the well.

On dividing Eq. (2.28) by differential volume $wh\Delta x$, and letting $\Delta x\rightarrow 0$, we have,

$$\frac{\partial}{\partial t}\left(\frac{1}{2}\rho v^2 + \rho\widehat{U}\right) = -\frac{\partial(e_x)}{\partial x} - \frac{2(e_y)|_{\,w}}{w} + \frac{2\dot{Q}|_{\,res-f}}{w} \tag{2.33}$$

Based on the assumptions, we know that the pressure inside fracture remains constant for an infinite conductivity fracture and equals to the bottomhole instantaneous shut-in pressure during injection. Also, the kinetic energy is negligible in this case. Thus, by substituting Eq. (2.29) and Eq. (2.30), for incompressible injection fluid, the LHS of Eq. (2.33) becomes to,

$$\frac{\partial}{\partial t}\left(\rho\widehat{U}\right) = \frac{\partial}{\partial t}\left(\rho\widehat{H}\right) = \rho\hat{C}_p\frac{\partial T}{\partial t} \tag{2.34}$$

The heat transfer rate given by Newton's Law at the fracture face, $\dot{Q}|_{\,res-f}$ can be described as,

$$\dot{Q}|_{\,res-f} = h_l(T_r - T_l) \tag{2.35}$$

Here, h_l is defined as Newton's heat transfer coefficient and it can be calculated by the following equation (Zhao and Tso, 1993),

$$h_l = Nv_x^s \tag{2.36}$$

In which, N and s are dimensionless empirical constants obtained from experiments.

Substitute Eq. (2.31), Eq. (2.32), Eq. (2.34), and Eq. (2.35) into Eq. (2.33), then manipulation gives,

$$\rho_l\hat{C}_{pl}\frac{\partial T_l}{\partial t} = -\frac{\rho_l\hat{C}_{pl}v_x\partial T_l}{\partial x} - \frac{2\rho_l\hat{C}_{pl}v_{lk}T_l}{w} + \frac{2h_l(T_r - T_l)}{w} \tag{2.37}$$

Where, " *l* " denotes the injection fluid properties in order to distinguish from reservoir and wellbore models. LHS of the above equation is the energy accumulation in

a differential volume over time *t*, the first term on the RHS is heat convection caused by fracturing fluid flow; second term is the convective energy loss due to fluid-loss, the last term is the heat transfer between the fracturing fluid and surrounding formation.

The initial and boundary conditions are:

$$I.C. \quad T_l = T_i, \qquad at\ t = 0 \tag{2.38}$$

$$B.C.s \quad \begin{cases} T_l = T, & at\ x = 0 \\ \dfrac{\partial T_l}{\partial x} = 0, & at\ x = X_f \end{cases} \tag{2.39}$$

Where, T_i represents the initial reservoir temperature. T is the injection fluid temperature, and v_I is the fluid velocity at $x = R$, and $\gamma = 1$, which are calculated from the wellbore model. The boundary coupled with the reservoir model at fracture face is shown in the reservoir thermal model.

2.4 Reservoir Model

The reservoir model established in this study can calculate fracturing fluid leak-off front and reservoir temperature distribution. Take an arbitrary differential volume from the reservoir, it is shown in **Fig. 2.5**.

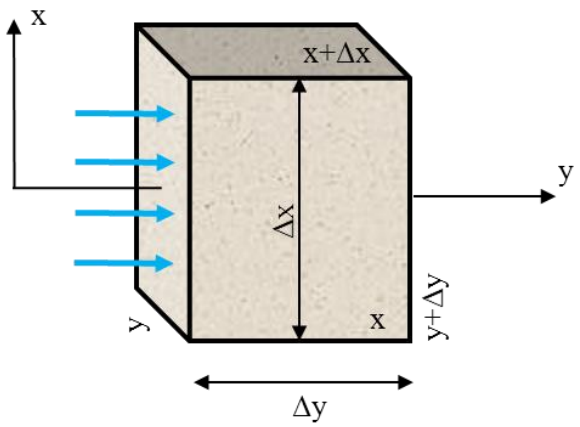

Fig. 2.5 A differential volume element in the reservoir

2.4.1 Fluid-loss into the Reservoir

The distance that fracturing fluid leaks off into the reservoir from fracture faces can be calculated by integrating the leak-off velocity with respect to leak-off time:

$$Y_{lk}(x) = \int_{\tau(x)}^{t} v_{lk} dt = \int_{\tau(x)}^{t} \frac{C}{\sqrt{t - \tau(x)}} dt \tag{2.40}$$

2.4.2 Reservoir Thermal Model

The reservoir thermal model is established to investigate reservoir temperature during fracturing treatment and to couple with the wellbore and fracture model. The transient reservoir thermal model is derived based on the general energy balance equation (Bird et al., 2002),

$$\frac{\partial(\rho \widehat{U})}{\partial t} = -\nabla \cdot \left(\rho \widehat{U} \boldsymbol{v}\right) - p\nabla \cdot \boldsymbol{v} - (\boldsymbol{\tau} : \nabla \boldsymbol{v}) - \nabla \cdot \boldsymbol{q} \tag{2.41}$$

Where, the LHS in Eq. (2.41) is the internal energy accumulation rate per unit volume. It is the summation of net rate change of internal energy caused by heat

convection, the reversible rate of internal energy increase by compression, the irreversible rate of internal energy change by viscous dissipation, and the rate of internal energy addition by conductive heat transfer per unit volume.

The internal energy in a porous media reservoir includes the internal energy of the formation rock and reservoir fluid it contains. Therefore, we can calculate the average bulk internal energy by,

$$\rho\widehat{U} = \phi\rho_f U_f + (1-\phi)\rho_r \widehat{U}_r \tag{2.42}$$

Where, $\widehat{U}$ represents the total internal energy per unit volume. The subscript " r " and " f " denote the formation rock matrix and reservoir fluid respectively.

The term $-(\boldsymbol{\tau}:\nabla\boldsymbol{v})$ involved in the consideration of energy equation denotes the viscous dissipation of energy by frictional forces. Al-Hadrami et al. (2003) derived an expression of the viscous dissipation term, which honors the asymptotic limiting conditions of low permeability porous media. When permeability is small enough, the effective fluid viscosity is close to zero, and for high permeability formation, assume the permeability is unlimited, the viscosity is close to the clear fluid viscosity. Considering the velocity vector is given by,

$$\boldsymbol{v} = U\boldsymbol{i} + V\boldsymbol{j} + W\boldsymbol{k} \tag{2.43}$$

Where, *U*, *V* and *W* are the components of the velocity vector, and $\boldsymbol{i}, \boldsymbol{j}, \boldsymbol{k}$ denote the unit vectors in the X-, Y-, Z- Cartesian coordinates, respectively.

The work done by frictional forces for three special cases are derived by Al-Hadrami et al. (2003) as following expressions,

(1) Motion of clear fluid is described by the Navier-Stokes equation,

$$Work\ Done = \rho \frac{D}{Dt}\left(\frac{U^2 + V^2 + W^2}{2}\right) - P\left(\frac{\partial U}{\partial x} + \frac{\partial V}{\partial y} + \frac{\partial W}{\partial z}\right)$$
$$+ \mu_f \left[2\left(\frac{\partial U}{\partial x}\right)^2 + 2\left(\frac{\partial V}{\partial x}\right)^2 + 2\left(\frac{\partial W}{\partial x}\right)^2 + \left(\frac{\partial U}{\partial y} + \frac{\partial V}{\partial x}\right)^2 \right. \quad (2.44)$$
$$\left. + \left(\frac{\partial U}{\partial z} + \frac{\partial W}{\partial x}\right)^2 + \left(\frac{\partial V}{\partial z} + \frac{\partial W}{\partial y}\right)^2\right]$$

The first term on the RHS of the above equation denotes the amount of work transformed into kinetic energy; the second term denotes the work involved in fluid compression; and the last term represents the amount of work lost by dissipation into heat, respectively (Beckett, 1980, Beckett and Friend, 1984).

The substantial derivative is defined by,

$$\frac{DP}{Dt} = \frac{\partial P}{\partial t} + \boldsymbol{v} \cdot \nabla P \quad (2.45)$$

(2) Motion of fluid in porous media is described by the Darcy equation,

$$Work\ Done = -P\left(\frac{\partial U}{\partial x} + \frac{\partial V}{\partial y} + \frac{\partial W}{\partial z}\right) + \frac{\mu_f}{K}(U^2 + V^2 + W^2) \quad (2.46)$$

Where, the first term on the RHS of Eq. (2.46) denotes the work involved in fluid compression and the second term denotes the amount of work lost by dissipation into heat, respectively (Ingham et al. 1990).

(3) Motion of fluid in porous media is described by the Brinkman equation (Al-Hadrami et al. (2003)),

$$Work\ Done = -P\left(\frac{\partial U}{\partial x}+\frac{\partial V}{\partial y}+\frac{\partial W}{\partial z}\right)+\frac{\mu_f}{K}(U^2+V^2+W^2)$$
$$+\mu\left[2\left(\frac{\partial U}{\partial x}\right)^2+2\left(\frac{\partial V}{\partial x}\right)^2+2\left(\frac{\partial W}{\partial x}\right)^2\right. \quad (2.47)$$
$$\left.+\left(\frac{\partial U}{\partial y}+\frac{\partial V}{\partial x}\right)^2+\left(\frac{\partial U}{\partial z}+\frac{\partial W}{\partial x}\right)^2+\left(\frac{\partial V}{\partial z}+\frac{\partial W}{\partial y}\right)^2\right]$$

Hence, Al-Hadrami et al. (2003) determined that the viscous dissipation for low permeability formation is expressed by the following, as in the case of the motion of fluid in porous media described by Darcy equation,

$$Viscous\ Dissipation \equiv (\boldsymbol{\tau}:\nabla\boldsymbol{v}) = \frac{\mu_f}{K}(U^2+V^2+W^2) \quad (2.48)$$

Which, Eq. (2.48) can be written as,

$$Viscous\ Dissipation \equiv (\boldsymbol{\tau}:\nabla\boldsymbol{v}) = \mu_f \boldsymbol{v}\cdot K^{-1}\cdot\boldsymbol{v} = -(\boldsymbol{v}\cdot\nabla p) \quad (2.49)$$

Therefore, the viscous dissipation heating term $-(\boldsymbol{\tau}:\nabla\boldsymbol{v})$ can be replaced by $-(\boldsymbol{v}\cdot\nabla p)$ for fluid flow in porous media (Al-Hadhrami et al., 2003).

Additionally, by applying Fourier's law, the heat conduction term can be written as,

$$\nabla\cdot\boldsymbol{q} = -\nabla\cdot(K_e\nabla T) \quad (2.50)$$

Where, K_e is the average effective reservoir thermal conductivity and can be calculated by,

$$K_e = \phi K_f + (1-\phi)K_r \quad (2.51)$$

Substitute Eq. (2.42), Eq. (2.49) and Eq. (2.50) into Eq. (2.41), the energy conservation equation can be rewritten as,

$$\frac{\partial}{\partial t}\left[\phi\rho_f U_f + (1-\phi)\rho_r \widehat{U}_r\right] = -\nabla\cdot\left(\rho\widehat{U}\boldsymbol{v}\right) - p\nabla\cdot\boldsymbol{v} - (\boldsymbol{v}\cdot\nabla p) + \nabla\cdot(K_e\nabla T) \tag{2.52}$$

By using thermodynamic equilibrium relationships (Bird et al., 2002), the total derivative of enthalpy can be derived as,

$$d\widehat{H} = \hat{C}_p dT + \frac{1}{\rho}(1-\beta T)dp \tag{2.53}$$

Where, β is the thermal expansion coefficient and it is defined as,

$$\beta = -\frac{1}{\rho}\left(\frac{\partial\rho}{\partial T}\right)_P = -\frac{1}{V}\left(\frac{\partial V}{\partial T}\right)_P \tag{2.54}$$

Substitute Eq. (2.29) to Eq. (2.52), we have,

$$\frac{\partial}{\partial t}\left[\phi\rho_f\widehat{H} - \phi p + (1-\phi)\rho_r\widehat{U}_r\right] = -\nabla\cdot\left(\rho\widehat{H}\boldsymbol{v}\right) + \nabla\cdot(K_e\nabla T) \tag{2.55}$$

The internal energy of rock can be approximated by heat capacity and temperature change due to the constant rock density,

$$d\widehat{U}_r \cong d\widehat{H}_r = \hat{C}_{pr}dT_r \tag{2.56}$$

Where, T_r represents the formation rock temperature.

Substitute Eq. (2.56) into Eq. (2.55) and rearrange yields,

$$\begin{aligned}\phi\rho_f\frac{\partial\widehat{H}}{\partial t} + \widehat{H}\frac{\partial(\rho_f\phi)}{\partial t} - \phi\frac{\partial p}{\partial t} + \rho_r\hat{C}_{pr}(1-\phi)\frac{\partial T_r}{\partial t} \\ + T_r\frac{\partial}{\partial t}\left[\rho_r\hat{C}_{pr}(1-\phi)\right] \\ = -\widehat{H}\nabla\cdot\rho\boldsymbol{v} - \rho\boldsymbol{v}\cdot\nabla\widehat{H} + \nabla\cdot(K_e\nabla T)\end{aligned} \tag{2.57}$$

Based on the mass conservation of reservoir fluid, we have,

$$\frac{\partial}{\partial t}(\rho_f \phi) = -\nabla \cdot \rho_f \boldsymbol{v} \tag{2.58}$$

From the mass conservation of formation rock, we have,

$$\frac{\partial}{\partial t}[\rho_r(1-\phi)] = 0 \tag{2.59}$$

By substituting Eq. (2.58) and Eq. (2.59), Eq. (2.57) becomes to,

$$\phi\rho_f \frac{\partial \widehat{H}}{\partial t} - \phi \frac{\partial p}{\partial t} + \rho_r \hat{C}_{pr}(1-\phi)\frac{\partial T_r}{\partial t} = -\rho \boldsymbol{v} \cdot \nabla \widehat{H} + \nabla \cdot (K_e \nabla T) \tag{2.60}$$

Substitute d$\widehat{H}$ from Eq. (2.53) into Eq. (2.60) and manipulate, we have,

$$\begin{aligned} &\phi\rho_f \hat{C}_{pf}\frac{\partial T}{\partial t} - \phi\beta T\frac{\partial p}{\partial t} + \rho_r \hat{C}_{pr}(1-\phi)\frac{\partial T_r}{\partial t} \\ &\qquad = -\rho \boldsymbol{v} \cdot \hat{C}_p \nabla T + (\beta T - 1)\boldsymbol{v} \cdot \nabla p + \nabla \cdot (K_e \nabla T) \end{aligned} \tag{2.61}$$

The average effective property of formation fluid and rock can be defined as,

$$\overline{\rho \hat{C}_p} = \phi\rho_f \hat{C}_{pf} + \rho_r \hat{C}_{pr}(1-\phi) \tag{2.62}$$

Assuming the thermal equilibrium between formation fluid and rock matrix can be reached instantaneously, we can use an overall temperature to represent formation temperature, which in other words, $T = T_r$, thus, we can rewrite Eq. (2.61) as,

$$\overline{\rho \hat{C}_p}\frac{\partial T_r}{\partial t} - \phi\beta T_r \frac{\partial p}{\partial t} = -\rho \boldsymbol{v} \cdot \hat{C}_p \nabla T_r + (\beta T_r - 1)\boldsymbol{v} \cdot \nabla p + \nabla \cdot (K_e \nabla T_r) \tag{2.63}$$

In Cartesian coordinate system, 2-D problem, assume there is no fracturing fluid flow in the *x* direction in the reservoir (only leak-off velocity in the *y* direction), the energy balance becomes to,

$$\overline{\rho\hat{C}_p}\frac{\partial T_r}{\partial t} - \phi\beta T_r\frac{\partial p}{\partial t}$$

$$= -\rho_l\hat{C}_{pl}v_{lk}\frac{\partial T_r}{\partial \mathrm{y}} + (\beta T_r - 1)v_{lk}\frac{\partial p}{\partial y} + \frac{\partial}{\partial x}\left(K_e\frac{\partial T_r}{\partial \mathrm{x}}\right) \qquad (2.64)$$

$$+ \frac{\partial}{\partial y}\left(K_e\frac{\partial T_r}{\partial \mathrm{y}}\right)$$

Similar to the wellbore thermal model, thermal expansion for water based injection fluid can be neglected, Eq. (2.64) becomes to,

$$\overline{\rho\hat{C}_p}\frac{\partial T_r}{\partial t} = -\rho_l\hat{C}_{pl}v_{lk}\frac{\partial T_r}{\partial \mathrm{y}} + \frac{\partial}{\partial x}\left(K_e\frac{\partial T_r}{\partial \mathrm{x}}\right) + \frac{\partial}{\partial y}\left(K_e\frac{\partial T_r}{\partial \mathrm{y}}\right) \qquad (2.65)$$

Equation (2.65) is the energy conservation equation in the formation at local position. The average effective heat capacity and effective thermal conductivity is not constant for the grid blocks invaded by the fracturing fluid. LHS of the above equation is energy accumulation in a differential volume over time *t*; the first term on the RHS is heat convection due to fluid leaks off into the formation; the second and third terms are the heat conduction in a 2-D flow system.

The initial and boundary conditions for Eq. (2.65) are,

$$I.C. \quad T_r = T_i, \qquad at\ t = 0 \qquad (2.66)$$

$$B.C.s \begin{cases} \dfrac{\partial T_r}{\partial x} = 0, & at\ x \to \infty \\ \dfrac{\partial T_r}{\partial y} = 0, & at\ y \to \infty \\ K_e\dfrac{\partial T_r}{\partial y} = h_l(T_r - T_l), & at\ y = \dfrac{w}{2} \\ K_e\dfrac{\partial T_r}{\partial x} = U_T(T_r - T), & at\ x = x_{res/wb} \end{cases} \qquad (2.67)$$

The boundary condition at the fracture face and reservoir/wellbore interface are used to couple with the fracture and wellbore model. The solution by finite difference approach is presented in Chapter 3.

3. INTEGRATED FORWARD MODEL SOLUTION

3.1 Introduction

In the previous chapter, the forward model has been developed, as well as the initial and boundary conditions. In this chapter, the solution procedure and approach for each model is discussed in detail, and the integrated solution for multiple stages fracture treatments is presented. Numerical solutions are necessary for time dependent fluid-loss and complex non-linear heat exchange. Particularly, in order to efficiently solve the coupled integrated thermal model, the discretization of the wellbore, reservoir and fracture model is considered conjointly. The Mass and energy conservation equations are solved by finite difference approach for the gridding system. The thermal models are solved implicitly with upstream weighted.

Due to the symmetrical configuration of the physical problem. The calculation domain is only one quarter of the full modeled domain to reduce the calculation time as shown in **Fig. 3.1**.

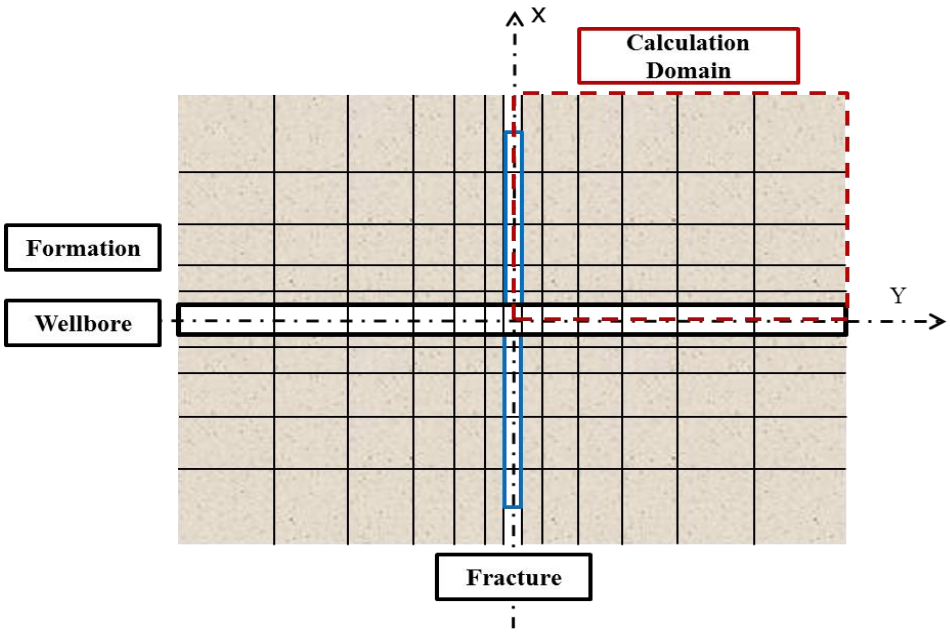

Fig. 3.1 Calculation domain of the integrated forward model

All the mass and energy conservation equations are solved specifically for this calculation domain. The discretization of the calculation domain is shown in **Fig. 3.2**.

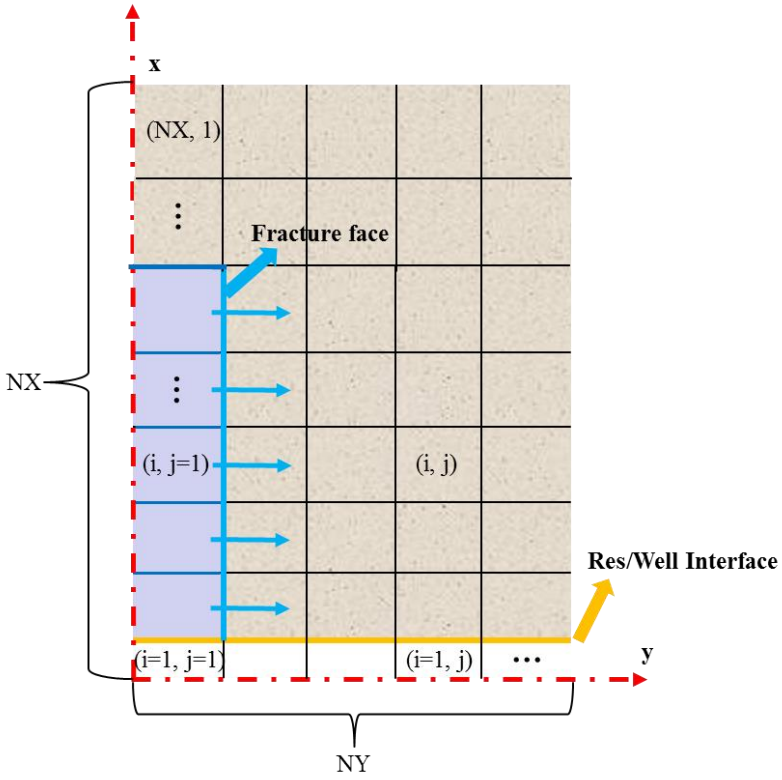

Fig. 3.2 Discretization of the calculation domain

As shown in **Fig. 3.2**, the wellbore takes the first grid block in *x* direction and the fracture is assigned to be the first grid block in *y* direction. Accordingly, the boundary conditions for coupling between each model is discussed in detail later in this chapter.

3.2 Wellbore Model Solution

The wellbore model is solved to provide injection flow rate and temperature along the wellbore as input for the fracture and reservoir model. It is solved numerically by using finite difference approach. The gridding scheme is shown in **Fig. 3.3**.

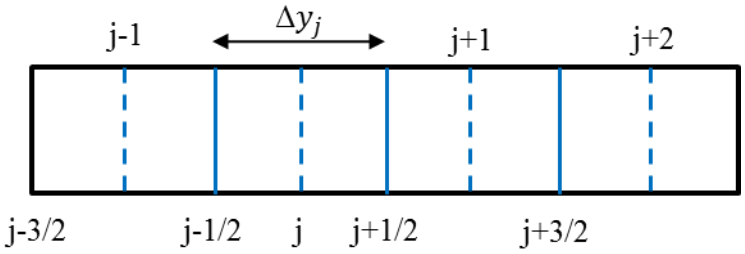

Fig. 3.3 Gridding configuration in the wellbore

3.2.1 Wellbore Flow Model Solution

The wellbore mass conservation equation is derived in Chapter 2. The discretized form of Eq. (2.2) is,

$$0 = \frac{v_{i,j+\frac{1}{2}} - v_{i,j-\frac{1}{2}}}{\Delta y_j} - \frac{2\gamma v_{I_{i,j}}}{R} \tag{3.1}$$

Hence, the velocity at grid interface can be calculated,

$$v_{i,j+\frac{1}{2}} = \frac{2\gamma v_{I_{i,j}}}{R}\Delta y_j + v_{i,j-\frac{1}{2}} \tag{3.2}$$

The wellbore model is assigned to be i = 1, thus, the above equation can be rewritten as,

$$v_{1,j+\frac{1}{2}} = \frac{2\gamma v_{I_{1,j}}}{R}\Delta y_j + v_{1,j-\frac{1}{2}} \tag{3.3}$$

3.2.2 Wellbore Thermal Model Solution

As mentioned before, wellbore is assigned to be the first grid block in x direction. In other words, for $(i = 1, j = 1, 2, \ldots N_y)$, wellbore energy conservation equation is applied to obtain temperature distribution.

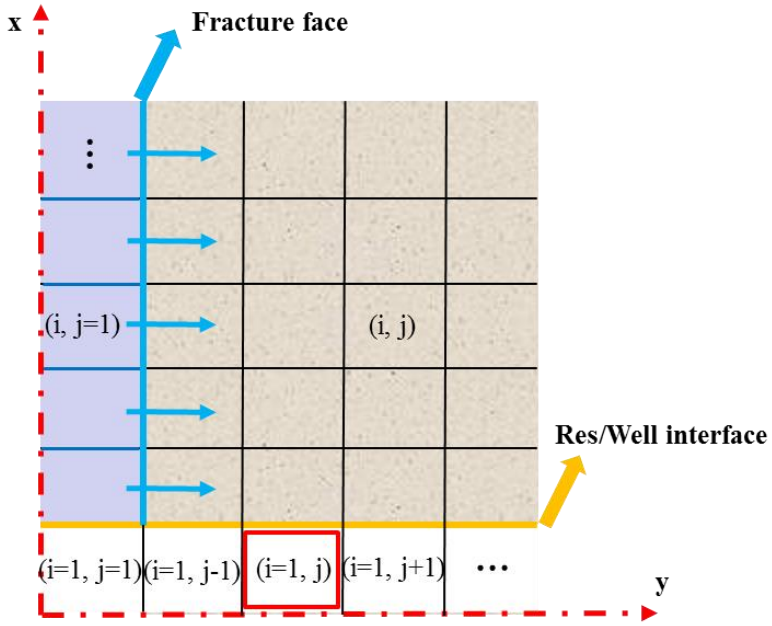

Fig. 3.4 Gridding scheme of the wellbore in the calculation domain

For a mesh cell shown in the above figure, the finite difference equation for energy balance is,

$$\rho\hat{C}_p\frac{T_{1,j}^n - T_{1,j}^{n-1}}{\Delta t} = \frac{2\gamma}{R}\rho_I(v_I)_{1,j}\hat{C}_p(T_I - T)_{1,j}^n + \frac{2(1-\gamma)}{R}U_T\left(T_{2,j}^n - T_{1,j}^n\right) + \rho v_{1,j}^n\hat{C}_p\frac{T_{1,j+\frac{1}{2}}^n - T_{1,j-\frac{1}{2}}^n}{\Delta y_j} + \rho v_{1,j}^n g\sin\theta \quad (3.4)$$

The temperature at the grid boundary can be replaced by the corresponding upstream grid temperature due to the heat convection transferred by fluid flow. And rearrange the above equation, we obtain,

$$\frac{\rho v_{1,j}^{n}\hat{C}_p}{\Delta y_j}T_{1,j-1}^{n}+\left[\frac{\rho\hat{C}_p}{\Delta t}+\frac{2\gamma}{R}\rho_I(v_I)_{1,j}\hat{C}_p+\frac{2(1-\gamma)}{R}U_T-\frac{\rho v_{1,j}^{n}\hat{C}_p}{\Delta y_j}\right]T_{1,j}^{n}$$

$$-\frac{2(1-\gamma)}{R}U_T T_{2,j}^{n}-\frac{2\gamma}{R}\rho_I(v_I)_{1,j}\hat{C}_p T_{I_{1,j}}^{n} \tag{3.5}$$

$$=\frac{\rho\hat{C}_p}{\Delta t}T_{1,j}^{n-1}+\rho v_{1,j}^{n}g\sin\theta$$

And the temperature for grid block (i = 1, j) shown in **Fig. 3.4** is calculated by,

$$T_{1,j}^{n}=\left[\frac{\rho\hat{C}_p}{\Delta t}+\frac{2\gamma}{R}\rho_I(v_I)_{1,j}\hat{C}_p+\frac{2(1-\gamma)}{R}U_T-\frac{\rho v_{1,j}^{n}\hat{C}_p}{\Delta y_j}\right]^{-1}$$

$$\cdot\left[\frac{\rho\hat{C}_p}{\Delta t}T_{1,j}^{n-1}+\rho v_{1,j}^{n}g\sin\theta-\frac{\rho v_{1,j}^{n}\hat{C}_p}{\Delta y_j}T_{1,j-1}^{n}\right. \tag{3.6}$$

$$\left.+\frac{2(1-\gamma)}{R}U_T T_{2,j}^{n}+\frac{2\gamma}{R}\rho_I(v_I)_{1,j}\hat{C}_p T_{I_{1,j}}^{n}\right]$$

In which, the local grid is coupled with fracture grids at $\gamma = 1$, while other mesh grids are coupled with reservoir model at $\gamma = 0$. During injection, the wellbore temperature is assumed to be uniform and equals to fracturing fluid injection temperature. And during shut-in, Eq. (3.6) is used to obtain wellbore temperature solved simultaneously coupling with the fracture and reservoir thermal model.

When considering plug and perf completion method, there is casing and cement existed between the wellbore and formation, extra mesh cells can be added outside of the wellbore. The number of grids in the fracture and reservoir model will be changed accordingly. For example, the new gridding scheme considering casing and cement shows in the following figure,

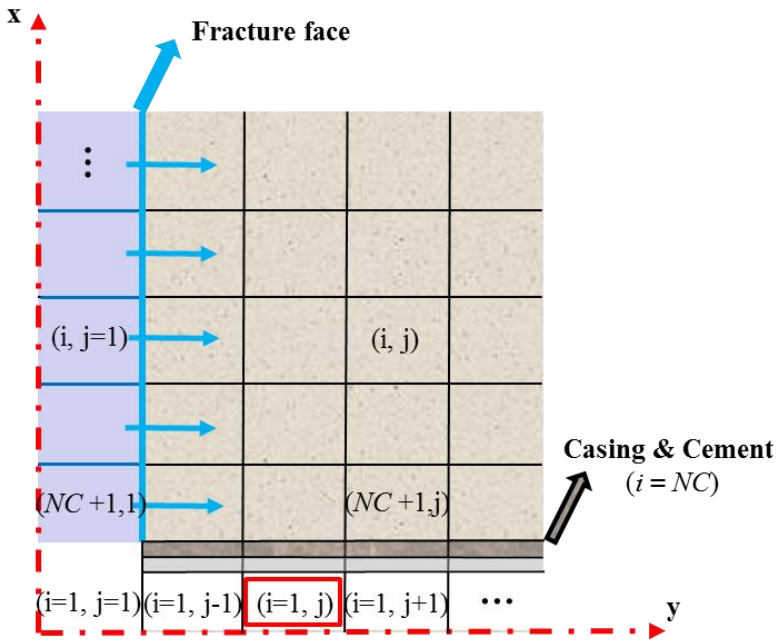

Fig. 3.5 Gridding scheme of the wellbore for plug and perf completion

The reservoir temperature calculation then can be extended to the casing and cement with different grid properties, such as zero porosity, higher thermal conductivity compare to the formation rock. The solutions is presented in the following chapters. Consequently, the temperature at different location can be simulated and to interpret measured DTS data in the case of different DTS deployment location due to different completion methods.

3.3 Fracture Model Solution

The finite difference equation and numerical solution of fracture flow model is derived based on the following mesh gridding system.

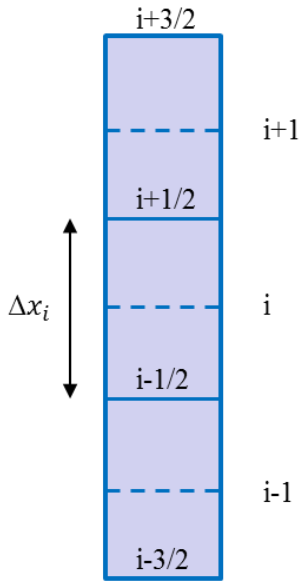

Fig. 3.6 Gridding configuration in the fracture

3.3.1 Solution of the Fracture Flow Model

Analytical solution of the fracture flow model is not applicable due to the time dependent fluid-loss. Thus, the fracture is solved numerically using finite difference approach. Assuming time step *n* is consistency with fracture propagating step *i*, in other words, at time step *n*, the fracture propagates to the *i*-th grid block.

The discretized form of continuity equation (Eq. (2.20)) for a calculation domain is written as,

$$wh\frac{X_{f_i}^{\,n} - X_{f_i}^{\,n-1}}{\Delta t} = (q_{inj_i}^{\,n} - q_{inj_{i-1}}^{\,n}) - 2h\sum_{i=1}^{n} C\Delta x_i \int_{t_{n-1}}^{t_n} \frac{1}{\sqrt{t-\tau(x_i)}}\,dt \tag{3.7}$$

Based on the definition of $\tau(x)$, at time step n, fluid leak-off starts from $x_{i-1/2}$. Therefore, $\tau(x_i)$ can be replaced by,

$$\tau(x_i) = t_{i-\frac{1}{2}} = \frac{t_{i-1} + t_i}{2} \tag{3.8}$$

For given time step *Δt*, we can calculate the fracture half-length at the *i*-th grid block using Eq. (3.7).

$$\begin{aligned} wh\Delta x_n &= wh\left(\Delta x_{n+\frac{1}{2}} - \Delta x_{n-\frac{1}{2}}\right) = wh\left[X_f(t_n) - X_f(t_{n-1})\right] \\ &= q_{inj}\Delta t_n - 2h\sum_{i=1}^{n-1} C\Delta x_i \int_{t_{n-1}}^{t_n} \frac{1}{\sqrt{t - t_{i-\frac{1}{2}}}} dt \\ &\quad - 2hC\Delta x_n \int_{t_{n-1}}^{t_n} \frac{1}{\sqrt{t - t_{n-1}}} dt \end{aligned} \tag{3.9}$$

Integrating the leak-off term, we obtain,

$$\begin{aligned} wh\Delta x_n = q_{inj}\Delta t_n &- 2h\sum_{i=1}^{n-1} C\Delta x_i [2\sqrt{t - t_{i-\frac{1}{2}}}]\Big|_{t_{n-1}}^{t_n} \\ &- 2hC\Delta x_n [2\sqrt{t - t_{i-1}}]\Big|_{t_{n-1}}^{t_n} \end{aligned} \tag{3.10}$$

Rewrite Eq. (3.10) in expansion of t_{n-1} to t_n gives,

$$\begin{aligned} wh\Delta x_n = q_{inj}\Delta t_n &- 2h\sum_{i=1}^{n-1} C\Delta x_i [2\sqrt{t_n - t_{i-\frac{1}{2}}} - 2\sqrt{t_{n-1} - t_{i-\frac{1}{2}}}] \\ &- 2hC\Delta x_n [2\sqrt{\Delta t_n}] \end{aligned} \tag{3.11}$$

Where Δx_i and Δt_n can be calculated based on the gridding system,

$$\Delta x_i = x_{i-\frac{1}{2}} - x_{i+\frac{1}{2}} \tag{3.12}$$

And,

$$\Delta t_n = t_n - t_{n-1} \tag{3.13}$$

Manipulate Eq. (3.11) and rearrange for Δx_n, we have,

$$\Delta x_n = \frac{\left[q_{inj}\Delta t_n - 4Ch\sum_i^{n-1}\Delta x_i\left(\sqrt{t_n - t_{i-\frac{1}{2}}} - \sqrt{t_{n-1} - t_{i-\frac{1}{2}}}\right)\right]}{wh - 4Ch\sqrt{\Delta t_n}} \tag{3.14}$$

From Eq. (3.14) we can calculate the fracture half-length increase for a given time step. In this case, the fracture half-length increasing rate is decrease due to the accumulation of the fluid-loss and constant injection rate and time step.

3.3.2 Solution of the Fracture Thermal Model

The fracture thermal model is solved numerically by coupling with the reservoir and wellbore thermal model. For one calculation domain, the fracture is assigned as the first grid block in *y* direction (well flow direction), which is *j* = 1 in the discretization scheme shows in **Fig. 3.7**.

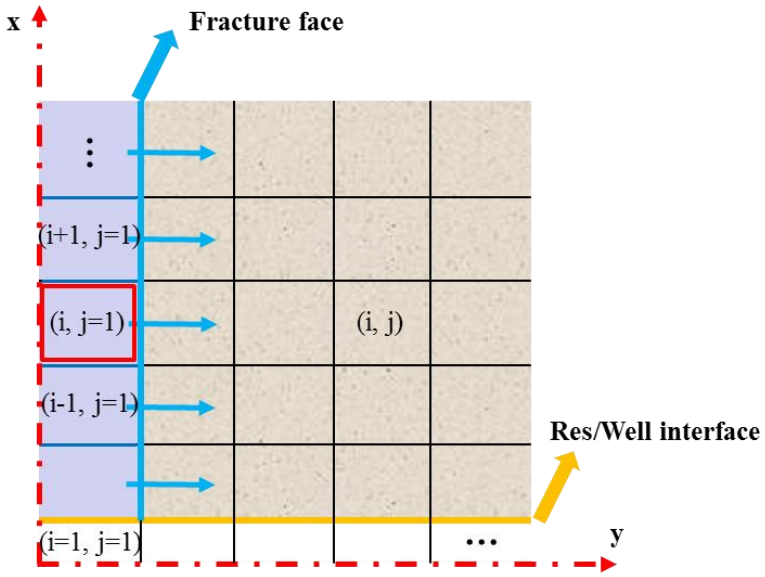

Fig. 3.7 Gridding scheme of the fracture in the calculation domain

The discretization of the energy conservation equation in the fracture can be written for one calculation domain based on Eq. (2.37),

$$\frac{\left(v_{x}{}^{n}_{i-\frac{1}{2},j}T_{l}{}^{n}_{i-1,j}-v_{x}{}^{n}_{i+\frac{1}{2},j}T_{l}{}^{n}_{i,j}\right)}{\Delta x_i}-\frac{2v_{lk}{}^{n}_{i,j}T_{l}{}^{n}_{i,j}}{w}+\frac{2h_l\left(T_{l}{}^{n}_{i,j+1}-T_{l}{}^{n}_{i,j}\right)}{\rho_l\hat{C}_{pl}w}=\frac{\left(T_{l}{}^{n}_{i,j}-T_{l}{}^{n-1}_{i,j}\right)}{\Delta t} \tag{3.15}$$

Where, velocity v_x and v_{lk} are calculated by fracture flow model, and the upstream mesh cell temperature is used at the interface for heat convection. As the fracture is the first grid in *y* direction, we can rewrite Eq. (3.15) as,

$$\frac{\left({v_x}^n_{i-\frac{1}{2},1}{T_l}^n_{i-1,1} - {v_x}^n_{i+\frac{1}{2},1}{T_l}^n_{i,1}\right)}{\Delta x_i} - \frac{2{v_{lk}}^n_{i,1}{T_l}^n_{i,1}}{w} + \frac{2h_l\left(T^n_{l_{i,2}} - T^n_{l_{i,1}}\right)}{\rho_l \hat{C}_{pl} w} = \frac{\left(T^n_{l_{i,1}} - T^{n-1}_{l_{i,1}}\right)}{\Delta t} \tag{3.16}$$

Where, $T^n_{l_{i,2}}$ represents the temperature of contacted grid block in the reservoir mesh and has to be solved simultaneously with the fracture thermal model as a boundary condition.

Rearrange Eq. (3.16) for matrix computation, we obtain,

$$\frac{T^{n-1}_{l_{i,1}}}{\Delta t} = \left(\frac{{v_x}^n_{i+\frac{1}{2},1}}{\Delta x_i} + \frac{2{v_{lk}}^n_{i,1}}{w} + \frac{2h_l}{\rho_l \hat{C}_{pl} w} + \frac{1}{\Delta t}\right){T_l}^n_{i,1} - \frac{{v_x}^n_{i-\frac{1}{2},1}}{\Delta x_i}{T_l}^n_{i-1,1} - \frac{2h_l}{w}T^n_{l_{i,2}} \tag{3.17}$$

The boundary conditions at the wellbore and fracture interface is shared by grid block *i* = 1 which is from wellbore model and *i* = 2 from fracture model. During injection period ($t \leq t_{inj}$), we have,

$$\begin{cases} {T_l}^n_{1,1} = {T_{inj}}^n, & at\ x = x_{\frac{3}{2}} \\ {v_x}^n_{\frac{3}{2},1} = v_I^n, & at\ x = x_{\frac{3}{2}} \end{cases} \tag{3.18}$$

Therefore, during injection, at (*i* = 2, *j* = 1), the energy balance is,

$$\frac{T_{l_{2,1}}^{n-1}}{\Delta t} + \frac{v_I^n}{\Delta x_2} T_{inj}{}^n = \left(\frac{v_{x\frac{5}{2},1}^{n}}{\Delta x_2} + \frac{2v_{lk}{}_{2,1}^{n}}{w} + \frac{2h_l}{\rho_l \hat{C}_{pl} w} + \frac{1}{\Delta t} \right) T_{l_{2,1}}^{n} - \frac{2h_l}{w} T_{l_{2,2}}^{n} \tag{3.19}$$

During shut-in period, a "no flow" condition results in zero velocity of Eq. (3.19), the temperature inside fracture is solved by incorporating the appropriate boundary condition with the reservoir model,

$$\frac{\rho_l \hat{C}_{pl} \left(T_{l_{i,1}}^{n} - T_{l_{i,1}}^{n-1} \right)}{\Delta t} = K_e \frac{\left(T_{l_{i,2}}^{n} - T_{l_{i,1}}^{n} \right)}{\Delta y_2} \tag{3.20}$$

3.4 Reservoir Model Solution

The distance of leak-off fluid travels into the reservoir can be solved analytically and numerically. However, the non-linear heat transfer in the reservoir has to be solved numerically. As we discussed in the fracture thermal model, the reservoir model is coupled with the fracture and wellbore model and has to be solved simultaneously at each time step. The mesh cells scheme shows in **Fig. 3.8**.

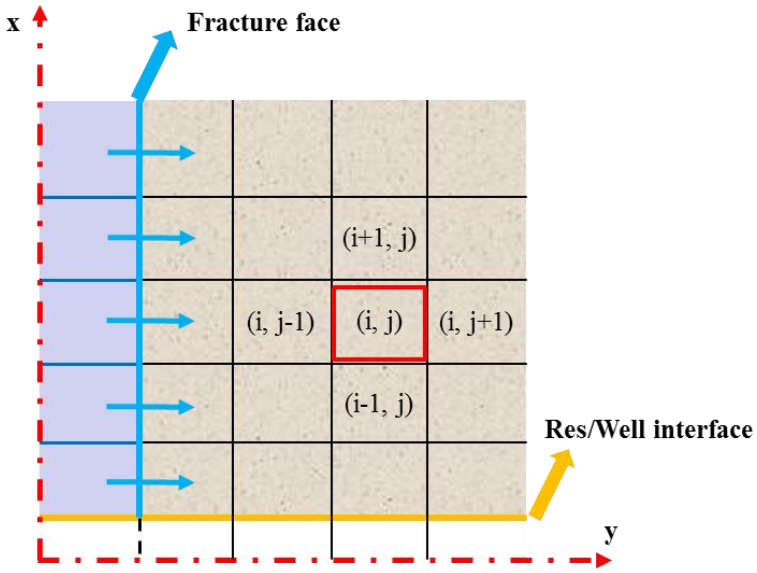

Fig. 3.8 Gridding scheme of the reservoir in the calculation domain

3.4.1 Fluid Leak-off Front

Similar to the fracture flow model, the front of fluid-loss travels into the reservoir can also be calculated by Eq. (2.40), after integration, Eq. (2.40) becomes to,

$$Y_{lk}(x) = \int_{\tau(x)}^{t} v_{lk}\,dt = \int_{\tau(x)}^{t} \frac{C}{\sqrt{t-\tau(x)}}\,dt = 2C\sqrt{t-\tau(x)} \tag{3.21}$$

In the reservoir, an effective travel distance needs to be considered regarding porosity of the rock matrix.

$$Y_{lk}(x) = 2C\sqrt{t-\tau(x)} = \frac{2C}{\phi}\sqrt{t-\tau(x)} \tag{3.22}$$

The finite difference equation is given as,

$$Y_{lk} = 4Ch\Delta x_i \left[\left(\sqrt{t-t_{i-1}}\right)_{t_{i-1}}^{t_i} + \sum_{i+1}^{n} \left(\sqrt{t-t_{i-\frac{1}{2}}} \right)_{t_i}^{t_{i+1}} \right] \tag{3.23}$$

3.4.2 Numerical Solution of the Reservoir Thermal Model

As it is shown in the gridding scheme, for grid block (i, j) in the reservoir, the discretization of the energy conservation equation (Eq. (2.65)) can be expressed as,

$$\begin{aligned}
&\frac{\left[\left(\overline{\rho\hat{C}_p}\right)_{i,j}^{n} T_{r}{}_{i,j}^{n} - \left(\overline{\rho\hat{C}_p}\right)_{i,j}^{n-1} T_{r}{}_{i,j}^{n-1}\right]}{\Delta t_n} \\
&= -\frac{\left(\rho_{l}{}_{i,j-1}^{n} \hat{C}_{pl}{}_{i,j-1}^{n} v_{lk}{}_{i,j-1}^{n} T_{r}{}_{i,j-1}^{n} - \rho_{l}{}_{i,j}^{n} \hat{C}_{pl}{}_{i,j}^{n} v_{lk}{}_{i,j}^{n} T_{r}{}_{i,j}^{n}\right)}{\Delta y_j} \\
&+ \frac{\left[K_{e}{}_{i-\frac{1}{2},j}^{n} \left(-\frac{\partial T_r}{\partial \mathrm{x}}\right)_{i-\frac{1}{2},j}^{n} - K_{e}{}_{i+\frac{1}{2},j}^{n} \left(-\frac{\partial T_r}{\partial \mathrm{x}}\right)_{i+\frac{1}{2},j}^{n}\right]}{\Delta x_i} \\
&+ \frac{\left[K_{e}{}_{i,j-\frac{1}{2}}^{n} \left(-\frac{\partial T_r}{\partial \mathrm{y}}\right)_{i,j-\frac{1}{2}}^{n} - K_{e}{}_{i,j+\frac{1}{2}}^{n} \left(-\frac{\partial T_r}{\partial \mathrm{y}}\right)_{i,j+\frac{1}{2}}^{n}\right]}{\Delta y_j}
\end{aligned} \tag{3.24}$$

The heat conduction term in both directions can be further expanded, thus, Eq. (3.24) becomes to,

$$\frac{\left[\left(\overline{\rho\hat{C}_p}\right)_{i,j}^{n} T_{r_{i,j}}^{\ n} - \left(\overline{\rho\hat{C}_p}\right)_{i,j}^{n-1} T_{r_{i,j}}^{\ n-1}\right]}{\Delta t_n}$$

$$= -\frac{\left(\rho_{l_{i,j-1}}^{n} \hat{C}_{pl}{}_{i,j-1}^{\ n} v_{lk}{}_{i,j-1}^{n} T_{r_{i,j-1}}^{\ n} - \rho_{l_{i,j}}^{n} \hat{C}_{pl}{}_{i,j}^{\ n} v_{lk}{}_{i,j}^{n} T_{r_{i,j}}^{\ n}\right)}{\Delta y_j}$$

$$+ \frac{\left[K_{e}{}_{i-\frac{1}{2},j}^{\ n} \frac{-\left(T_{r_{i,j}}^{\ n} - T_{r_{i-1,j}}^{\ n-1}\right)}{\frac{\Delta x_i + \Delta x_{i-1}}{2}} - K_{e}{}_{i+\frac{1}{2},j}^{\ n} \frac{-\left(T_{r_{i+1,j}}^{\ n} - T_{r_{i,j}}^{\ n-1}\right)}{\frac{\Delta x_{i+1} + \Delta x_i}{2}}\right]}{\Delta x_i} \tag{3.25}$$

$$+ \frac{\left[K_{e}{}_{i,j-\frac{1}{2}}^{\ n} \frac{-\left(T_{r_{i,j}}^{\ n} - T_{r_{i,j-1}}^{\ n-1}\right)}{\frac{\Delta y_j + \Delta y_{j-1}}{2}} - K_{e}{}_{i,j+\frac{1}{2}}^{\ n} \frac{-\left(T_{r_{i,j+1}}^{\ n} - T_{r_{i,j}}^{\ n-1}\right)}{\frac{\Delta y_{j+1} + \Delta y_j}{2}}\right]}{\Delta y_j}$$

The temperature is upstream weighted while the fracture and fluid-loss front are propagating. Moreover, the boundary conditions must be incorporated at the fracture face and reservoir/wellbore interface, as well as far boundaries in the reservoir.

As discussed in the previous chapter, the effective heat conductivity and capacity of the near fracture formation is changing with time due to the fluid-loss. Normally the thermal properties is very different between reservoir fluid and fracturing fluid. Rearrange Eq. (3.25) to solve for temperature distribution, we obtain,

$$-\frac{\left(\overline{\rho\hat{C}_p}\right)_{i,j}^{n-1}}{\Delta t_n}T_{r_{i,j}}^{n-1}$$

$$= \frac{2K_{e}{}_{i-\frac{1}{2},j}^{n}}{\Delta x_i(\Delta x_i + \Delta x_{i-1})}T_{r_{i-1,j}}^{n}$$

$$+\left[\frac{2K_{e}{}_{i,j-\frac{1}{2}}^{n}}{\Delta y_j(\Delta y_j + \Delta y_{j-1})} + \frac{\rho_{l}{}_{i,j-1}^{n}\hat{C}_{pl}{}_{i,j-1}^{n}v_{lk}{}_{i,j-1}^{n}}{\Delta y_j}\right]T_{r_{i,j-1}}^{n}$$

$$-\left[\frac{2K_{e}{}_{i-\frac{1}{2},j}^{n}}{\Delta x_i(\Delta x_i + \Delta x_{i-1})} + \frac{2K_{e}{}_{i+\frac{1}{2},j}^{n}}{\Delta x_i(\Delta x_{i+1} + \Delta x_i)} + \frac{2K_{e}{}_{i,j-\frac{1}{2}}^{n}}{\Delta y_j(\Delta y_j + \Delta y_{j-1}}\right.$$

$$\left. + \frac{2K_{e}{}_{i,j+\frac{1}{2}}^{n}}{\Delta y_j(\Delta y_{j+1} + \Delta y_j)} + \frac{\rho_{l}{}_{i,j}^{n}\hat{C}_{pl}{}_{i,j}^{n}v_{lk}{}_{i,j}^{n}}{\Delta y_j} + \frac{\left(\overline{\rho\hat{C}_p}\right)_{i,j}^{n}}{\Delta t_n}\right]T_{r_{i,j}}^{n} \quad (3.26)$$

$$+ \frac{2K_{e}{}_{i+\frac{1}{2},j}^{n}}{\Delta x_i(\Delta x_{i+1} + \Delta x_i)}T_{r_{i+1,j}}^{n} + \frac{2K_{e}{}_{i,j+\frac{1}{2}}^{n}}{\Delta y_j(\Delta y_{j+1} + \Delta y_j)}T_{r_{i,j+1}}^{n}$$

General expression for the above discretized equation in terms of spatial coefficients can be written as,

$$APT_{r_{i,j}}^{n-1} = AWT_{r_{i-1,j}}^{n} + AST_{r_{i,j-1}}^{n} + ACT_{r_{i,j}}^{n} + AET_{r_{i+1,j}}^{n} + ANT_{r_{i,j+1}}^{n} \quad (3.27)$$

Where, the spatial coefficients are given by,

$$AP = -\frac{\left(\overline{\rho\hat{C}_p}\right)_{i,j}^{n-1}}{\Delta t_n} \quad (3.28)$$

$$AW = \frac{2K_{e}{}_{i-\frac{1}{2},j}^{n}}{\Delta x_i(\Delta x_i + \Delta x_{i-1})} \quad (3.29)$$

$$AS = \frac{2K_{e}{}^{n}_{i,j-\frac{1}{2}}}{\Delta y_j\left(\Delta y_j + \Delta y_{j-1}\right)} + \frac{\rho_{l}{}^{n}_{i,j-1}\hat{C}_{pl}{}^{n}_{i,j-1}v_{lk}{}^{n}_{i,j-1}}{\Delta y_j} \tag{3.30}$$

$$AC = -\frac{2K_{e}{}^{n}_{i-\frac{1}{2},j}}{\Delta x_i(\Delta x_i + \Delta x_{i-1})} - \frac{2K_{e}{}^{n}_{i+\frac{1}{2},j}}{\Delta x_i(\Delta x_{i+1} + \Delta x_i)} - \frac{2K_{e}{}^{n}_{i,j-\frac{1}{2}}}{\Delta y_j\left(\Delta y_j + \Delta y_{j-1}\right)} - \frac{2K_{e}{}^{n}_{i,j+\frac{1}{2}}}{\Delta y_j\left(\Delta y_{j+1} + \Delta y_j\right)} - \frac{\rho_{l}{}^{n}_{i,j}\hat{C}_{pl}{}^{n}_{i,j}v_{lk}{}^{n}_{i,j}}{\Delta y_j} - \frac{\left(\overline{\rho\hat{C}_p}\right)^{n}_{i,j}}{\Delta t_n} \tag{3.31}$$

$$AE = \frac{2K_{e}{}^{n}_{i+\frac{1}{2},j}}{\Delta x_i(\Delta x_{i+1} + \Delta x_i)} \tag{3.32}$$

$$AN = \frac{2K_{e}{}^{n}_{i,j+\frac{1}{2}}}{\Delta y_j\left(\Delta y_{j+1} + \Delta y_j\right)} \tag{3.33}$$

To solve Eq. (3.26), various boundaries including far boundaries in the reservoir and the boundaries encountered with the fracture and wellbore interface must be taken into consideration. At the far boundary, where ($i = N_x$), no heat transfer boundary condition is applied,

$$AP = -\frac{\left(\overline{\rho\hat{C}_p}\right)^{n-1}_{N_x,j}}{\Delta t_n} \tag{3.34}$$

$$AW = \frac{2K_{e}{}^{n}_{N_x-\frac{1}{2},j}}{\Delta x_{N_x}\left(\Delta x_{N_x} + \Delta x_{N_x-1}\right)} \tag{3.35}$$

$$AS = \frac{2K_{e}{}^{n}_{N_x,j-\frac{1}{2}}}{\Delta y_j\left(\Delta y_j + \Delta y_{j-1}\right)} + \frac{\rho_{l}{}^{n}_{N_x,j-1}\hat{C}_{pl}{}^{n}_{N_x,j-1}v_{lk}{}^{n}_{N_x,j-1}}{\Delta y_j} \tag{3.36}$$

$$AC = -\frac{2K_e{}^{n}_{N_x-\frac{1}{2},j}}{\Delta x_{N_x}\left(\Delta x_{N_x}+\Delta x_{N_x-1}\right)} - \frac{2K_e{}^{n}_{N_x,j-\frac{1}{2}}}{\Delta y_j\left(\Delta y_j+\Delta y_{j-1}\right)} - \frac{2K_e{}^{n}_{N_x,j+\frac{1}{2}}}{\Delta y_j\left(\Delta y_{j+1}+\Delta y_j\right)} - \frac{\rho_l{}^{n}_{N_x,j}\hat{C}_{pl}{}^{n}_{N_x,j}v_{lk}{}^{n}_{N_x,j}}{\Delta y_j} - \frac{\left(\overline{\rho\hat{C}_p}\right)^{n}_{N_x,j}}{\Delta t_n} \tag{3.37}$$

$$AE = 0 \tag{3.38}$$

$$AN = \frac{2K_e{}^{n}_{N_x,j+\frac{1}{2}}}{\Delta y_j\left(\Delta y_{j+1}+\Delta y_j\right)} \tag{3.39}$$

Similarly, at ($j = N_y$), we have,

$$AP = -\frac{\left(\overline{\rho\hat{C}_p}\right)^{n-1}_{i,N_y}}{\Delta t_n} \tag{3.40}$$

$$AW = \frac{2K_e{}^{n}_{i-\frac{1}{2},N_y}}{\Delta x_i(\Delta x_i+\Delta x_{i-1})} \tag{3.41}$$

$$AS = \frac{2K_e{}^{n}_{i,N_y-\frac{1}{2}}}{\Delta y_{N_y}\left(\Delta y_{N_y}+\Delta y_{N_y-1}\right)} + \frac{\rho_l{}^{n}_{i,N_y-1}\hat{C}_{pl}{}^{n}_{i,N_y-1}v_{lk}{}^{n}_{i,N_y-1}}{\Delta y_{N_y}} \tag{3.42}$$

$$AC = -\frac{2K_{e}{}^{n}_{i-\frac{1}{2},N_y}}{\Delta x_i(\Delta x_i + \Delta x_{i-1})} - \frac{2K_{e}{}^{n}_{i+\frac{1}{2},N_y}}{\Delta x_i(\Delta x_{i+1} + \Delta x_i)} - \frac{2K_{e}{}^{n}_{i,N_y-\frac{1}{2}}}{\Delta y_j(\Delta y_j + \Delta y_{j-1})} - \frac{\rho_{l}{}^{n}_{i,N_y}\hat{C}_{pl}{}^{n}_{i,N_y} v_{lk}{}^{n}_{i,N_y}}{\Delta y_j} - \frac{\left(\overline{\rho\hat{C}_p}\right)^{n}_{i,N_y}}{\Delta t_n} \tag{3.43}$$

$$AE = \frac{2K_{e}{}^{n}_{i+\frac{1}{2},N_y}}{\Delta x_i(\Delta x_{i+1} + \Delta x_i)} \tag{3.44}$$

$$AN = 0 \tag{3.45}$$

During injection period, when $t \le t_{inj}$, it is constant injection fluid temperature inside wellbore. Thus, at i = 2, we have,

$$\begin{aligned} -\frac{\left(\overline{\rho\hat{C}_p}\right)^{n-1}_{2,j}}{\Delta t_n} T_{r}{}^{n-1}_{2,j} = {} & \frac{2K_{e}{}^{n}_{\frac{3}{2},j}}{\Delta x_2(\Delta x_2 + \Delta x_1)} T_{inj} \\ & + \left[\frac{2K_{e}{}^{n}_{2,j-\frac{1}{2}}}{\Delta y_j(\Delta y_j + \Delta y_{j-1})} + \frac{\rho_{l}{}^{n}_{2,j-1}\hat{C}_{pl}{}^{n}_{2,j-1} v_{lk}{}^{n}_{2,j-1}}{\Delta y_j}\right] T_{r}{}^{n}_{2,j-1} \\ & - \left[\frac{2K_{e}{}^{n}_{\frac{3}{2},j}}{\Delta x_2(\Delta x_2 + \Delta x_1)} + \frac{2K_{e}{}^{n}_{\frac{5}{2},j}}{\Delta x_2(\Delta x_3 + \Delta x_2)} + \frac{2K_{e}{}^{n}_{2,j-\frac{1}{2}}}{\Delta y_j(\Delta y_j + \Delta y_{j-1})}\right. \\ & \left. + \frac{2K_{e}{}^{n}_{2,j+\frac{1}{2}}}{\Delta y_j(\Delta y_{j+1} + \Delta y_j)} + \frac{\rho_{l}{}^{n}_{2,j}\hat{C}_{pl}{}^{n}_{2,j} v_{lk}{}^{n}_{2,j}}{\Delta y_j} + \frac{\left(\overline{\rho\hat{C}_p}\right)^{n}_{2,j}}{\Delta t_n}\right] T_{r}{}^{n}_{2,j} \\ & + \frac{2K_{e}{}^{n}_{\frac{5}{2},j}}{\Delta x_2(\Delta x_3 + \Delta x_2)} T_{r}{}^{n}_{3,j} + \frac{2K_{e}{}^{n}_{i,j+\frac{1}{2}}}{\Delta y_j(\Delta y_{j+1} + \Delta y_j)} T_{r}{}^{n}_{2,j+1} \end{aligned} \tag{3.46}$$

Similarly, during injection period, when $t \le t_{inj}$, at the fracture face (j = 2), we have,

$$AP = -\frac{\left(\overline{\rho\hat{C}_p}\right)_{i,2}^{n-1}}{\Delta t_n} \tag{3.47}$$

$$AW = \frac{2K_{e}{}_{i-\frac{1}{2},2}^{n}}{\Delta x_i(\Delta x_i + \Delta x_{i-1})} \tag{3.48}$$

$$AS = \frac{h_{l_i}}{\Delta y_2} + \frac{\rho_{l}{}_{i,1}^{n}\hat{C}_{pl}{}_{i,1}^{n} v_{lk}{}_{i,1}^{n}}{\Delta y_2} \tag{3.49}$$

$$\begin{aligned} AC = &-\frac{2K_{e}{}_{i-\frac{1}{2},2}^{n}}{\Delta x_i(\Delta x_i + \Delta x_{i-1})} - \frac{2K_{e}{}_{i+\frac{1}{2},2}^{n}}{\Delta x_i(\Delta x_{i+1} + \Delta x_i)} - \frac{h_{l_i}}{\Delta y_2} \\ &- \frac{2K_{e}{}_{i,\frac{5}{2}}^{n}}{\Delta y_2(\Delta y_3 + \Delta y_2)} - \frac{\rho_{l}{}_{i,2}^{n}\hat{C}_{pl}{}_{i,2}^{n} v_{lk}{}_{i,2}^{n}}{\Delta y_2} - \frac{\left(\overline{\rho\hat{C}_p}\right)_{i,2}^{n}}{\Delta t_n} \end{aligned} \tag{3.50}$$

$$AE = \frac{2K_{e}{}_{i+\frac{1}{2},2}^{n}}{\Delta x_i(\Delta x_{i+1} + \Delta x_i)} \tag{3.51}$$

$$AN = \frac{2K_{e}{}_{i,\frac{5}{2}}^{n}}{\Delta y_2(\Delta y_3 + \Delta y_2)} \tag{3.52}$$

The reservoir model should also cover the formation ahead of fracture tip and no-heat transfer boundary condition holds true due to the symmetry at *y* axis.

$$AP = -\frac{\left(\overline{\rho\hat{C}_p}\right)_{i,1}^{n-1}}{\Delta t_n} \tag{3.53}$$

$$AW = \frac{2K_{e}{}_{i-\frac{1}{2},1}^{n}}{\Delta x_i(\Delta x_i + \Delta x_{i-1})} \tag{3.54}$$

$$AS = 0 \tag{3.55}$$

$$AC = -\frac{2K_{e}{}^{n}_{i-\frac{1}{2},1}}{\Delta x_i(\Delta x_i + \Delta x_{i-1})} - \frac{2K_{e}{}^{n}_{i+\frac{1}{2},1}}{\Delta x_i(\Delta x_{i+1} + \Delta x_i)} - \frac{2K_{e}{}^{n}_{i,\frac{3}{2}}}{\Delta y_1(\Delta y_2 + \Delta y_1)} - \frac{\rho_{l}{}^{n}_{i,1}\hat{C}_{pl}{}^{n}_{i,1}v_{lk}{}^{n}_{i,1}}{\Delta y_1} - \frac{\left(\overline{\rho\hat{C}_p}\right)^{n}_{i,1}}{\Delta t_n} \tag{3.56}$$

$$AE = \frac{2K_{e}{}^{n}_{i+\frac{1}{2},1}}{\Delta x_i(\Delta x_{i+1} + \Delta x_i)} \tag{3.57}$$

$$AN = \frac{2K_{e}{}^{n}_{i,\frac{3}{2}}}{\Delta y_1(\Delta y_2 + \Delta y_1)} \tag{3.58}$$

At the far boundary when ($i = N_x, j = 1$) ahead of fracture tip, it is no-heat transfer boundary condition for both axial direction, the following spatial coefficients are applicable,

$$AP = -\frac{\left(\overline{\rho\hat{C}_p}\right)^{n-1}_{i,1}}{\Delta t_n} \tag{3.59}$$

$$AW = \frac{2K_{e}{}^{n}_{N_x-\frac{1}{2},1}}{\Delta x_{N_x}(\Delta x_{N_x} + \Delta x_{N_x-1})} \tag{3.60}$$

$$AS = 0 \tag{3.61}$$

$$AC = -\frac{2K_{e}{}^{n}_{N_x-\frac{1}{2},1}}{\Delta x_{N_x}(\Delta x_{N_x} + \Delta x_{N_x-1})} - \frac{2K_{e}{}^{n}_{N_x,\frac{3}{2}}}{\Delta y_1(\Delta y_2 + \Delta y_1)} - \frac{\rho_{l}{}^{n}_{N_x,1}\hat{C}_{pl}{}^{n}_{N_x,1}v_{lk}{}^{n}_{N_x,1}}{\Delta y_1} - \frac{\left(\overline{\rho\hat{C}_p}\right)^{n}_{N_x,1}}{\Delta t_n} \tag{3.62}$$

$$AE = 0 \tag{3.63}$$

$$AN = \frac{2K_{e_{i,\frac{3}{2}}}^{n}}{\Delta y_1(\Delta y_2 + \Delta y_1)} \tag{3.64}$$

3.5 Solution Procedure of the Integrated Forward Model

To solve these models to simulate temperature distribution along the wellbore respect to real time, we couple these models and solve them simultaneously by integration of boundary conditions. The solution procedure of the integrated forward model for single stage fracturing treatment shows in **Fig. 3.9** (Li and Zhu, 2016).

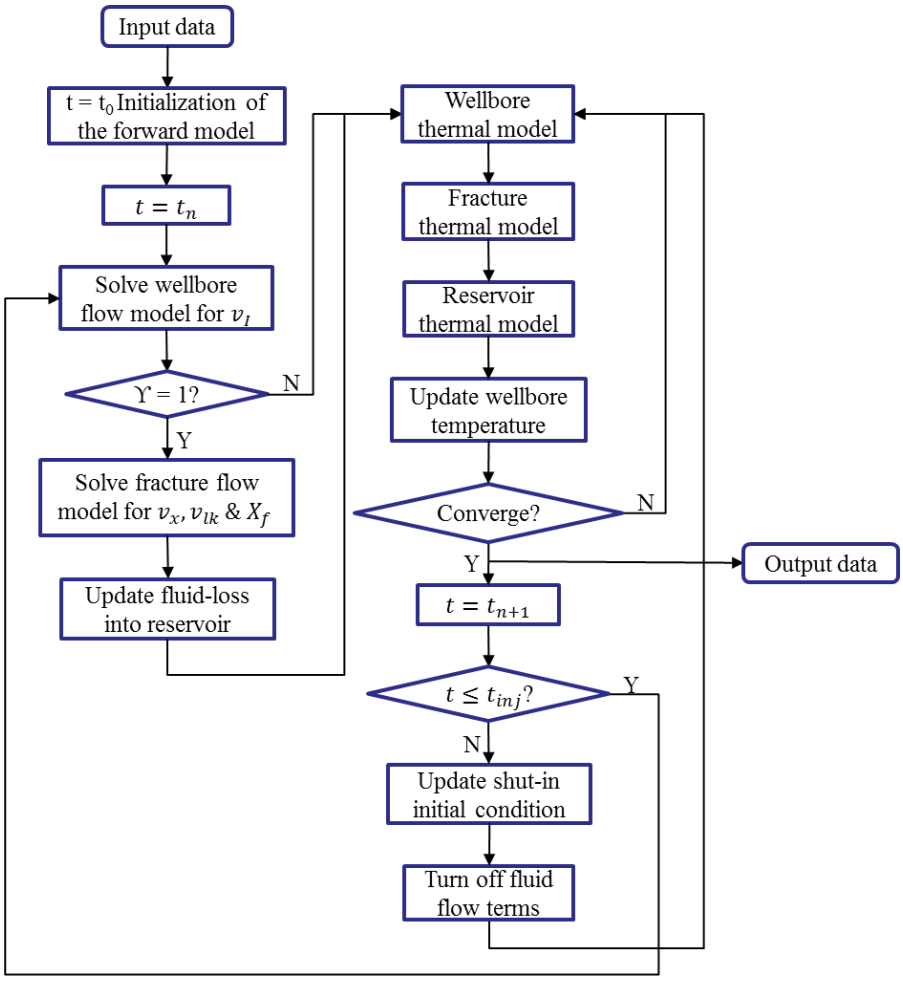

Fig. 3.9 Solution procedure for single stage fracturing treatment (Li and Zhu, 2016)

Figure 3.9 shows that at each time step for single stage fracturing, the forward model solves the wellbore flow model first to obtain the fracturing fluid velocity at the perforation location. When there is a fracture, the model continues to solve the fracture flow model to obtain the fracture half-length and the injection fluid velocity inside fracture, as well as fluid-loss into the reservoir. Then, the wellbore, fracture and reservoir thermal model are coupled and solved simultaneously. After the injection time has been ceased, the forward model automatically starts the shut-in period. There is no fluid flow during shut-in, thus, the invaded reservoir region, the fracture and the wellbore are warmed up by the geothermal formation. The fluid and temperature profile at the end of injection is used as the initialization for shut-in.

For multi-stage fracturing treatments in a horizontal well, real time schedule is introduced to the wellbore model. Due to the zonal isolation between each stage, the wellbore can be divided into multiple segments. Based on the real-time control, the coupled integrated model is called for each segment during injection and shut-in periods respectively. For plug and perf fracturing stimulation operations, shut-in period can be several hours between stages, a sequential simulation method is applied to calculate temperature distribution for each segment from toe to heel in the well. A multistage fracturing solution procedure is shown in **Fig. 3.10** (Li and Zhu, 2016),

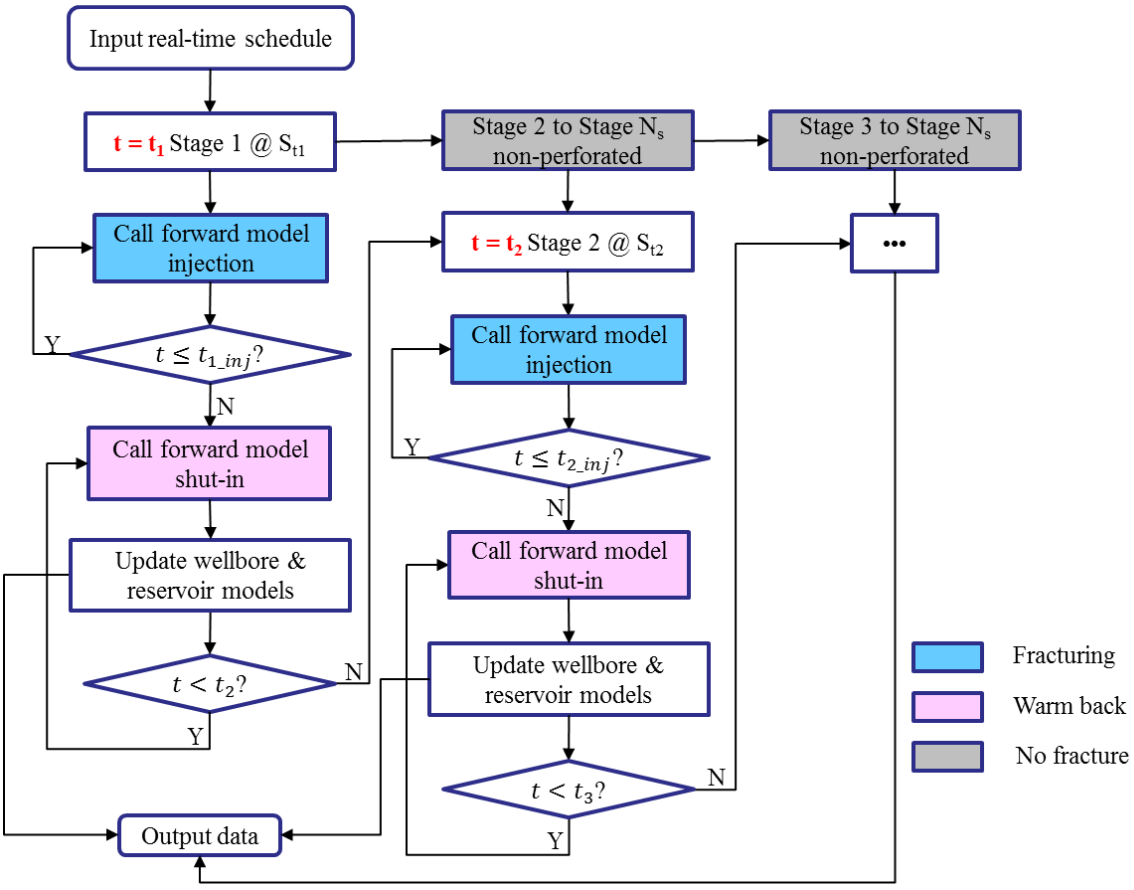

Fig. 3.10 Solution procedure for multistage fracturing treatments (Li and Zhu, 2016)

The above schematic shows the solution procedure for multistage fractures stimulation. One can find that the forward model is run for different stages respect to the location of current fracturing treatment. The temperature distribution is updated along the well from toe to heel. Upstream of the current fracture, the shut-in model is applied, and downstream of the current facture, only heat conduction between wellbore and reservoir exist.

4. FORWARD MODEL VALIDATION

In this chapter, the developed forward model is validated with analytical solution for specific condition when the analytical solution is available, and compared with Yoshida's numerical solution as well for fracture and reservoir model respectively. The wellbore model adopted here presented by Yoshioka (2007) and Sui (2009) have been validated in their previous work, and hence, the wellbore model validation is not repeated in this study.

4.1 Comparison with Analytical Solutions

The fracture and reservoir energy conservation equations are solved numerically to account for time and space dependent fluid-loss and transient thermal model coupling. However, an analytical solution is available to solve for fracture temperature when assuming there is no fluid-loss, and a constant reservoir temperature is considered. The Green function solution can be used to solve for heat transfer by conduction in the reservoir thermal model without fluid-loss convection heat transfer. The simplified energy conservation equations and analytical solutions are presented in the following sections.

4.1.1 Comparison with Fracture Analytical Solution

Assuming there is no fluid-loss, a constant injection flowrate into the fracture, and the temperature in the reservoir is constant and equals to the initial reservoir geothermal temperature. The fracture energy conservation equation (Eq. (2.37)) can be reduced to,

$$\rho_l \hat{C}_{pl} \frac{\partial T_l}{\partial t} = -\frac{\rho_l \hat{C}_{pl} v_x \partial T_l}{\partial x} + \frac{2h_l (T_r - T_l)}{w} \tag{4.1}$$

With the following initial and boundary conditions:

$$I.C. \quad T_l = T_i, \qquad at\ t = 0 \tag{4.2}$$

$$B.C.s \quad \begin{cases} T_l = T_{inj}, & at\ x = 0 \\ T_r = Const = T_i, & at\ all\ x, t \end{cases} \tag{4.3}$$

Introducing dimensionless variables T_D and Laplace transform variable ξ as,

$$T_D = \frac{T_i - T_l}{T_i - T_{inj}} \tag{4.4}$$

And,

$$\xi = \frac{2h_l}{\rho_l \hat{C}_{pl} w} \tag{4.5}$$

We can rewrite Eq. (4.1) as

$$\frac{\partial T_D}{\partial t} = -v_x \frac{\partial T_D}{\partial x} - \xi T_D \tag{4.6}$$

And the initial and boundary conditions become to,

$$T_D = 0, at\ t = 0 \tag{4.7}$$

$$T_D = 1, at\ x = 0 \tag{4.8}$$

In domain η, we can rewrite Eq. (4.6) as,

$$\eta \widetilde{T_D}(x, \eta) - T_D(x, 0) = -v_x \frac{\partial \widetilde{T_D}}{\partial x} - \xi \widetilde{T_D}(x, \eta) \tag{4.9}$$

Where, $\widetilde{T_D}$ is the dimensionless temperature in η domain. The boundary condition can also be written in η domain,

$$\widetilde{T_D} = \frac{1}{\eta}, \qquad at\ x = 0 \tag{4.10}$$

Apply the initial condition of Eq. (4.7) in Eq. (4.9), we obtain,

$$(\eta + \xi)\widetilde{T_D}(x,0) + v_x \frac{\partial \widetilde{T_D}}{\partial x} = 0 \tag{4.11}$$

By multiplying the integration term, the above equation becomes to,

$$e^{\frac{x(\xi+\eta)}{v_x}}(\eta + \xi)\widetilde{T_D}(x,\eta) + e^{\frac{x(\xi+\eta)}{v_x}} v_x \frac{\partial \widetilde{T_D}}{\partial x} = 0 \tag{4.12}$$

In which, $e^{\frac{x(\xi+\eta)}{v_x}}$ is the integration term, manipulate Eq. (4.12) yields,

$$\frac{\partial}{\partial x}\left(\widetilde{T_D} e^{\frac{x(\xi+\eta)}{v_x}}\right) = 0 \tag{4.13}$$

Using the boundary condition of Eq. (4.10) and rearrange, we have,

$$\widetilde{T_D} = \frac{1}{\eta} e^{-\frac{x(\xi+\eta)}{v_x}} \tag{4.14}$$

The solution in the dimensionless form using inverse of Laplace transform gives,

$$T_D = 1 \qquad when\ (x - v_x t) > 0 \tag{4.15}$$

$$T_D = 1 - e^{-x\frac{\xi}{v_x}} \qquad when\ (x - v_x t) < 0 \tag{4.16}$$

Therefore, the fracture temperature is given by,

$$T_l = T_i - T_D(T_i - T_{inj}) \tag{4.17}$$

In order to compare the developed fracture model solution with the above analytical solution, a case study is presented here. As discussed previously, the fluid-loss is neglected, and the reservoir temperature is considered to be constant during the injection period. In other words, the fracture is propagating with a constant fluid flow velocity and constant boundary condition.

In the calculation of the analytical solution, a constant fracture geometry is used. While the fracture is propagating during the injection period in the forward fracture

thermal model calculation. The fracture half-length incremental is set as a constant value and the time step for each grid block of the fracture propagation is calculated in this case. The treatment schedule is listed in **Table 4.1**. The fluid and reservoir properties used in the numerical simulation and analytical solution calculation is listed in **Table 4.2**.

Table 4.1 Treatment design parameters

Treatment Design	SI Unit	Field Unit
Injection time, t_{inj}	3085.8 s	51.43 min
Injection rate, q_{inj}	0.0605 m^3/s	22.83 bpm
Fracture width, w	0.0061 m	0.02 ft
Fracture height, h	48.768 m	160 ft
Fracture half-length, X_f	313.844 m	1029.671 ft
Fracture half-length incremental size, Δx	4.1846 m	13.729 ft

Table 4.2 Fracturing fluid and reservoir properties

Property	SI Unit	Field Unit
Reservoir initial geothermal temperature, T_i	114.65 °C	238.37 °F
Fracturing fluid injection temperature (heel), T_{inj}	26.67 °C	80 °F
Reservoir porosity, ϕ	0.08	0.08
Reservoir rock density, ρ_r	2380.023 kg/m^3	148.58 lbm/ft^3
Fracturing fluid density, ρ_l	985.904 kg/m^3	61.548 lbm/ft^3
Reservoir rock thermal conductivity, K_r	1.6 J/(m-s-K)	0.000257 Btu/(ft-s-°F)
Reservoir fluid thermal conductivity, K_f	0.6626 J/(m-s-K)	0.000106 Btu/(ft-s-°F)
Fracturing fluid thermal conductivity, K_l	0.6626 J/(m-s-K)	0.000106 Btu/(ft-s-°F)
Reservoir rock heat capacity, C_{pr}	844.06 J/(kg-K)	0.2016 Btu/(lbm-°F)
Reservoir fluid heat capacity, C_{pf}	4135.72 J/(kg-K)	0.9878 Btu/(lbm-°F)
Fracturing fluid heat capacity, C_{pl}	4135.72 J/(kg-K)	0.9878 Btu/(lbm-°F)
Heat transfer coefficient, h_l	58.6 $J/(m^2\text{-s-K})$	0.002867 $Btu/(ft^2\text{-s-°F})$

Based on the given input parameters, the analytical solution can be obtained, as well as the numerical simulation temperature profile in the fracture. The results are presented and compared at the end of injection, shown in **Figs. 4.1** and **4.2**.

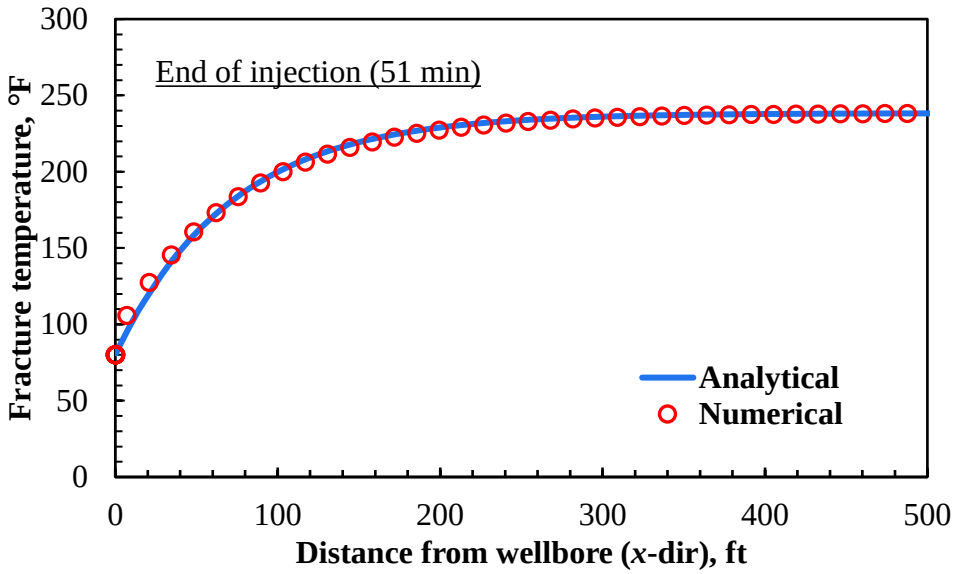

Fig. 4.1 Fracture temperature comparison with analytical solution

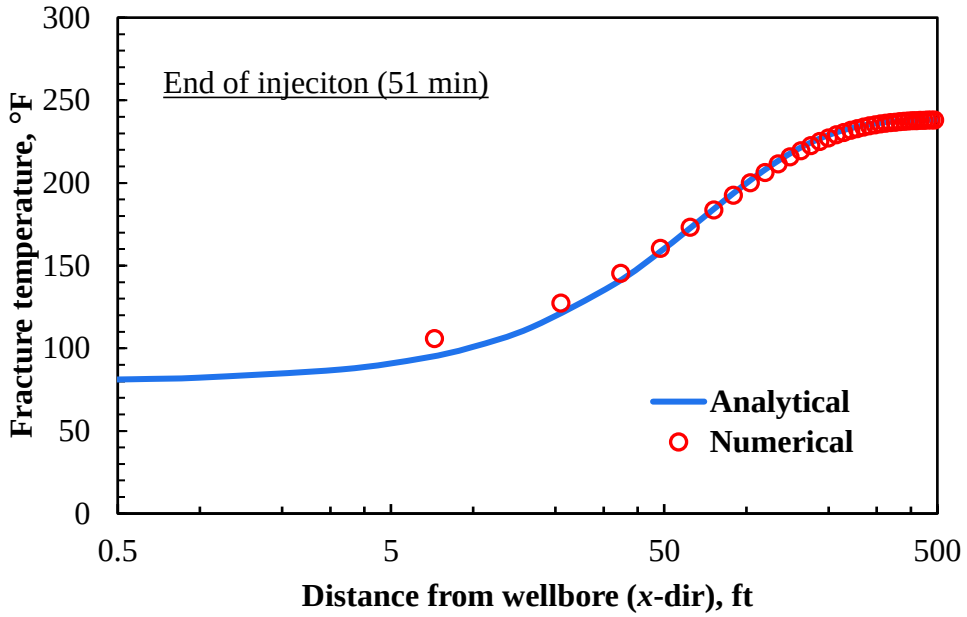

Fig. 4.2 Fracture temperature comparison with analytical solution in log scale

From **Figs. 4.1** and **4.2**, we see that the fracture temperature profile simulated by our numerical model has a good match with the analytical solution.

4.1.2 Comparison with Reservoir Analytical Solution

The reservoir thermal model is also validated during shut-in period with an analytical solution when reduce the energy balance equation to 1-D heat diffusion with no heat transfer at outer boundary. In order to investigate the temperature distribution along the wellbore direction in the reservoir, we assume there is not fluid loss and the heat conduction in the fracture propagating direction is ignored. Thus, Eq. (2.65) is simplified as,

$$\overline{\rho \hat{C}_p} \frac{\partial T_r}{\partial t} - \frac{\partial}{\partial y}\left(K_e \frac{\partial T_r}{\partial y}\right) = 0 \tag{4.18}$$

Additionally, assume it is an isotropic reservoir with homogeneous reservoir thermal conductivity. And the temperature profile along the wellbore direction at the end of injection $f(y)$ is used as the initial condition of shut-in period. We can write the following initial and boundary conditions,

$$I.C. \quad T_r(y) = f(y), \qquad at\ t = 0 \tag{4.19}$$

$$B.C.s \quad \begin{cases} \dfrac{\partial T_r}{\partial y} = 0, & at\ y \to \infty \\ \dfrac{\partial T_r}{\partial y} = 0, & at\ y = \dfrac{w}{2} \end{cases} \tag{4.20}$$

The Green's Function is used to solve for Eq. (4.18). The heat kernel derived for Green's Function is,

$$G(y,t) = \frac{1}{\sqrt{4\pi kt}} e^{\frac{-y}{4kt}} \tag{4.21}$$

Equation (4.21) is the solution of Eq. (4.18) with singular initial data $\delta(y)$,

$$G(y,t) = \delta(y) \qquad at\ t = 0 \tag{4.22}$$

In other words, $G(y,t)$ satisfies Equation (4.18),

$$\lim_{t\to 0} \int_{-\infty}^{\infty} G(y,t) f(y) dy = f(0) \tag{4.23}$$

The solution of this problem is Green's Function $G(y,t;\alpha)$ with initial data $\delta(y-\alpha)$,

$$G(y,t;\alpha) = G(y-\alpha,t) = \frac{1}{\sqrt{4\pi kt}} e^{\frac{-(y-\alpha)^2}{4kt}} \tag{4.24}$$

In which, α is a point in $(-\infty,\infty)$ and $\delta(y-\alpha)$ is a translation of $\delta(y)$ in space. Therefore, the analytical solution of Eq. (4.18) is given by,

$$T_r(y,t) = \int_{-\infty}^{\infty} G(y,t;\alpha) f(\alpha) d\alpha = \int_{-\infty}^{\infty} \frac{1}{\sqrt{4\pi kt}} e^{\frac{-(y-\alpha)^2}{4kt}} f(\alpha) d\alpha \qquad (4.25)$$

To compare the temperature profile simulated by the reservoir thermal model with the analytical solution solved by the Green's Function, the previous case is studied during shut-in period. The initial condition ($t = t_{inj}$) is calculated by using a constant fluid injection temperature in the fracture and initial reservoir geothermal temperature everywhere in the reservoir. The inner boundary at fracture face during shut-in period is no heat transfer closed boundary to decouple the fracture model. The input data is the same as **Tables 4.1** and **4.2**.

Figures 4.3 and **4.4** show the calculated reservoir temperature comparison from the end of injection till shut-in the well to one day. One can see that the two models have a good agreement. After injecting cold fracturing fluid for over 50 minutes in to the fracture, the cooling heat front travels only a couple of feet into the shale reservoir. In this case, reservoir temperature almost kept the initial geothermal temperature beyond 2 feet without fluid-loss.

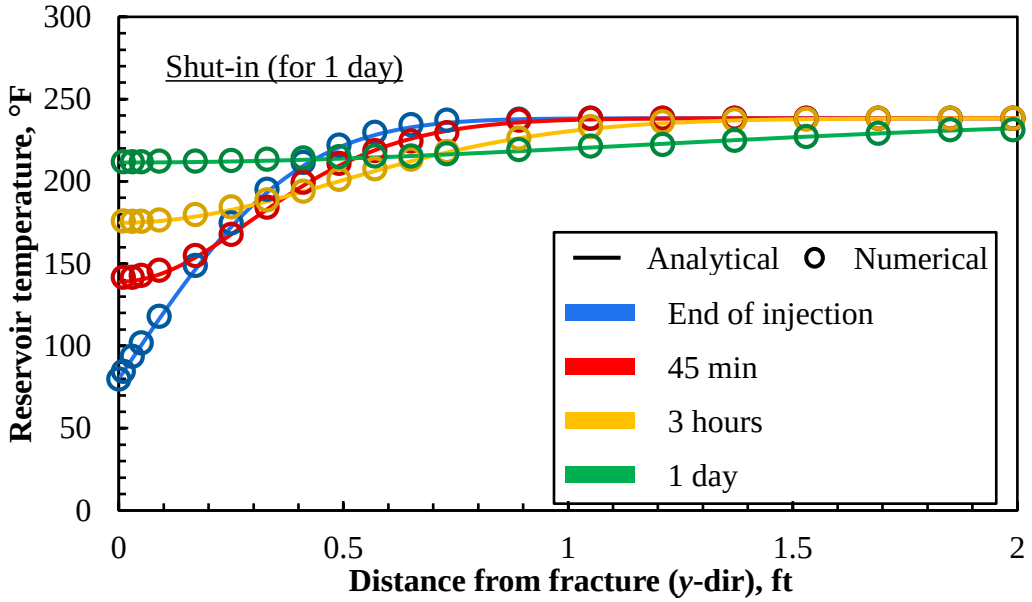

Fig. 4.3 Reservoir temperature comparison with analytical solution

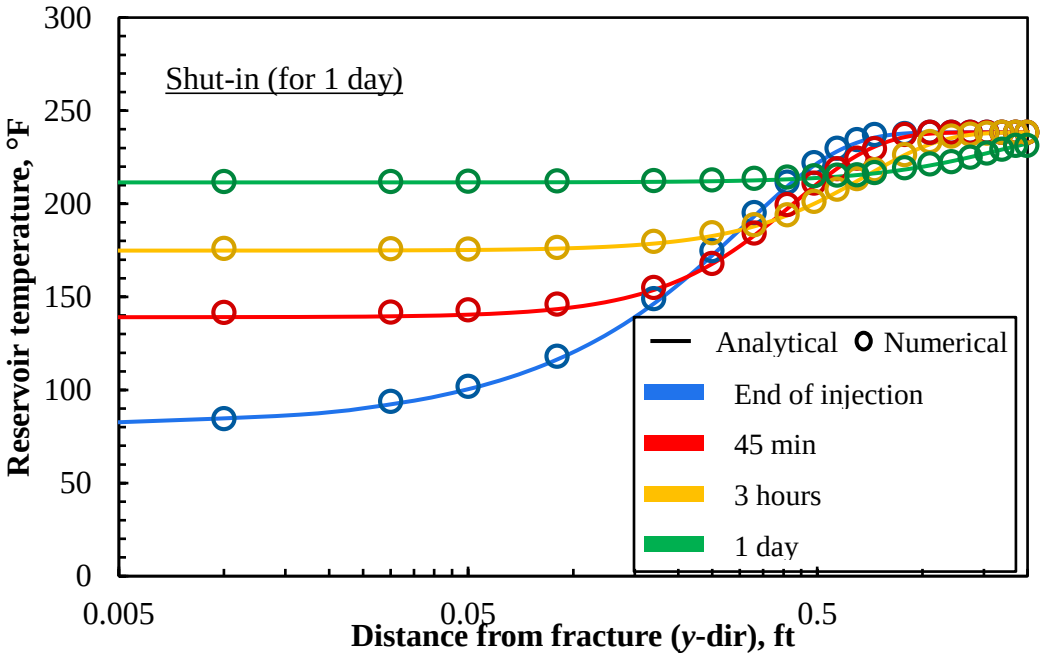

Fig. 4.4 Reservoir temperature comparison with analytical solution in log scale

4.2 Comparison with Numerical Solution

The numerical model developed by Yoshida (2013) considered thermal expansion and viscous dissipation in the thermal model during production period. The fracture property is assigned to certain grid blocks in the reservoir model to represent existing fracture. The fracture geometry is then assume to be constant during the whole production period. When assuming the same fracture geometry, the same boundary conditions, and the same input parameters in **Tables 4.1** and **4.2** during injection and shut-in periods, the fracture and reservoir thermal model presented in this study can be compared with Yoshida' model. In his model, the reservoir domain with fractures is described in the following figure,

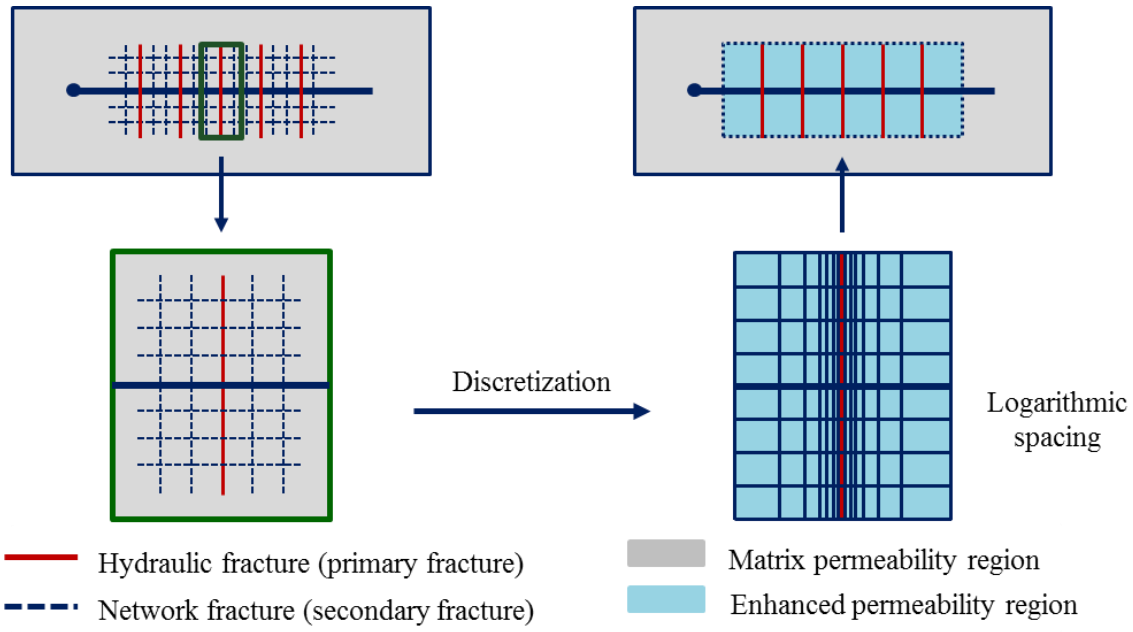

Fig. 4.5 Reservoir simulation domain with fractures by Yoshida (2013)

To compare the numerical thermal model presented in this study with Yoshida's reservoir simulation model, the fracture geometry is set to be the same by using a given fracture incremental half-length, Δx, based on the total injection time. The comparison of fracture temperature and reservoir temperature distribution are presented in the following.

4.2.1 Fracture Temperature Comparison

Assume there is no fluid-loss, and the input parameters are the same as the data shown in **Tables 4.1 and 4.2**. The solution of temperature distribution at the end of injection by the two numerical models are shown in the figures below.

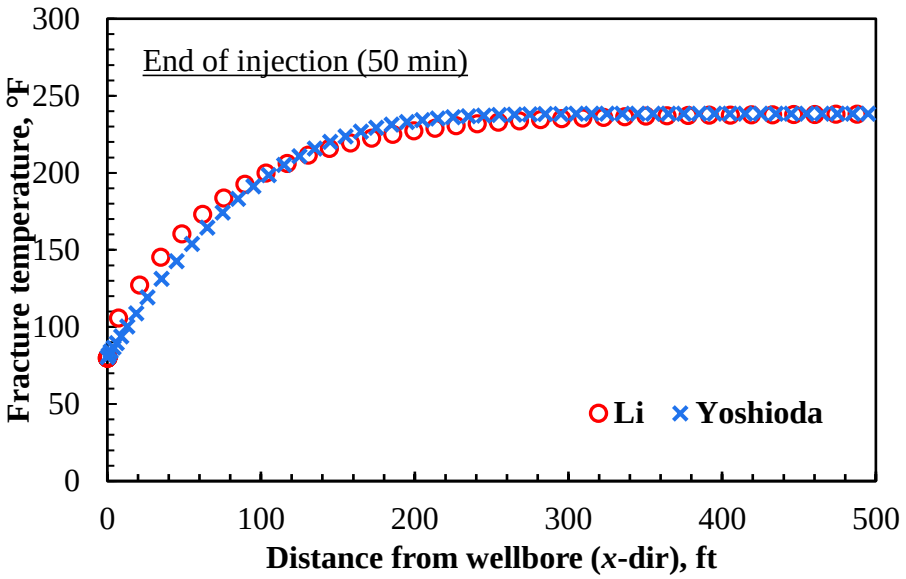

Fig. 4.6 Fracture temperature comparison for the two numerical models

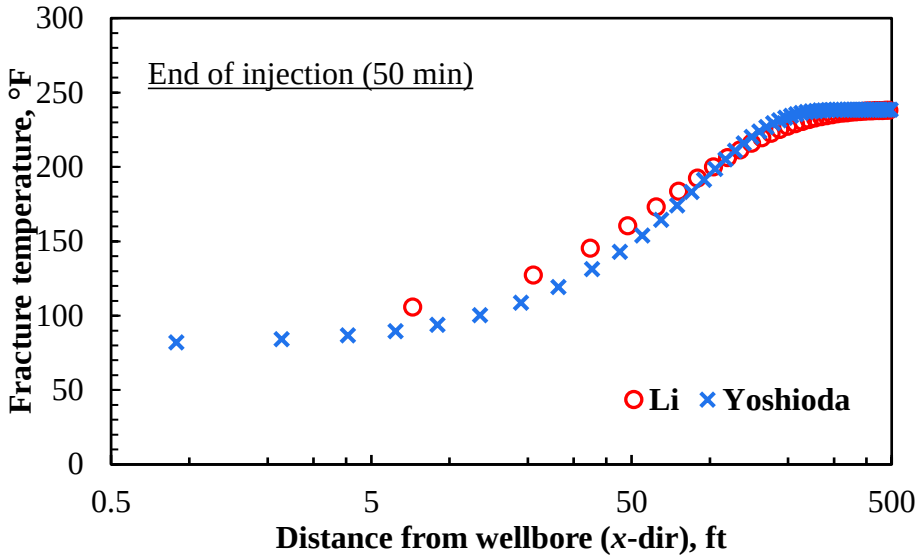

Fig. 4.7 Fracture temperature comparison for the two numerical models in log scale

From the above two figures, one can see that in hypothetical case, the two models validated each other well. However, the small difference between the two models are caused by the propagation of the fracture. In Yoshida's numerical model, the fracture is fixed geometry at the beginning of injection. However, in this study, the fracture is propagating and the grid blocks ahead of fracture tip is still formation rock matrix. Hence, at near wellbore region, the temperature calculated by the numerical model in this study is warmed up quicker by the surrounding formation comparing to Yoshida's model during injection period.

4.2.2 Reservoir Temperature Comparison

To compare the reservoir temperature profile during shut-in period, the initial temperature distribution should be the same. The inner and outer boundaries are assumed to be no heat flow closed boundary to decouple with the fracture and wellbore model and

validate the reservoir thermal model. The following figures show the temperature solution comparison up to shut-in the well for one day. The reservoir contains formation rock and reservoir fluid. As the shut-in of well starts, the reservoir at near wellbore location is heated up by the surrounding geothermal temperature. And the longer of the shut-in period lasts, the more uniform of the reservoir temperature intend to be. Eventually, the reservoir temperature warms back to the initial reservoir geothermal temperature. In this case, with no fluid-loss, and typical shale reservoir input parameters, we found that the cold fluid heat front traveled only a few feet into the reservoir.

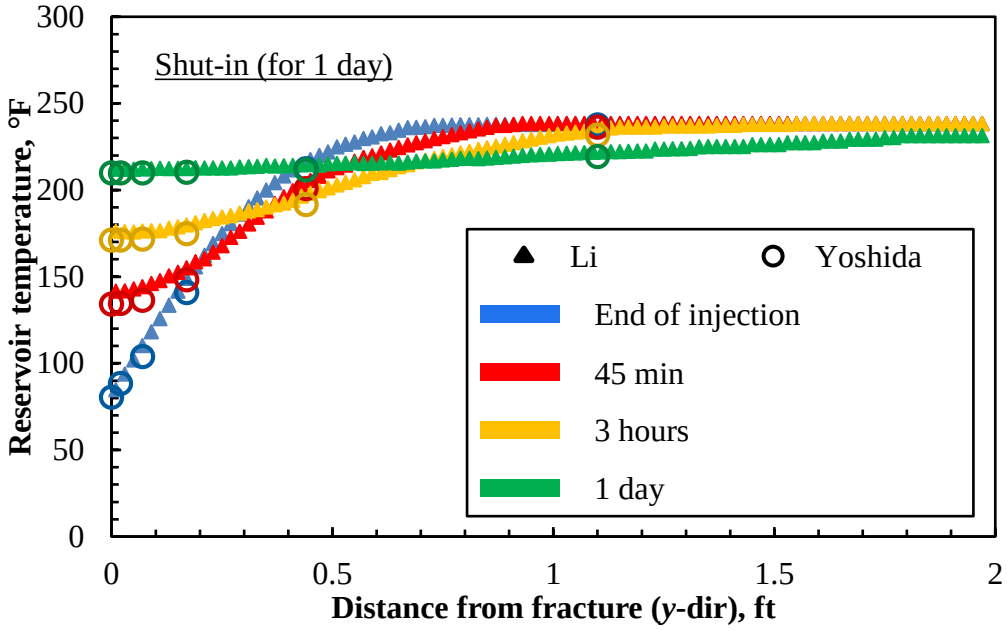

Fig. 4.8 Reservoir temperature comparison for the two numerical models

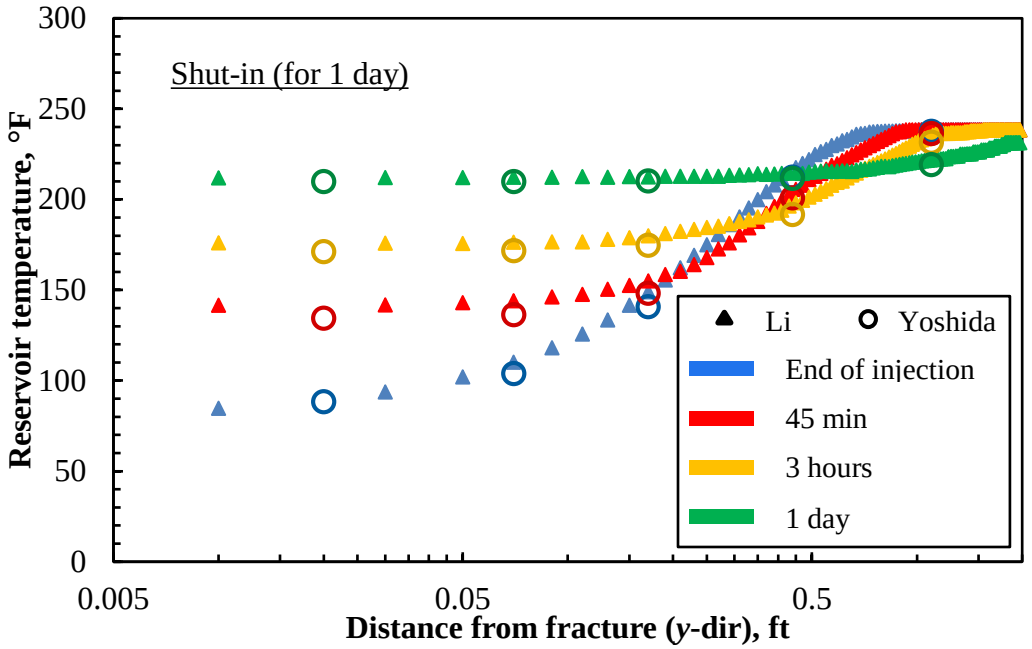

Fig. 4.9 Reservoir temperature comparison for the two numerical models in log scale

Based on above comparisons, we know that the integrated thermal model developed in this study has a good agreement with reservoir simulation model. Both numerical models are 2-D and can simulate temperature distribution in the fracture and reservoir. However, for the purpose of studying temperature responses during injection and shut-in period, the integrated forward model is much more efficient and is able to take fracture propagation and fluid-loss accumulation into account.

The fracture and reservoir thermal model are validated separately in this chapter, and the wellbore thermal model is validated in the previous study. For the fully coupled wellbore, fracture and reservoir model, synthetic cases are studied in Chapter 5, as well as the effect of fluid distribution and fracture and reservoir properties, on simulated temperature profile.

5. RESULTS AND DISCUSSION

5.1 Introduction

In the previous chapters, an integrated forward model to predict temperature distribution during multistage fracturing treatments in horizontal wells is developed. The forward model also compared with analytical solutions and reservoir simulations. In this chapter, comprehensive synthetic case study is presented to illustrate the application of the integrated forward model on transient temperature simulation. Sensitivity studies of fluid distribution, fracture and reservoir properties are also discussed within the examples.

First, the fully coupled model is applied to a single traverse fracture system to investigate fracture propagation, fluid distribution, and temperature distribution in the fracture and reservoir. A single-stage fracturing treatment with multiple clusters is then studied to demonstrate the effect of fluid distribution, leak-off coefficient and formation thermal conductivity on temperature behavior. For multistage fracturing treatment, real time control is introduced to the forward model, and the simulated temperature responses at DTS measurement locations along the wellbore is shown in the result under different circumstances.

Due to the complex heat transfer problem, observed temperature distribution is affected by many critical parameters, such as injection rate, flowrate distribution between fractures, leak-off coefficient, fracture scales, fracturing fluid and reservoir properties. Moreover, treatment schedule, well completion methods, and possible DTS deployment locations are also considered to be important for the temperature behavior near wellbore.

5.2 Synthetic Case Studies

In the forward model, fracture propagation, fluid-loss front in the reservoir and temperature distribution in the wellbore, fracture and reservoir are simulated. A synthetic case of single stage fracturing treatment in a horizontal well in a shale reservoir is presented.

5.2.1 Single Stage Single Fracture Analysis

A comprehensive case study for the fully coupled forward model with single traverse fracture is presented here. The schematic of the simulated domain is shown in **Fig. 5.1**. Typical shale gas reservoir properties are used to initialize the input of the numerical model. The treatment schedule, fluid and reservoir parameters are given in **Tables 5.1** and **5.2** for the base case.

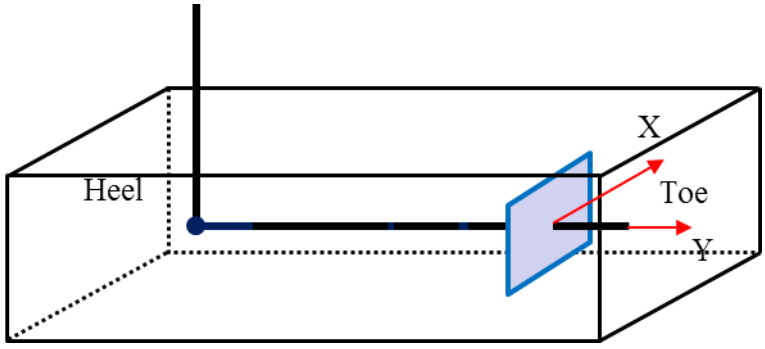

Fig. 5.1 Horizontal well with single traverse fracture in a shale reservoir

Table 5.1 Fracture and treatment parameters of the base case

Fracture & Treatment Parameter	SI Unit	Field Unit
Injection time, t_{inj}	3600 s	60 min
Injection rate, q_{inj}	0.053 m^3/s	20 bpm
Fracture width, w	0.0061 m	0.24 in
Fracture height, h	45.72 m	150 ft
Hole ID, R_o	0.22 m	8.75 in
Casing OD, R_{ocs}	0.14 m	5.5 in
Casing ID, R_{cs}	0.116 m	4.548 in
Simulation time step, Δt	120 s	2 min

For multistage fracturing treatments in horizontal wells, injection rate as high as 90 bpm is used in each stage with 4-5 clusters (Mayerhofer et al., 2011). Considering single traverse fracture for the base case, an injection rate of 20 bpm is used here. **Table 5.2** lists the properties of the reservoir and well system.

Table 5.2 Reservoir, injection fluid, and wellbore properties

Property	SI Unit	Field Unit
Reservoir initial geothermal temperature, T_i	157.22 °C	315 °F
Fracturing fluid injection temperature (heel), T_{inj}	37.77 °C	100 °F
Reservoir porosity, ϕ	0.045	0.045
Reservoir rock density, ρ_r	2380 kg/m^3	148.6 lbm/ft^3
Reservoir fluid density, ρ_f	420 kg/m^3	26.22 lbm/ft^3
Fracturing fluid density, ρ_l	993.144 kg/m^3	62 lbm/ft^3
Casing density, ρ_{cs}	7752.931 kg/m^3	484 lbm/ft^3
Cement density, ρ_{cm}	3149.228 kg/m^3	196.6 lbm/ft^3
Reservoir rock thermal conductivity, K_r	1.606 J/(m-s-K)	0.000257 Btu/(ft-s-°F)
Reservoir fluid thermal conductivity, K_f	0.6813 J/(m-s-K)	0.000109 Btu/(ft-s-°F)
Fracturing fluid thermal conductivity, K_l	0.9313 J/(m-s-K)	0.000149 Btu/(ft-s-°F)
Casing thermal conductivity, K_{cs}	10 J/(m-s-K)	0.0016 Btu/(ft-s-°F)
Cement thermal conductivity, K_{cm}	3.63 J/(m-s-K)	0.000581 Btu/(ft-s-°F)
Reservoir rock heat capacity, C_{pr}	845.73 J/(kg-K)	0.202 Btu/(lbm-°F)
Reservoir fluid heat capacity, C_{pf}	4178.43 J/(kg-K)	0.998 Btu/(lbm-°F)
Fracturing fluid heat capacity, C_{pl}	4178.43 J/(kg-K)	0.998 Btu/(lbm-°F)
Casing heat capacity, C_{pcs}	490 J/(kg-K)	0.117 Btu/(lbm-°F)
Cement heat capacity, C_{pcm}	916 J/(kg-K)	0.22 Btu/(lbm-°F)
Total average leak-off coefficient, C_{lk}	3.048E-5 m/s$^{1/2}$	0.0001 ft/s$^{1/2}$

Typical shale reservoir rock and fluid properties values from "*Enhanced Oil Recovery*" (Lake, 2010) are used as initial inputs. Injection water thermal properties at specific temperature is considered. The leak-off coefficient for a shale gas reservoir without natural fractures is applied for the base case.

Fracture half-length can be calculated using the fracture flow model, here, assuming the injection flow rate keeps constant during the injection period. The result is shown in **Fig. 5.2.** One can see that the fracture half-length is increasing during the injection period and the increasing rate is getting slower. This is caused by fluid-loss accumulation during the injection period. With a constant injection rate and constant simulation time step size, the injection fluid flowrate inside fracture is decreasing due to the fluid-loss to the reservoir. As we have a higher injection rate, the fracture is longer at the same injection time. However, when we have a much higher leak-off coefficient, the fracture length decreases fast. This may happen if there are natural factures existing in the system. More sensitivity studies about fluid-loss is discussed later in the chapter.

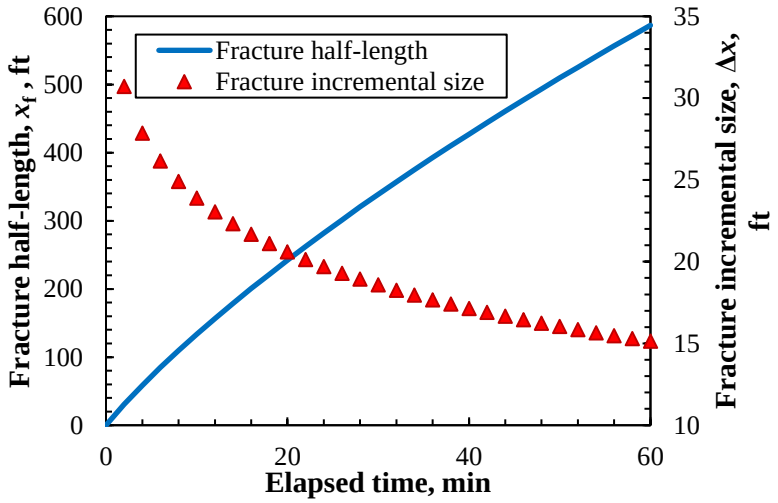

Fig. 5.2 Fracture half-length and incremental size of the base case for constant time step

To investigate the cooling effect around the fracture in the reservoir, we need to calculate the distance of leak-off fluid travels into the reservoir from fracture faces. It can

be calculated by integrating the fluid-loss velocity with respect to leak-off area and time. The figure below shows the fluid-loss front travels to the reservoir at different injection time along the fracture propagation direction. We can tell that the leak-off fluid keeps traveling in the reservoir due to the high injection pressure and formation porous media. The average fluid-loss velocity is inversely proportional to the square root of time. Thus, the fluid-loss velocity is decreasing as a function of injection time. From **Fig. 5.3**, we see that near wellbore region has the most leak-off accumulation, and it contributes to the cooling effect near wellbore during injection period.

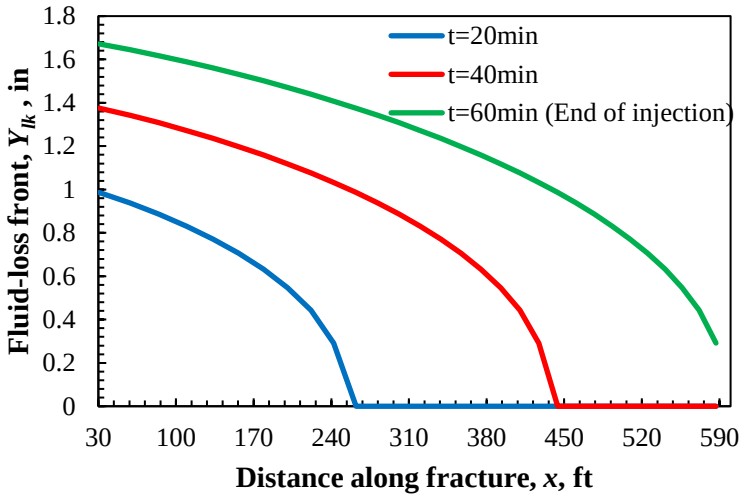

Fig. 5.3 Fluid-loss front along the fracture during injection period

The forward model can be used to simulate the temperature distribution in the wellbore, fracture and reservoir at any time and any location. At the initiation of the fracture, water based fracturing fluid is injected into the formation, and the fracture assumes to have unity porosity. The fracture temperature distribution can be calculated as

fracturing fluid temperature. During the injection period, the cold fracturing fluid flows into the formation under high pressure and meanwhile is heated up by the surrounding formation. The temperature distribution of fracturing fluid in the fracture during injection and shut-in period is shown in **Fig. 5.4**.

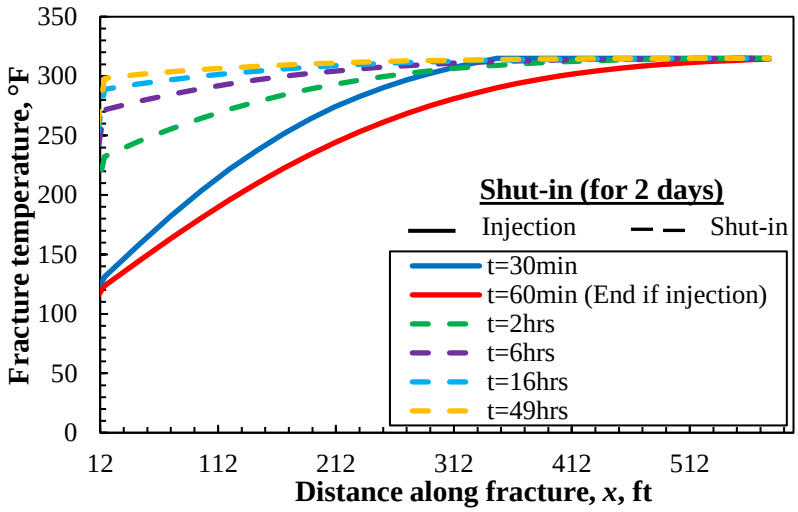

Fig. 5.4 Fracture temperature profile of the base case during injection and shut-in

From the above figure, we see that during injection period, the fracture is propagating and the fracture temperature decrease as we injected more cold fluid. Once we shut-in the well, the fracturing fluid is warmed up quickly by the surrounding formation. The boundary condition as described in Chapter 2, Model Development, is injection temperature and injection rate calculated by the wellbore model at the perforation location. No heat transfer at far boundaries in the reservoir. In this figure, temperature at the center of each fracture gird is shown. The fist grid block has the largest Δx when using

a constant injection rate and constant simulation time step as we discussed in previous chapters.

The reservoir temperature profile can also be calculated by the forward thermal model. **Fig. 5.5** shows the reservoir temperature profile at the middle of fracture along well direction. Due to the heat conduction and fluid-loss convection between the fracture and the formation during injection, the reservoir temperature near fracture is lowest and remain the same as initial reservoir temperature further away from the fracture. During shut-in, the reservoir and its contained invaded injection fluid are warmed up by the formation and the temperature profile tend to be uniform and closer to the initial geothermal temperature. For the base case with an injection rate of 20 bpm, the temperature remains the initial reservoir temperature beyond a couple of feet from the fracture in the formation, and the temperature is different to initial reservoir temperature near the fracture region even after two days of shut-in.

Figure 5.5 displays the reservoir temperature profile at the middle of the fracture. The casing temperature from the fracture along the wellbore is also presented in **Fig. 5.6**. For multistage fracturing treatments in horizontal wells with plug and perf completion design, the distributed temperature sensors are normally deployed outside the casing. Hence, the study of casing temperature can help us to interpret DTS measured data and have a better understanding of the coupled temperature behavior during fracturing treatment. From **Fig. 5.6**, we can clearly see the cooling effect of the wellbore fluid flow comparing with the reservoir temperature profile shown in **Fig. 5.5**. And at the beginning of shut-in, the casing temperature keeps decreasing until certain point, then starts to be

heated up. This is because we use reservoir geothermal temperature to initialize casing temperature. During injection, casing is cooled down by the fracturing fluid quickly. However, heat conduction happens until the casing temperature reaching thermal equilibrium with wellbore fluid and surrounding formation. If we shut-in the well in this process, the casing temperature is affected by both the cooling effect from the wellbore cold fluid and warming effect from the reservoir. Additionally, the casing temperature is sensible to the thermal properties of the material in the well system. **Fig. 5.6** shows casing temperature profile until shut-in the well for two days, when we can still see a significant lower temperature response compare to the reservoir initial geothermal temperature.

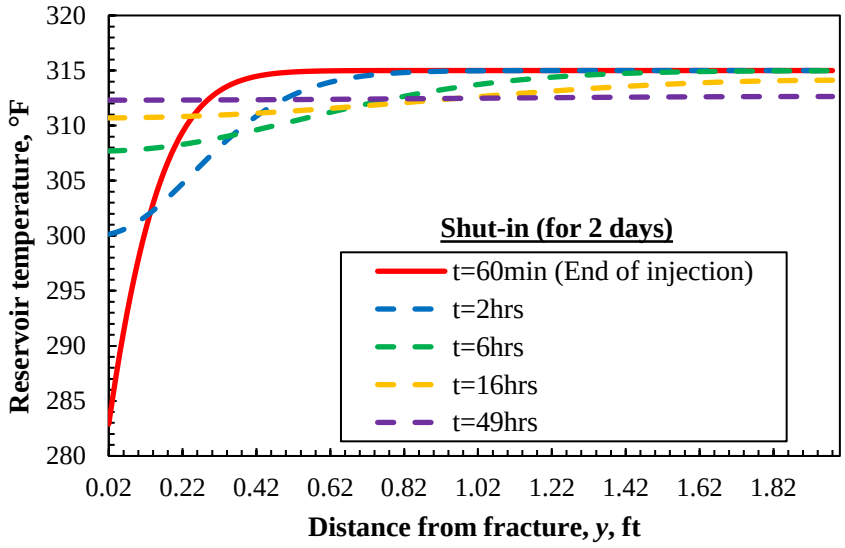

Fig. 5.5 Reservoir temperature profile of the base case during shut-in

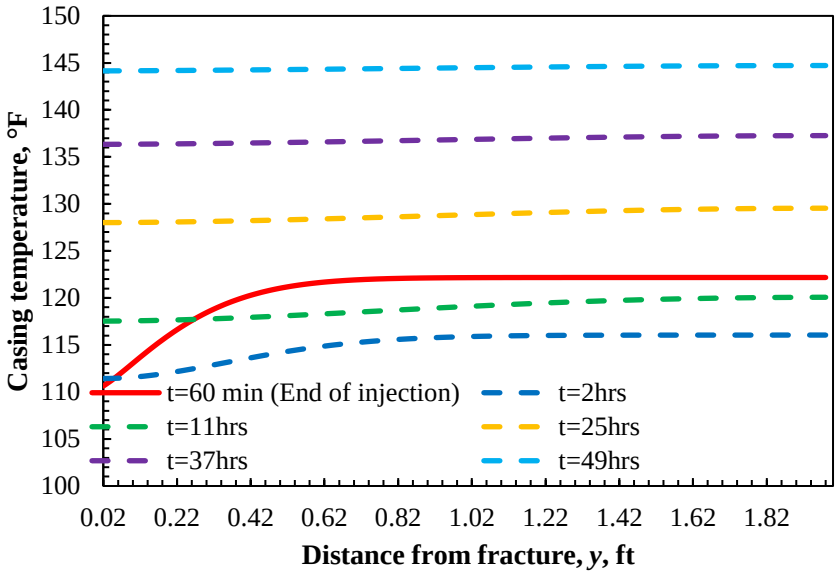

Fig. 5.6 Casing temperature profile of the base case during shut-in

Figure 5.7 shows the temperature maps for the fully coupled system throughout the whole single fracture treatment. **Fig. 5.7a** and **5.7b** display the temperature map during injection. And **Fig. 5.7c** to **5.7d** present the temperature map at different time step during shut-in. These temperature maps show half of the reservoir domain, where, $x = 0$ is the symmetrical line at the center of the horizontal well. From these temperature maps, we see that during injection, the temperature profile has a sharp low temperature region as a result of the heat convection of injection fluid flow is dominant under high injection rate. During shut-in, the temperature profile is more dispersed due to the heat conduction.

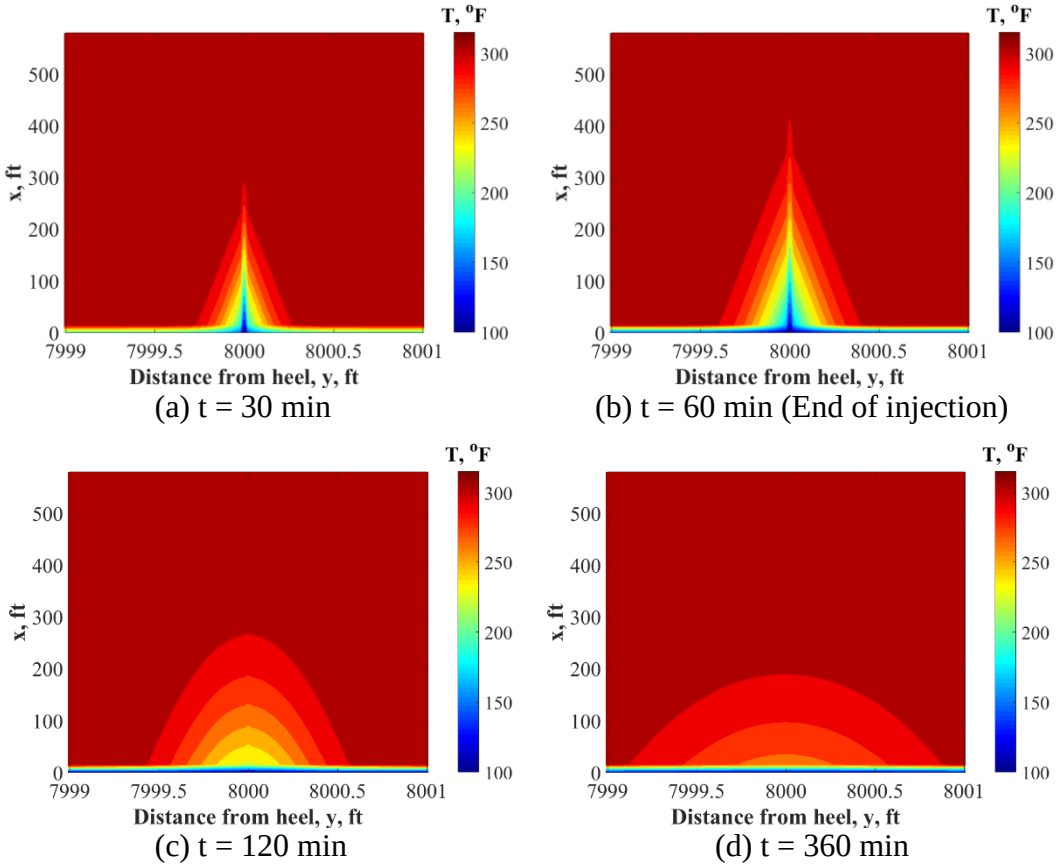

(a) t = 30 min (b) t = 60 min (End of injection)

(c) t = 120 min (d) t = 360 min

Fig. 5.7 Temperature map of the single-fracture system during fracturing treatment at various time steps

5.2.2 Sensitivity Study of Single Fracture System

During fracturing treatment, injection rate plays an important role on fracture propagation and temperature behavior. As presented before in this study, the fracture half-length is proportional to the injection rate, and the temperature distribution is then affected directly by the fracture scale. Also, the heat flux caused by injection fluid flow is critical to calculated temperature profile in the complex flow system during fracturing treatment.

Temperature maps at the end of injection and a specific time of shut-in for different injection rates are presented here. For single fracture system, injection rate of 10 bpm and

30 bpm are compared with the base case of 20 bpm. The rest of input parameters are kept the same as shown in **Tables 5.1** and **5.2**. The fracture half-length calculated corresponding to different injection rates is shown in **Table 5.3**.

Table 5.3 Fracture half-length for different injection rates

Injection rate, q_{inj}	Fracture half-length, X_f
10 bpm	293 ft
20 bpm	587 ft
30 bpm	880 ft

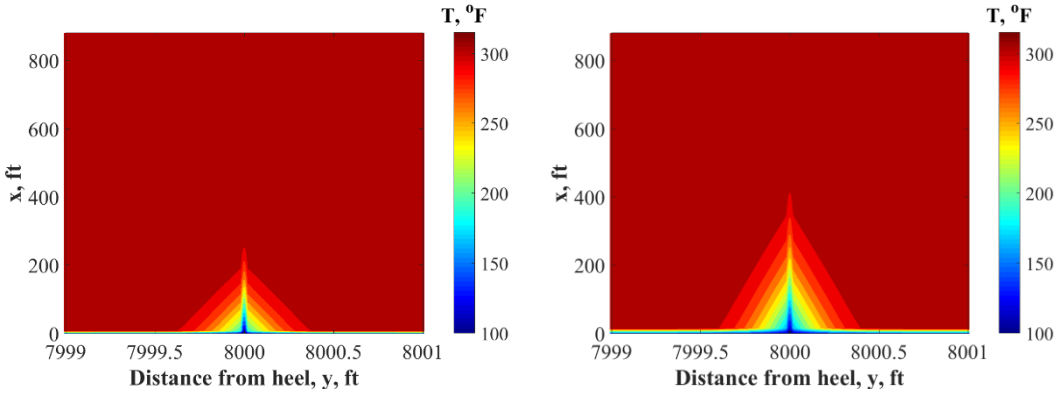

(a) q = 10 bpm (b) q = 20 bpm

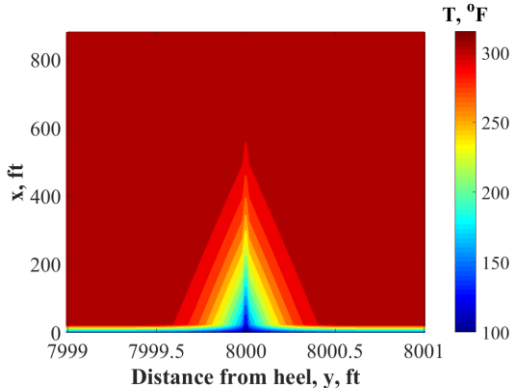

(c) q = 30 bpm

Fig. 5.8 Temperature map of the single fracture system at the end of injection (60 mins) for various injection rates

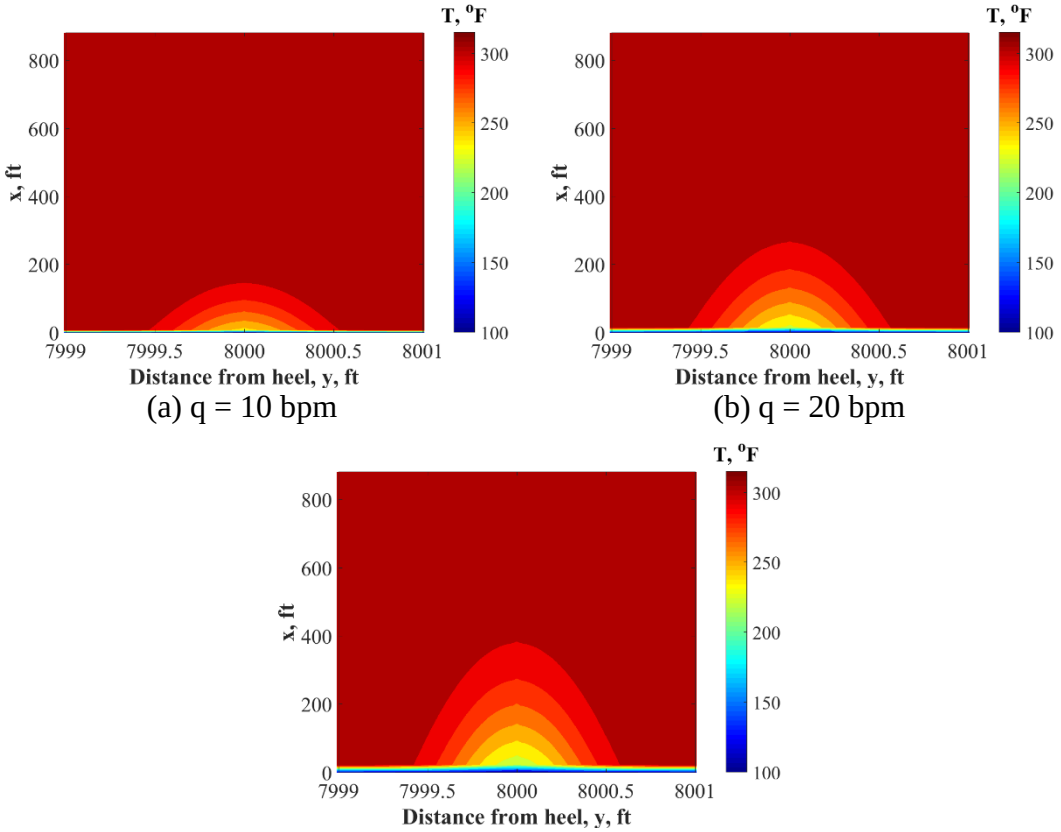

(a) q = 10 bpm (b) q = 20 bpm

(c) q = 30 bpm

Fig. 5.9 Temperature map of the single fracture system at 1 hour after shut-in for various injection rates

As presented in Chapter 2, reservoir properties have strong impact on leak-off coefficient. When there are natural fractures existed in the reservoir, or complex hydraulically induced discrete fractures have been created, the fluid-loss as a result can increase dramatically, which can be represented by using higher value of leak-off coefficient. In order to investigate the effect of leak-off amount on fracture propagation and temperature behavior of such scenarios, various leak-off coefficients are considered and the simulated results are compared. In **Fig. 5.10**, fracture half-length and leak-off front are displayed for different values of leak-off coefficient.

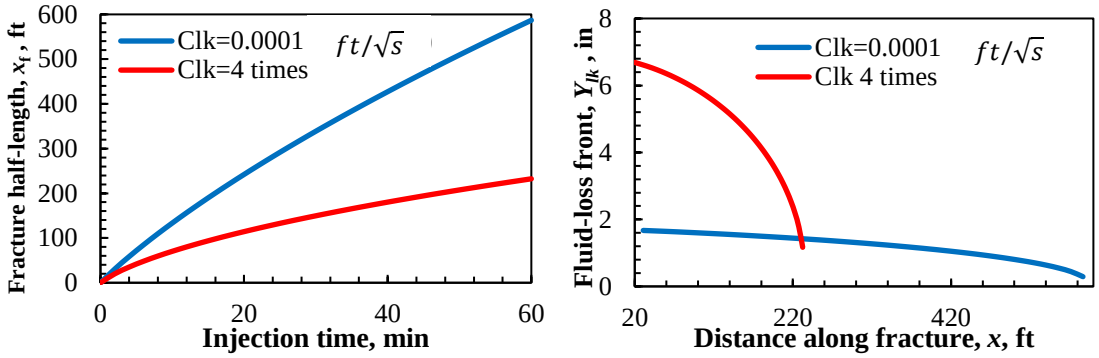

(a) Fracture half-length (b) Leak-off front

Fig. 5.10 Fracture half-length and distance of leak-off front travels into the reservoir for various leak-off coefficients during injection

By increasing leak-off coefficient 4 times, we see the difference in fracture half-length and leak-off with the base case. Fracture half-length decreases (**Fig. 5.10a**). From **Fig. 5.10b**, we see that the fluid-loss travels further into the reservoir at near wellbore region for higher leak-off coefficients.

Temperature behavior is also sensitive to leak-off coefficient. Temperature map for the base case ($C_{lk} = 0.0001\ ft/\sqrt{s}$), and 4 times of leak-off coefficients are presented in **Figs. 5.11** and **5.12** during injection and shut-in respectively. We see that as leak-off coefficient increases, the temperature map is less sharp, and the heat flux is more dispersed at near wellbore region. From the comparison of **Figs. 5.11** and **5.12**, we see that the effect of leak-off coefficient on temperature distribution is more obvious during shut-in period because of the heat transfer is much slower than the injection fluid flow.

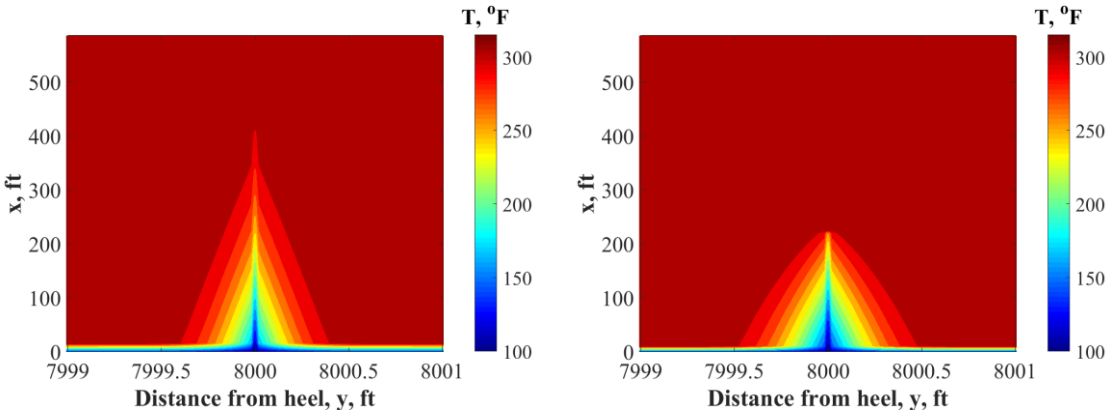

(a) $C_{lk} = 0.0001\ ft/\sqrt{s}$ (b) 4 times C_{lk}

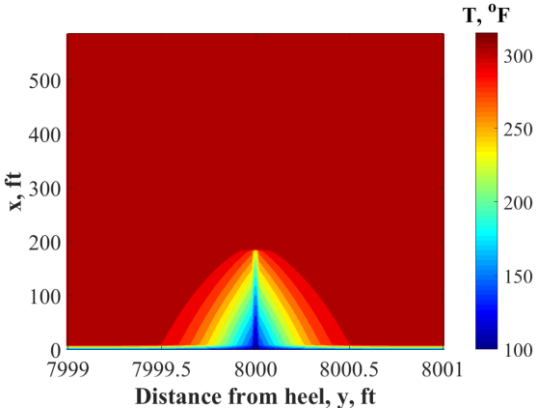

(c) 5 times C_{lk}

Fig. 5.11 Temperature map of the single fracture system at the end of injection (60 mins) for various leak-off coefficients

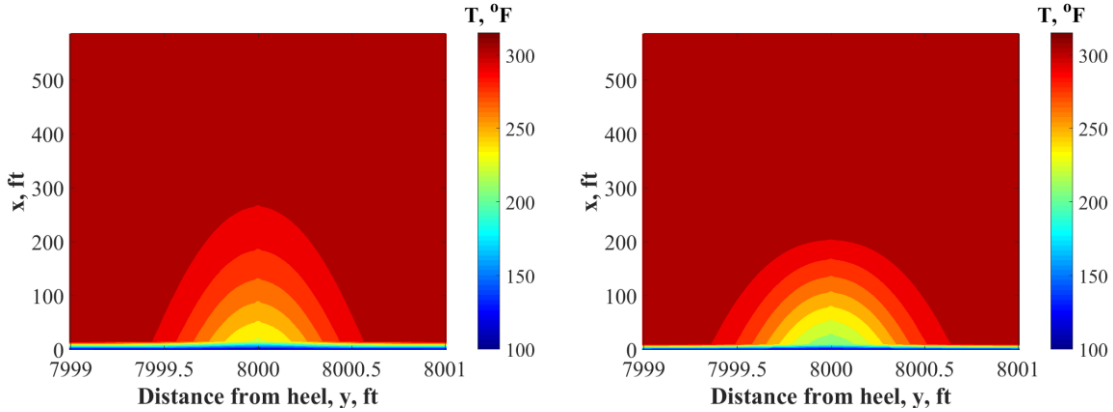

(a) $C_{lk} = 0.0001\ ft/\sqrt{s}$ (b) 4 times C_{lk}

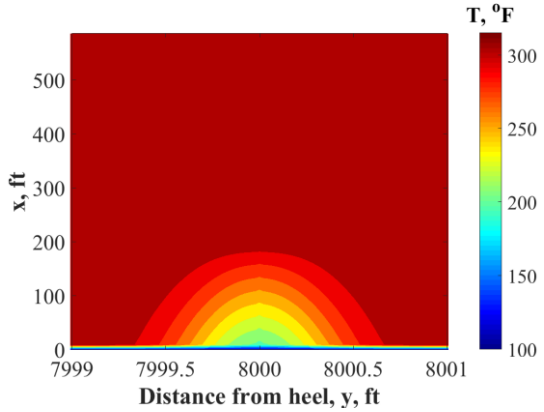

(c) 5 times C_{lk}

Fig. 5.12 Temperature map of the single fracture system at 1 hour after shut-in for various leak-off coefficients

Temperature behavior highly depends on reservoir thermal properties during fracturing treatment. Temperature profile is relatively sensitive to the reservoir thermal conductivity due to the dominant role of heat conduction during shut-in. In order to investigate the effect of reservoir thermal conductivity on temperature behavior during fracturing treatment, three cases are compared, including $K_r = 0.000257\ Btu/(ft - s - °F)$ (base case), and thermal conductivities of 2 times higher, and 4 times higher.

From **Fig. 5.13**, we observe that near wellbore region with heat convection caused by fluid-loss during injection, the cold heat flux travels faster when having a higher rock thermal conductivity. On the contrary, during shut-in period, heat conduction becomes the dominant phenomena. One can clearly see the warm-up process is much faster when using higher rock thermal conductivity based on **Fig. 5.14**.

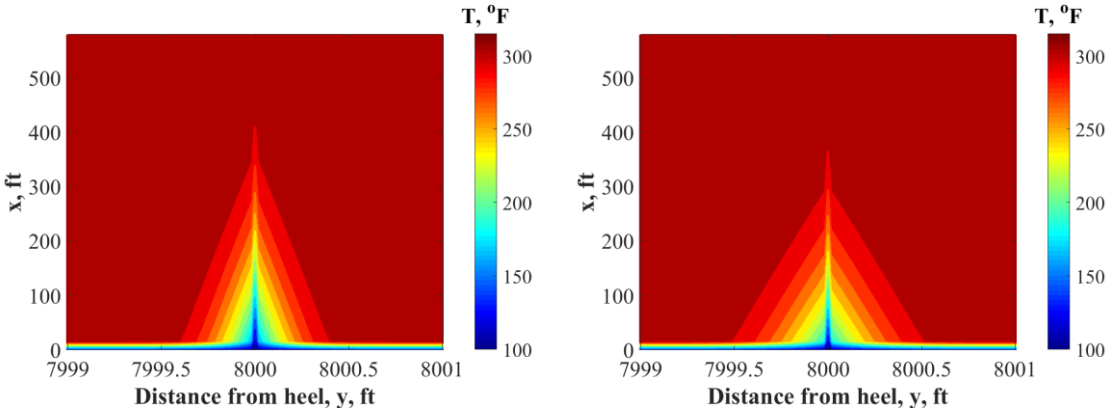

(a) $K_r = 0.000257\ Btu/(ft - s - °F)$ (b) 2 times K_r

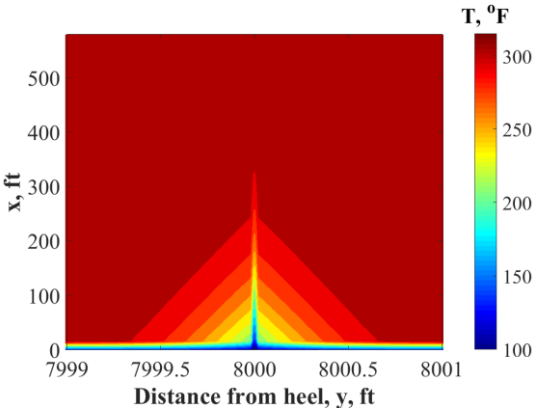

(c) 4 times K_r

Fig. 5.13 Temperature map of the single fracture system at the end of injection (60 mins) for various reservoir rock thermal conductivities

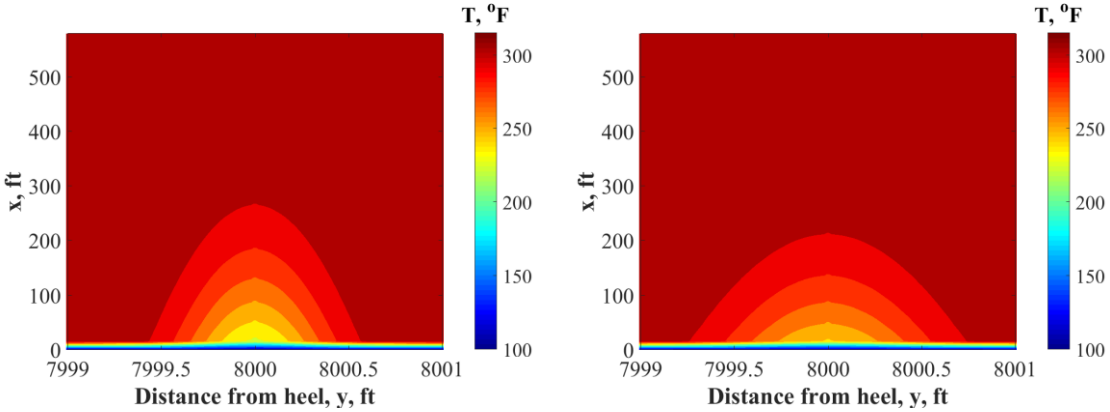

(a) $K_r = 0.000257\ Btu/(ft - s - °\text{F})$ (b) 2 times K_r

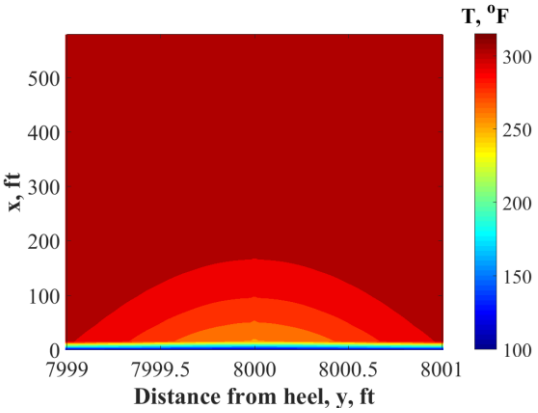

(c) 4 times K_r

Fig. 5.14 Temperature map of the single fracture system at 1 hour after shut-in for various reservoir rock thermal conductivities

To simulate DTS measured temperature profile along the wellbore, we have to understand multiple thermal coupling scenarios in DTS cables. Sierra et al. (2008) stated that the location of fiber, conveyed with coiled tubing inside the wellbore or cemented behind the casing, has a major impact in the temperature response, depending on the thermal conductivity between the fiber cable and injected fluid path. **Fig. 5.15** shows both thermal coupling scenarios in DTS cables. When the DTS conveyed with coiled tubing, it

measures the injection fracturing fluid temperature inside wellbore, when the DTS attached outside of casing, the response from DTS is casing surface temperature. Therefore, based on understanding of these thermal coupling scenarios, measured DTS temperature data can be better interpreted under different circumstances.

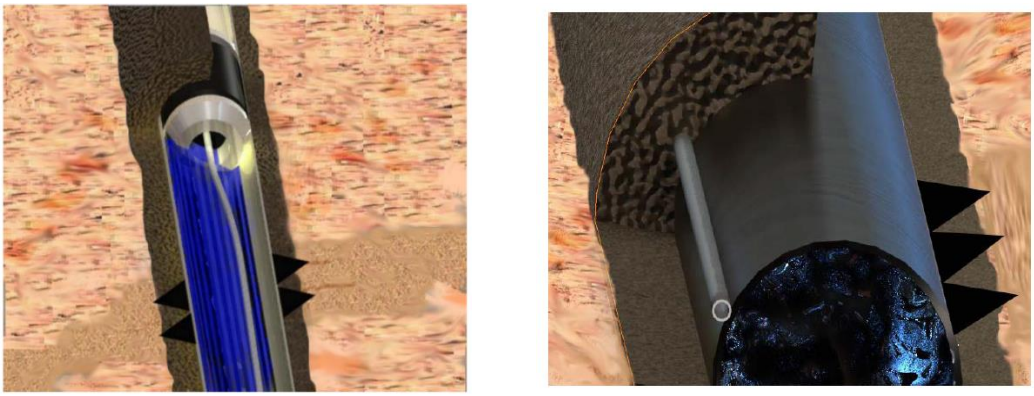

Fig. 5.15 Thermal coupling scenarios in DTS cables (Sierra et al., 2008)

The integrated forward model is able to simulate temperature profile for different DTS cable couplings scenarios. **Fig. 5.16** displays the temperature response in the wellbore, casing, and near well reservoir (the middle of the first reservoir grid block attached to the wellbore and fracture, 15 ft into the reservoir) locations during the fracturing treatment.

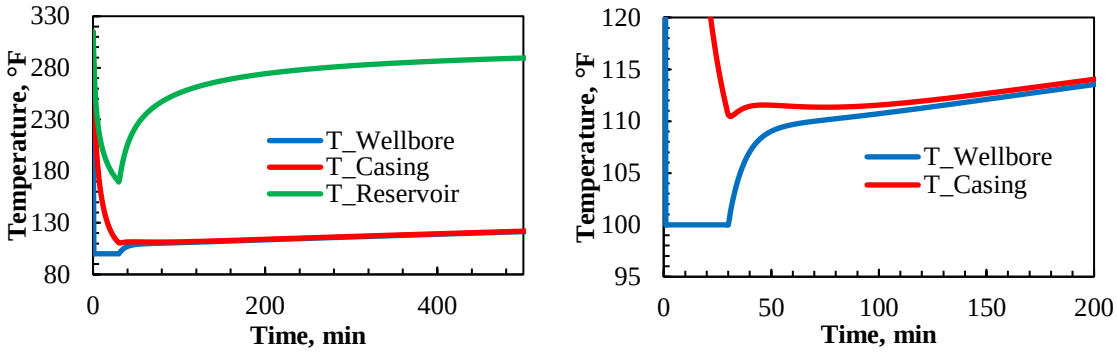

(a) Temperature at well, casing, and reservoir (b) Enlarged well and casing temperature

Fig. 5.16 Simulated temperature profiles for different DTS thermal coupling scenarios for the single fracture system during injection and shut-in

From the above plot, we see that when DTS cable is deployed inside the wellbore, it is measuring the injection fluid temperature. Therefore, during injection, it shows constant injection fluid temperature. The temperature starts rising once the well is shut-in. More details between wellbore and casing is showing in **Fig. 5.16b**. It shows the temperature difference inside wellbore and outside of casing during treatment. We found that the temperature difference is getting smaller after shut-in the well. Specifically, the casing temperature is showing the thermal effect from both the surrounding formation and the injection fluid inside wellbore. In order to have better diagnosis of the fracturing treatment, good coupling scenario of DTS attached outside of casing is discussed in the following.

5.2.3 Single Stage with Multiple Fractures

The integrated forward model is able to simulate temperature distribution for multiple fractures in the same stage. The propagation of multiple fractures is considered simultaneously. To investigate the effect of fluid volume on temperature behavior, we compared the simulated temperature profile if we distribute the total injection volume into two equal fractures instead of one, and the input for this investigation is listed in **Table 5.4**. The simulated temperature result is displayed in **Fig. 5.17**. Under the ideal condition, the temperature respond distinctly for one large fracture compared with two smaller fractures. The cooling locations are clear indication of the locations of created fractures. This feature can be used to determine the number of fractures are created in one stage. The cooling depth into the reservoir both along the fracture and perpendicular to the fracture is different for one fracture case compared with two fractures case. The temperature behavior does provide useful information after shut-in for fracture. Large fractures with deeper cooling recover slower than smaller fractures.

Table 5.4 Number of clusters and corresponding fracture half-length at the same total injection rate

Injection rate, bpm	Cluster number	Fracture spacing, ft	Fracture half-length, ft
30	1	0	880
30	2	40	440

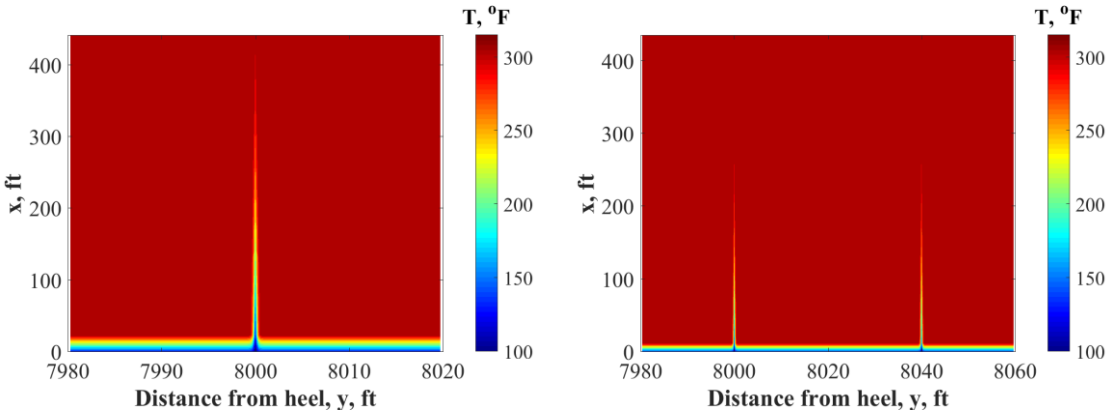

(a) Single fracture (b) Two identical fractures

Fig. 5.17 Temperature map of single-stage with single fracture and two identical fractures at the end of injection for the same total injection rate: 30 bpm per stage

A single-stage fracturing treatment with multiple clusters is studied to investigate the effect of injection fluid distribution and relative fracture scale on temperature behavior. Each cluster contains a fracture at the perforation location. For example, **Fig. 5.18** shows the reservoir domain of a horizontal well after stage one treatment with 5 fractures at the toe.

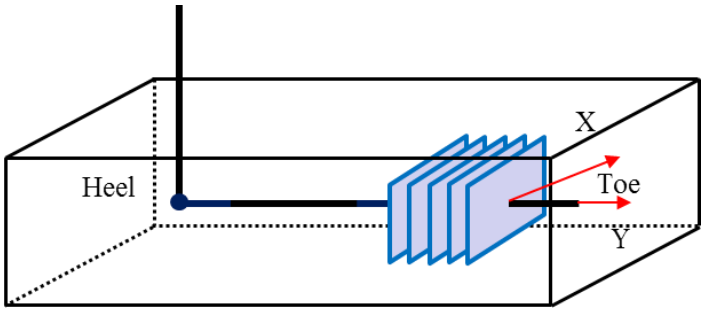

Fig. 5.18 Horizontal well single stage fracturing treatment with 5 fractures

The injection rate of multistage fracturing treatments in shale reservoirs can be as high as 90 bpm (Mayerhofer et al., 2011). Here, an example of both identical and non-identical fractures temperature map is plotted. The treatment design and reservoir properties are the same as the parameters shown in **Table 5.1** and **5.2**, and the fluid distribution is presented in **Table 5.5**.

Table 5.5 Fracture half-length for non-uniform fluid distribution in single-stage

Single-Stage at 60 bpm					
Cluster number	1	2	3	4	5
Injection rate, bpm	20	8	15	5	12
Fracture half-length, ft	587	235	440	147	352

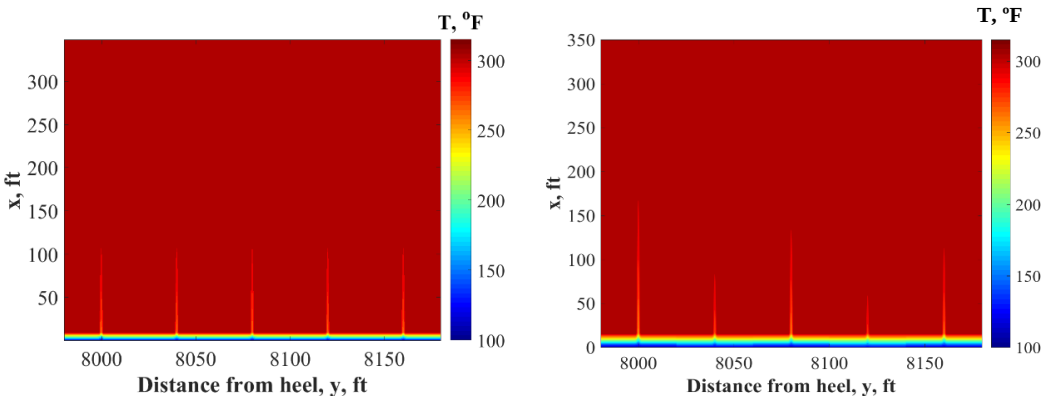

(a) Identical fractures (b) Non-identical fractures

Fig. 5.19 Temperature map of single-stage with 5 fractures for uniform and non-uniform fluid distributions at shut-in 5 hours for the same total injection rate (60 bpm per stage)

In reality, multiple fractures at the same stage are normally non-identical due to complex stress field with highly heterogeneous and non-isotropic reservoir properties in

shale plays. **Fig. 5.19b** shows an obvious different temperature response between these 5 fractures in same stage compare to the uniform fluid distribution in **Fig. 5.19a**. We also find that the temperature response directly reflects the fluid scale form **Fig. 5.19b**. The further the temperature signal can be captured in the reservoir, the higher injection rate the perforation takes, and we can still read this temperature difference after shut-in the well from the warm back temperature behavior.

5.3 Simulated DTS Temperature Analysis

As presented in the single fracture analysis, the casing temperature can be calculated by the integrated forward thermal model. Casing temperature profile along the wellbore for a single fracture system of the base case at 20 bpm is shown in **Fig. 5.20**. We see the fracture location has the lowest temperature profile during treatment. As mentioned before, at the beginning of shut-in, the casing temperature along wellbore away from fracture shows a delay of warm back due to the temperature convergence with the wellbore injection fluid. And at later shut-in period, casing is heated up by the formation. Until two days of shut-in, the casing temperature is still much lower than the reservoir initial geothermal temperature. Hence, we may interpret DTS data to allocate fractures.

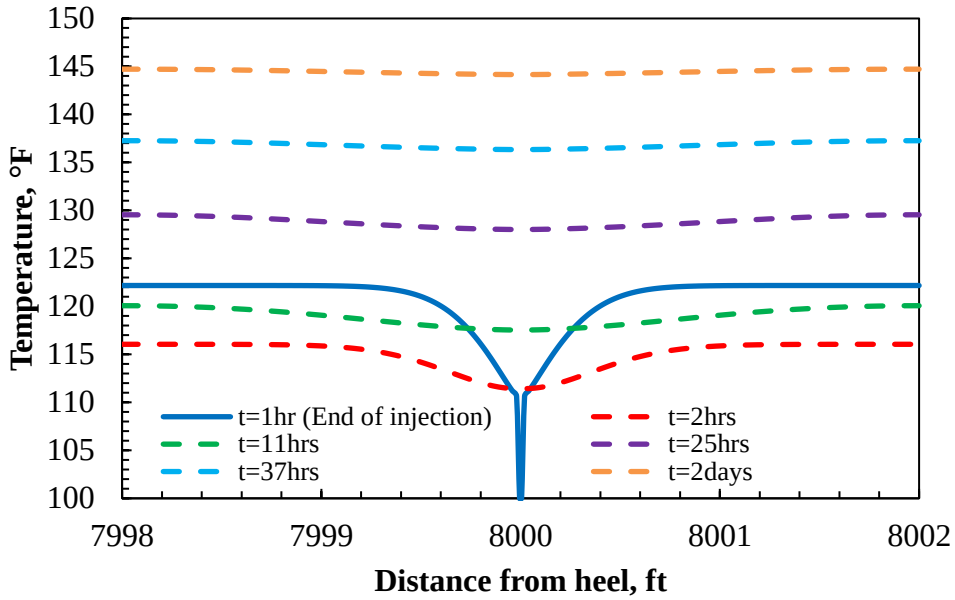

Fig. 5.20 Casing temperature profile of the single fracture system

Similarly, for multistage fracturing treatment with multiple clusters per stage, the casing temperature profile are presented. In order to investigate the casing temperature sensitivity to the injection rate, leak-off coefficient, and reservoir thermal properties, single stage with multiple identical fractures are studied to avoid complication. For multistage fracturing treatment, zonal isolation is implemented for plug and perf completion method. Casing temperature of multistage with single fracture and multistage with multi-fractures per stage are also presented for uniform and non-uniform injection fluid distribution.

5.3.1 Single Stage with Multiple Fractures

In this chapter, casing temperature profile along the wellbore are presented for several case studies. From previous discussion, we know that the injection rate is a critical

parameter for simulated temperature behavior. However, it is essential to know how much the injection rate can affect measured casing temperature profile. Thus, simulated casing temperature at various injection rates are plotted and compared.

Figure 5.21 shows the casing temperature profiles over time for injection rates of 40 bpm, 60 bpm, and 90 bpm. As mentioned before, there are five fractures, propagates simultaneously in one stage with a fracture space of 40 ft. **Table 5.6** lists the injection rates used and corresponding fracture half-length for each case. **Fig. 5.21** shows the temperature measured outside of casing as a function of time at different injection rates (**Figs. 5.21a**, **5.21b** and **5.21c**), and the comparison for these injection rates after shut-in for one day is shown in **Fig. 5.21d**. **Table 5.6** lists the simulated casing temperature results after shut-in for one day. With higher injection rate, more cold fluid enters the fracture during injection, resulting in a much slower recovery on temperature during warm back after shut-in. The casing temperature at fracture locations has 20 °F difference when the injection rate increased from 40 bpm to 90 bpm.

Table 5.6 Fracture half-length and simulated temperature (at 1 day after shut-in) for 5 identical fractures

Injection rate, bpm	Fracture half-length, ft	T at fracture locations after shut-in, °F
40	234	151.7
60	352	138.8
90	528	129.6

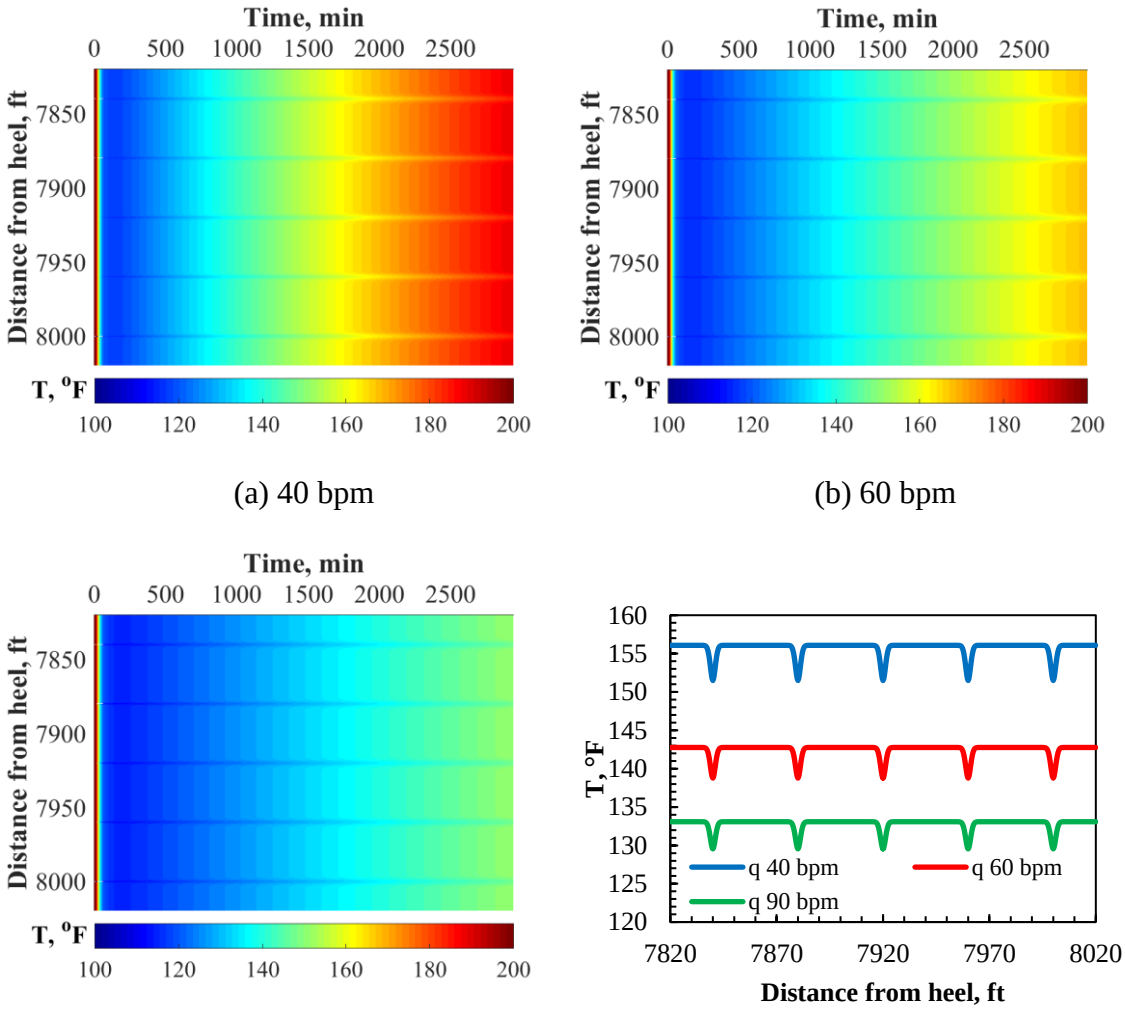

Fig. 5.21 Simulated casing temperature profiles over time of single-stage with 5 identical fractures for different injection rates and casing temperature profile comparison at one day after shut-in (d)

From the above simulated temperature profiles over time, one can clearly see lower temperature response at the fracture location during injection and shut-in. The transient temperature change along the wellbore starts from reservoir initial geothermal temperature as the initial condition before injection. Once the injection starts, casing is cooled down

by the injection fluid quickly due to relatively high casing thermal conductivity with relatively low casing heat capacity. Similarly, after shut-in the well, casing begins to be warmed up by the reservoir. For higher injection rate, the cooling temperature front travels faster to the reservoir and the warm back behavior is slower. We also found that up to two days of shut-in, the casing temperature still has a large difference compare to the initial reservoir geothermal temperature. As we expected, the temperature difference is larger when we have a higher injection rate.

As presented before, leak-off amount may varies under different circumstances, and leak-off coefficient plays an important role of fracture propagation and temperature behavior. The comparison of simulated casing temperature profile using multiple leak-off coefficients is shown in **Fig. 5.22**. We see that with higher leak-off coefficient, the casing temperature becomes lower due to the more cold fluid-loss amount near wellbore. The cooling temperature front has more dispersion near wellbore. We can also conclude that measured casing temperature may tell us the existence of natural fractures when combined with other information of fracture diagnostics.

Table 5.7 Leak-off coefficients of case study

Leak-off coefficient, C_{lk}, ft/s$^{1/2}$	
Base case	0.0001
2 times	0.0002
4 times	0.0004

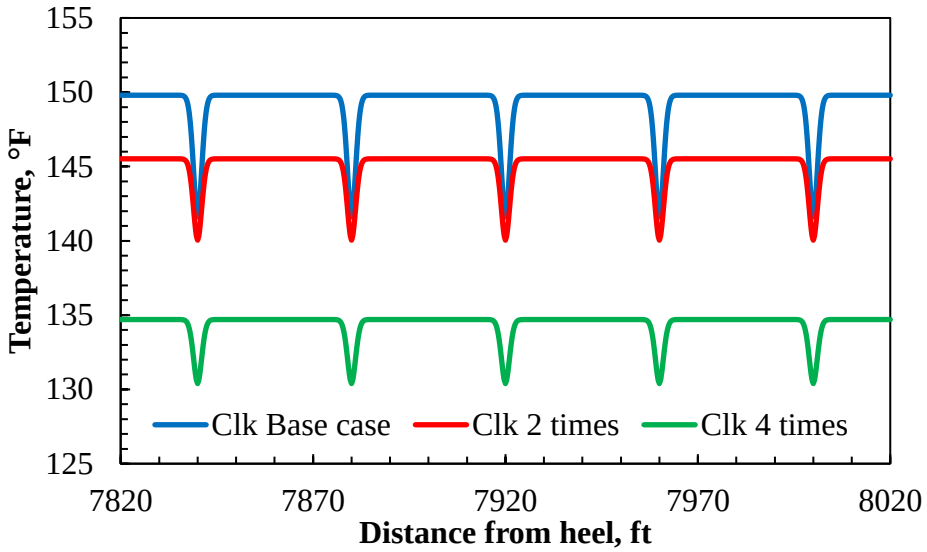

Fig. 5.22 Casing temperature comparison for various leak-off coefficients at 20 hours after shut-in

Casing temperature is also sensitive to the thermal properties of reservoir, and fracturing fluid. The thermal properties of fracturing fluid, casing and cement can be measured in the laboratory. However, the reservoir thermal conductivity for different type of formations may varies and hard to be determined. In this study, simulated casing temperature distribution is investigated for different reservoir rock thermal conductivities in a single-stage with 5 identical fractures at 40 bpm per stage (**Fig. 5.23**).

Temperature profiles over time are plotted using base case reservoir rock thermal conductivity, 2 times higher, and 4 times higher than the original value of the base case are compared here.

Table 5.8 Reservoir rock thermal conductivities of case study

Reservoir rock thermal conductivity, K_r	
Base case	0.000257 Btu/(ft-s-°F)
2 times	0.000514 Btu/(ft-s-°F)
4 times	0.001028 Btu/(ft-s-°F)

From **Fig. 5.23**, we see that the casing temperature is increasing much quicker during shut-in period when we have higher reservoir rock thermal conductivity. Temperature profile details of **Fig. 5.23a**, **5.23b**, and **5.23c** at one day after shut-in is compared in **Fig. 5.23d**. One can read the actual casing temperature difference from the following figure when using various reservoir rock thermal conductivities. The temperature increases about 30 °F after one day shut-in when we increase the reservoir rock thermal conductivity for 2 times. Although the temperature difference is getting smaller when we increase the reservoir rock thermal conductivity from 2 times to 4 times.

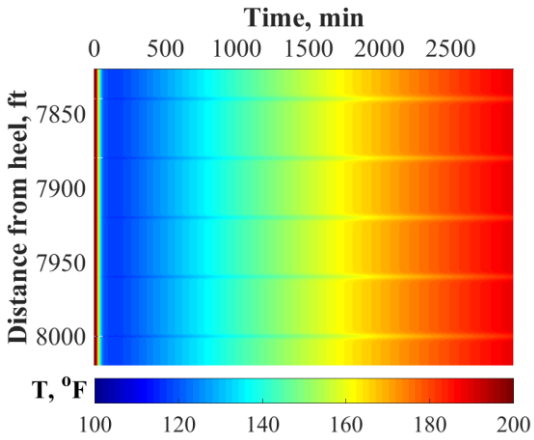

(a) $K_r = 0.000257\ Btu/(ft - s - °F)$

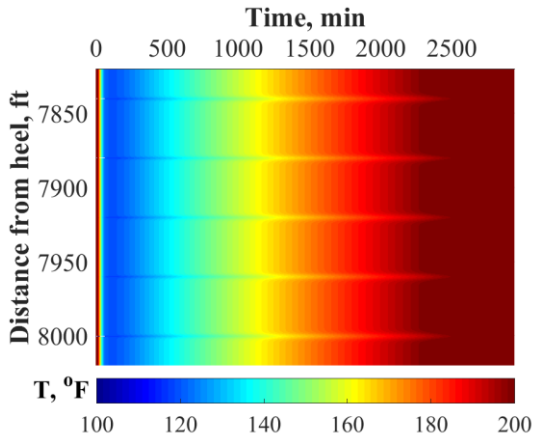

(b) 2 times K_r

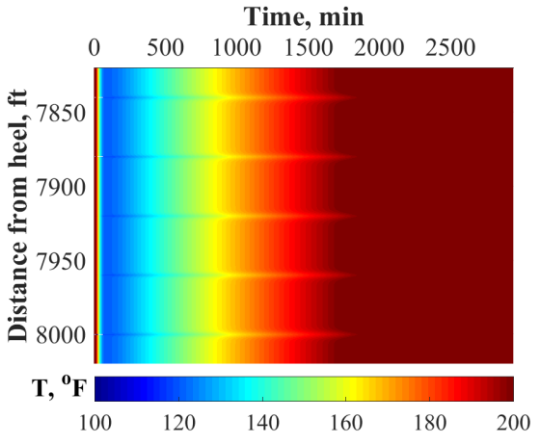

(c) 4 times K_r

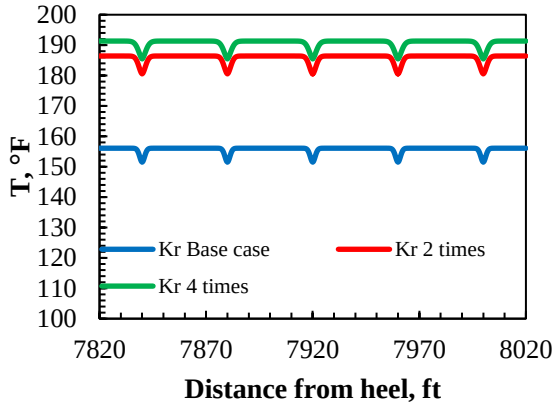

(d) Temperature comparison at shut-in 1 day

Fig. 5.23 Simulated casing temperature profiles over time of single-stage with 5 identical fractures for various reservoir rock thermal conductivities and casing temperature profile comparison at one day after shut-in (d)

5.3.2 Multistage Treatments with Single Fracture per Stage

For multistage fracturing treatment, zonal isolation is implemented. With plug and perf completion, the well is shut-in between stages to isolate the stage that already fractured, and prepare for injection of the following stage. A hypothetical case is studied

with sequential treatment schedule as injection one hour for each stage, followed by five hours shut-in. The stage space is 40 ft. The schematic of this five stages treatment is shown in **Fig. 5.24**. Simulated casing temperature profiles over time of identical and non-identical fracture distributions are presented, and 5 stages with single fracture per stage is considered to avoid complication.

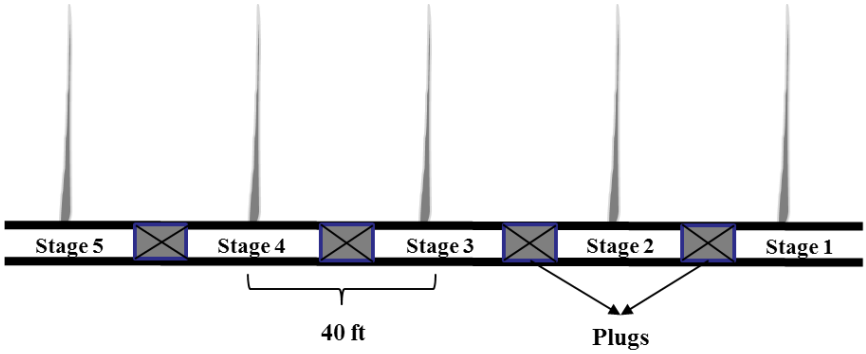

Fig. 5.24 Schematic of 5 stages treatments with single fracture per stage (Li and Zhu, 2016)

For identical fracture per stage, wellbore and casing temperature profiles over time are plotted in **Figs. 5.25** and **5.26** respectively. The side view in **Figs. 5.25b** and **5.26b** shows more details of the casing temperature transition from the initial reservoir geothermal temperature and changes between stages. **Fig. 5.27** illustrates that during injection, the well shows injection fluid temperature as long as we keep injecting cold fluid to propagate fractures. The temperature at fracture locations is the lowest because of no fluid flow during shut-in, as well as there is still heat flux from the injection fluid inside fractures. With good isolation, the distinct temperature changed from one stage to another can be identified.

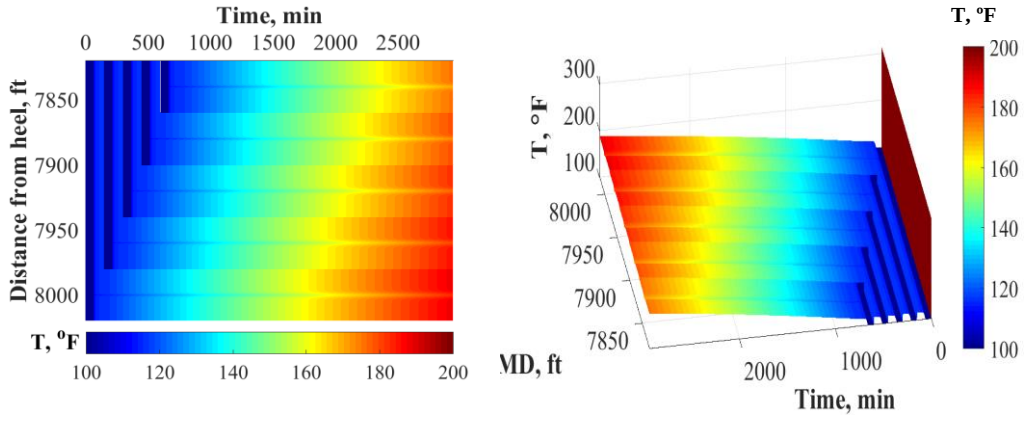

(a) Top view (b) Side view

Fig. 5.25 Simulated wellbore temperature profile of 5 stages with identical fractures

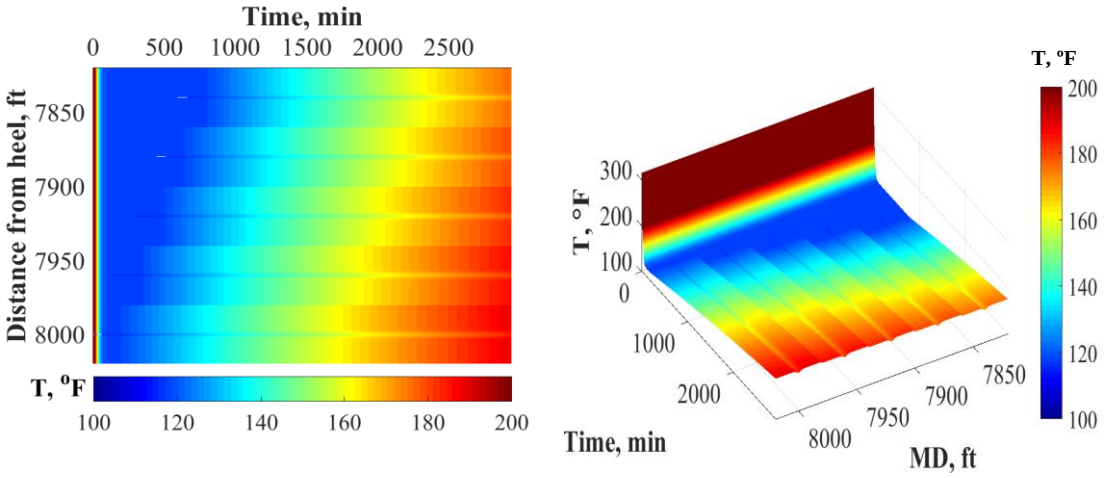

(a) Top view (b) Side view

Fig. 5.26 Simulated casing temperature profile of 5 stages with identical fractures

From **Figs. 5.25** and **5.26**, we see a time delay on the temperature response for identical fracture per stage due to shut-in between stages. For effective zonal isolation, we observe stair-step temperature distribution between stages. However, in general, the

fracture between stages is not perfectly identical even if the same treatment schedule is designed. Moreover, this can cause more complicated temperature profiles near wellbore. For example, non-identical fractures injection rates and fracture half-length is listed in **Table 5.9**. The corresponding temperature profile outside of casing for non-identical fracture at each stage is pictured in **Figs. 5.27** and **5.28**.

Table 5.9 Injection rate and fracture half-length at each stage

Non-identical fractures at 5 stages					
Stage number	1	2	3	4	5
Injection rate, bpm	5	7	10	8	10
Fracture half-length, ft	147	205	293	235	293

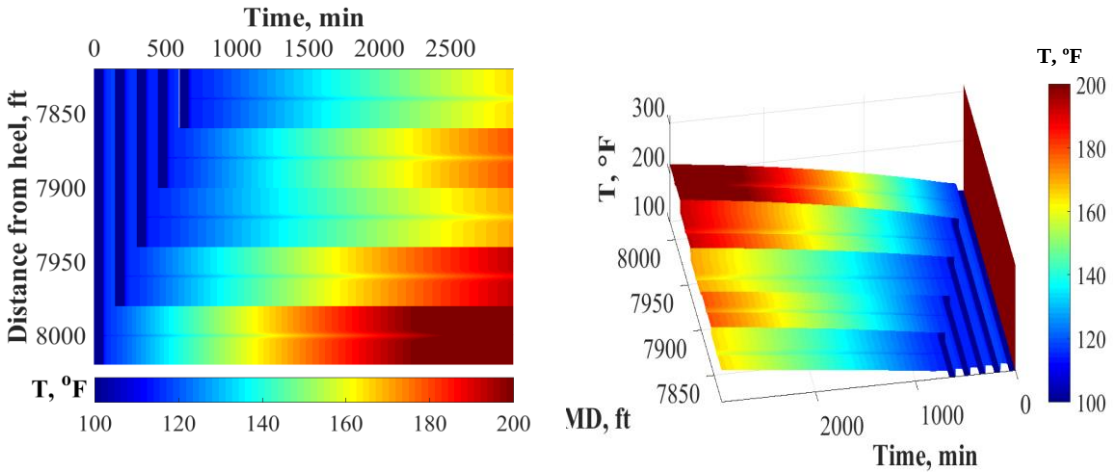

(a) Top view (b) Side view

Fig. 5.27 Simulated wellbore temperature profile over time of 5 stages with non-identical fractures

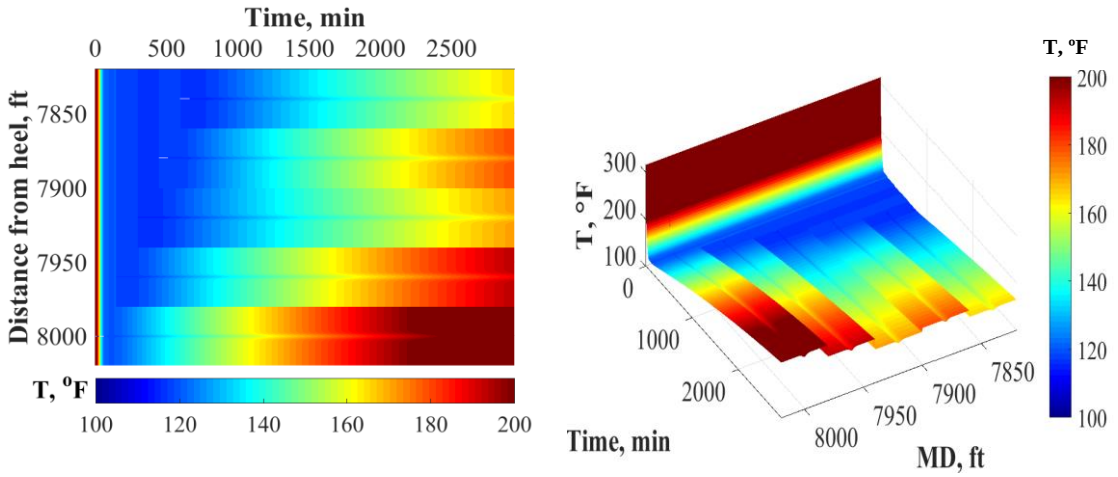

(a) Top view (b) Side view

Fig. 5.28 Simulated casing temperature profile over time of 5 stages with non-identical fractures

5.3.3 Multistage Multi-Fracture Simulation

The integrated forward model is applied to multistage multi-cluster cases. First, a synthetic case of 5 stages with 5 fractures per stage is studied. The stage length is 200 ft contains 5 evenly distributed fractures. In other words, the fracture spacing is 40 ft. For each stage, we inject fracturing fluid for one hour and shut-in for five hours between stages. The top and side view of simulated casing temperature are presented for uniform injection fluid distribution. Then, the same synthetic case is extended to non-uniform injection fluid distribution per stage and non-identical injection rates between stages. Simulated temperature profiles over time is also showed for a 10-stage treatment with 5 clusters per stage up to one week of shut-in. One can still see different casing temperature response at fracture locations compare to the rest of the well. **Fig. 5.29** shows the simulated casing temperature of 5 stages with 5 identical fractures per stage at 40 bpm.

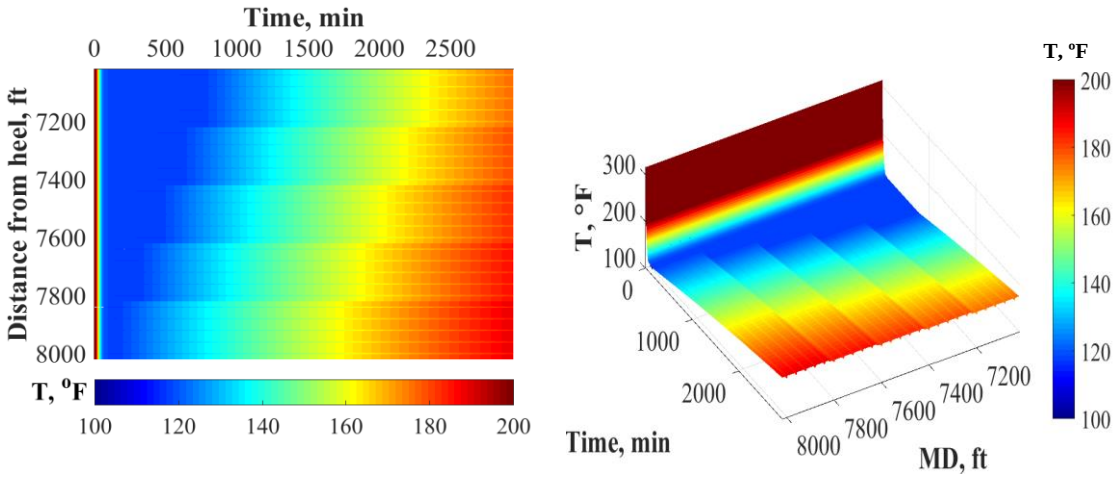

(a) Top view (b) Side view

Fig. 5.29 Simulated casing temperature profile over time of 5 stages with 5 identical fractures per stage at 40 bpm

Additional input of injection fluid distribution at each cluster in the example is listed in **Table 5.10**. For the five stages, fracture half-length is calculated from the injection rate of each stage, which assigned randomly. **Fig. 5.30** illustrates the fracture setting used in this example. **Fig. 5.31** plots the corresponding casing temperature profiles over time.

Table 5.10 Injection rate and fracture half-length at each cluster for all 5 stages

Stage 1 at 40 bpm					
Cluster number	1	2	3	4	5
Injection rate, bpm	9	9	8	7	7
Fracture half-length, ft	264	264	235	205	205
Stage 2 at 60 bpm					
Cluster number	1	2	3	4	5
Injection rate, bpm	10	11	12	12	15
Fracture half-length, ft	293	323	352	352	440
Stage 3 at 60 bpm					
Cluster number	1	2	3	4	5
Injection rate, bpm	8	10	12	15	15
Fracture half-length, ft	235	293	352	440	440
Stage 4 at 70 bpm					
Cluster number	1	2	3	4	5
Injection rate, bpm	18	15	12	10	15
Fracture half-length, ft	528	440	352	293	440
Stage 5 at 50 bpm					
Cluster number	1	2	3	4	5
Injection rate, bpm	10	12	9	10	9
Fracture half-length, ft	293	352	264	293	264

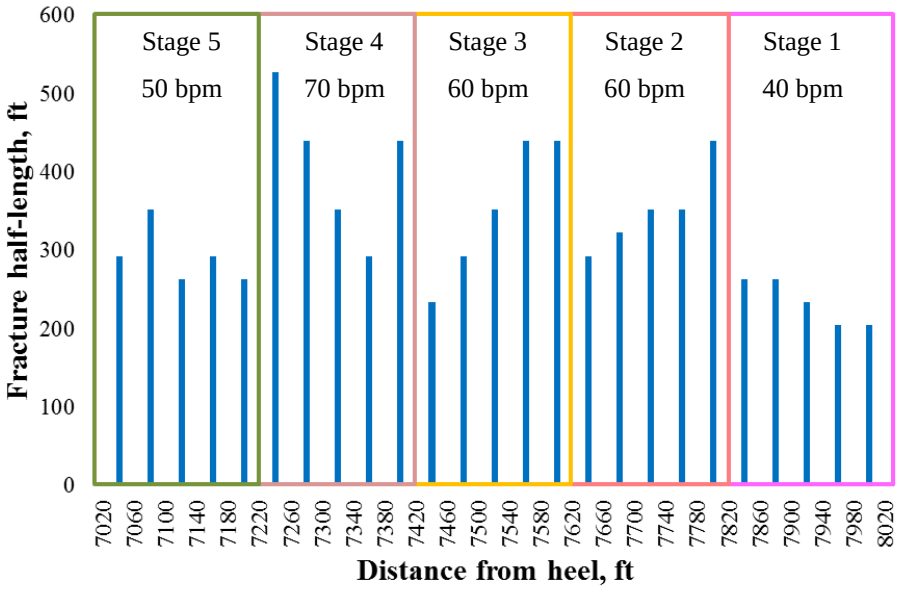

Fig. 5.30 Fracture half-length of non-uniform fluid distribution for multistage multi-cluster treatments

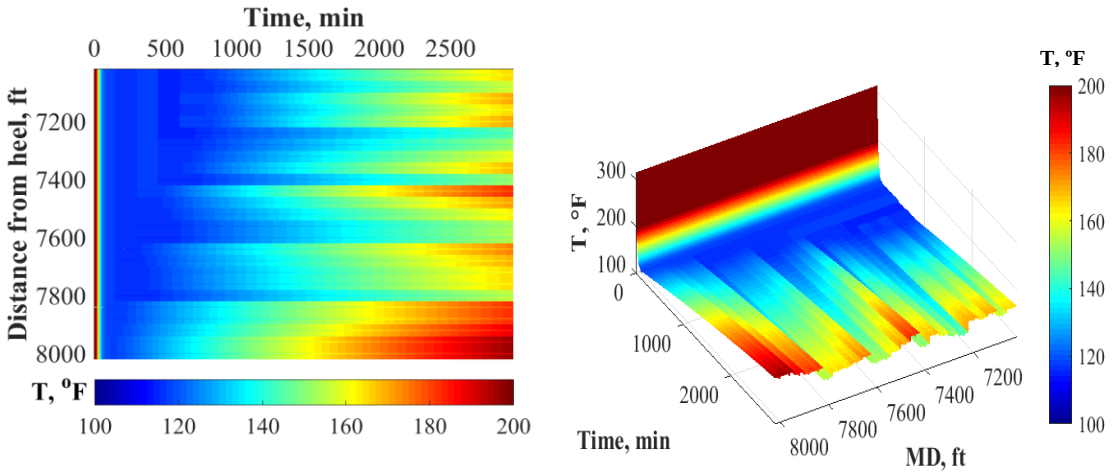

(a) Top view (b) Side view

Fig. 5.31 Simulated casing temperature profile over time of 5 stages with 5 non-identical fractures per stage

From non-uniform cases, we see casing temperature profiles are more complicated, and affected by not only the time-lag and isolation between stages, as well as fluid distribution. Therefore, to interpret of field DTS measured data using this forward model, all determine variables need to be taken into consideration during the entire fracturing treatment. Such as treatment design, injection fluid and reservoir properties, and locations of DTS cables deployment.

Figure 5.32 shows simulated casing temperature profiles for a synthetic case of 10 stages fracturing treatment with 5 clusters per stage over a week. We can tell from the figures that, after a week, we still see different temperature signals at fracture locations. This confirms that the DTS measured temperature data can be used to allocate fractures and interpret fluid distribution and reservoir properties.

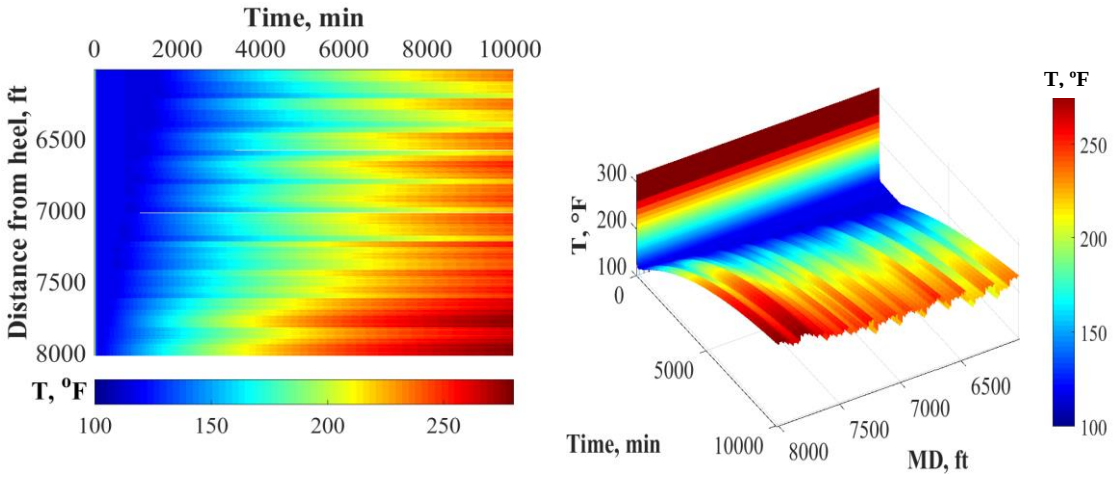

(a) Top view (b) Side view

Fig. 5.32 Simulated casing temperature profile of 10 stages with 5 non-identical fractures per stage over one week

6. CONCLUSIONS

In this study, a quantitative integrated forward model is developed to predict fracture propagation and injection fluid distribution, as well as to simulate temperature behavior in the wellbore, fracture, and reservoir during multistage hydraulic fracturing treatments in horizontal wells.

The proposed model has been described in detail in Chapter 2, and the solution and validation of the forward model were also presented in Chapter 3 and Chapter 4. From the synthetic case studies in shale reservoirs, we can conclude that:

The injection rate plays an important role on fracture growth, fluid distribution and temperature profiles in this complex flow system. By increasing the injection rate, we have longer fractures. As a result, the cooling temperature front travels faster into the reservoir and the warm back behavior in wellbore and fracture is slower. Also, for different fluid distribution, the temperature has corresponding response during treatment, especially at fracture locations. Therefore, the measured DTS data can be used to locate fractures and allocate injection volumes for perforation clusters. For higher injection rate, the delay warm back phenomena is more obvious along the wellbore away from the fracture location. For shale reservoir, the time scale to reach thermal equilibrium is on the order of weeks.

The simulated temperature profiles also depend on fluid-loss amount and distribution, which is studied by using various leak-off coefficients to model natural fractures and induced discrete fractures intercept with hydraulic fractures. The larger value

of leak-off coefficient, the more fluid-loss near wellbore happened to lower the casing temperature and reduce the fracture length. Therefore, we observed more energy dispersion near wellbore at fracture locations.

Reservoir properties also affect temperature behavior for the coupled flow system, such as rock thermal conductivity. Especially during shut-in period when heat conduction is dominant. Thus, with inversion, the measured downhole temperature data can be used to estimate reservoir properties.

It was proved that the locations of fiber optic DTS cables deployment due to different completion methods can cause different thermal couplings of the measurements by the simulated temperature results.

The model can either serve as a stand-alone tool to diagnose fracture treatment, or provide more accurate initial and boundary conditions for thermal and flow modeling of fractured well production.

Throughout this study, we know that the temperature behavior is sensitive to injection fluid distribution, the existence of natural fractures and induced discrete fractures, and fluid and reservoir properties. Therefore, the DTS measured temperature data during fracturing stimulation treatment allow for fracture diagnosis, such as, fracture location identification, fluid distribution profiling, and effectiveness of the zonal isolation detection.

The presented integrated forward model, through inclusion of shut-in periods between stages and zonal isolation for sequential multistage fracturing treatments in horizontal wells, better reflects the physical reality of a fracture operation. This more

thorough representation of the multistage hydraulic fracture stimulation gives more insight in the possible diagnosis of the operation through distributed temperature sensing.

REFERENCES

Abdulaziz, A.M. 2013. Microseismic Imaging of Hydraulically Induced-Fractures in Gas Reservoirs: A Case Study in Barnett Shale Gas Reservoir, Texas, USA. *Open Journal of Geology* **3** (5): 361-369.

Al-Hadhrami, A.K., Elliott, L., and Ingham, D.B. 2003. A New Model for Viscous Dissipation in Porous Media Across a Range of Permeability Values. *Transport in Porous Media* **53** (1): 117–122.

Alves, I.N., Alhanati, F.J.S., and Shoham, Ovadia. 1992. A Unified Model for Predicting Flowing Temperature Distribution in Wellbores and Pipelines. *SPE Production Engineering* **7** (4): 363-367.

Amini, K., Soliman, M.Y., and House, W.V. 2015. A Three-Dimensional Thermal Model for Hydraulic Fracturing. Paper SPE 174858 presented at the SPE Annual Technical Conference and Exhibition, Houston, Texas, USA, 28-30 September.

Bahonar, M., Azaiez, J., and Chen, Z. 2010. A Semi-Unsteady-State Wellbore Steam/Water Flow Model for Prediction of Sandface Conditions in Steam Injection Wells. *Journal of Canadian Petroleum Technology* **49** (9): 13-21.

Barree, R.D., Fisher, M.K., and Woodroof, R.A. 2002. A Practical Guide to Hydraulic Fracture Diagnostic Technologies. Paper SPE 77442 presented at the SPE Annual Technical Conference and Exhibition, San Antonio, Texas, 29 September-2 October.

Beckett, P.M. 1980. Combined Natural and Forced Convection between Parallel Vertical Walls. *SIAM J.* Appl. *Math.* **39** (2): 372–384.

Beckett, P. M., and Friend, I. E. 1984. Combined natural and forced convection between parallel walls: developing flow at high Rayleigh numbers. *International Journal of Heat and Mass* Transfer **27** (4): 611–621.

Bird, R.B., Stewart W.E. and Lightfoot, E.N. 2002. *Transport Phenomena*. New York: John Wiley and Sons.

Cipolla, C.L., and Wright, C.A. 2000. Diagnostic Techniques to Understand Hydraulic Fracturing: What? Why? and How? Paper SPE 59735 presented at the SPE/CERI Gas Technology Symposium, Calgary, Alberta, Canada, 3-5 April.

Cui, J., and Zhu, D. 2014. Diagnosis of Multiple Fracture Stimulation in Horizontal Wells by Downhole Temperature Measurements. Paper IPTC 17700 presented at the International Petroleum Technology Conference, Doha, Qatar, 20-22 January.

Duru, O.O., and Horne, R.N. 2008. Modeling Reservoir Temperature Transients, and Matching to Permanent Downhole Gauge (PDG) Date for Reservoir Parameter Estimation. Paper SPE 115791 presented at the SPE Annual Technical Conference and Exhibition, Denver, Colorado, USA, 21-24 September.

Economides, M.J., Hill, A.D., and Ehlig-Economides, C. 1994. *Petroleum Production Systems*. Upper Saddle River, New Jersey: Prentice Hall PTR.

Farouq Ali, S.M. 1981. A Comprehensive Wellbore Stream/Water Flow Model for Steam Injection and Geothermal Applications. *Society of Petroleum Engineers Journal* **21** (5): 527-534.

Geertsma, J., and Klerk, F. 1969. A Rapid Method of Predicting Width and Extent of Hydraulically Induced Fractures. *Journal of Petroleum Technology* **21** (12): 1571-1581.

Griston, S. and Willhite, G.P. 1987. Numerical Model for Evaluating Concentric Steam Injection Wells. Paper SPE 16337 presented at the SPE California Regional Meeting, Ventura, California, 8-10 April.

Hagoort, J. 2004. Ramey's Wellbore Heat Transmission Revisited. *SPE Journal* **9** (4): 465-474.

Hasan, A.R., and Kabir, C.S. 1991. Heat Transfer During Two-Phase Flow in Wellbores: Part I-Formation Temperature. Paper SPE 22866 presented at the SPE 66th Annual Technical Conference and Exhibition, Dallas, Texas, 6-9 October.

Hasan, A.R., and Kabir, C.S. 2010. Modeling Two-Phase Fluid and Heat Flows in Geothermal Wells. *Journal of Petroleum Science and Engineering* **71** (1-2): 77-86

Hoang, H., Mahadevan, J., and Lopez, H.D. 2011. Interpretation of Wellbore Temperatures Measured using Distributed Temperature Sensors during Hydraulic Fracture. Paper SPE 140442 presented at the SPE Hydraulic Fracturing Technology Conference, The Woodlands, Texas, USA, 24-26 January.

Holley, E. H., Molenaar, M. M., Fidan, E., and Banack, B. M. 2012. Interpreting Uncemented Multistage Hydraulic-Fracturing Completion Effectiveness Using Fiber-Optic DTS Injection Data. Paper SPE 153131 presented at Middle East Unconventional Gas Conference and Exhibition, Abu Dhabi, UAE, 23-25 January.

Holst, P.H., and Flock, D.L. 1966. Wellbore Behavior During Saturated Steam Injection. *Journal of Canadian Petroleum Technology* **5** (4): 184-193.

Hossain, M.M., 2001. *Reservoir Stimulation by Hydraulic Fracturing: Complexities and Remedies with Reference to Initiation and Propagation of Induced and Natural Fractures*. Ph.D. dissertation, The University of New South Wales, Sydney, Australia.

Howard, G.C., and Fast, C.R. 1957. Optimum Fluid Characteristics for Fracture Extension. *Drilling and Production Practices*. New York: API, (Appendix by E.D. Carter: Derivation of the general equation for estimating the extent of the fractured area), pp. 261-270.

Huckabee, P. 2009. Optic Fiber Distributed Temperature for Fracture Stimulation Diagnostics and Well Performance Evaluation. Paper SPE 118831 presented at the SPE Hydraulic Fracturing Technology Conference, The Woodlands, Texas, USA, 19-21 January.

Ingham, D. B., Pop, I., and Cheng, P. 1990. Combined free and forced convection in a porous medium between two vertical walls with viscous dissipation, *Transport in Porous Media* **5** (4): 381–398.

Johnson, D., Sierra, J., Kaura, J., and Gualtieri, D. 2006. Successful Flow Profiling of Gas Wells Using Distributed Temperature Sensing Data. Paper SPE 103097 presented at the SPE Annual Technical Conference and Exhibition, San Antonio, Texas, USA, 24-27 September.

Kamphuis, H., Davies, D. R. and Roodhart, L. P. 1993. A New Simulator for the Calculation of the In Situ Temperature Profile During Well Stimulation Fracturing Treatments. *Journal of Canadian Petroleum Technology* **32** (5): 38-47.

Khristianovitch, S.A., and Zheltov, Y.P. 1955. Formation of Vertical Fractures by Means of Highly Viscous Fluids. *Proceedings of the 4th World Petroleum Congress*, Rome, Italy, 2, pp. 579-586.

Lake, Larry W. 2010. *Enhanced Oil Recovery*. SPE. pp.461.

Li, X., and Zhu, D. 2016. Temperature Behavior of Multi-Stage Fracture Treatments in Horizontal Wells. Paper SPE 181876 presented at the SPE Asia Pacific Hydraulic Fracturing Conference, Beijing, China, 24-26 August.

Li, Z., and Zhu, D. 2010. Predicting Flow Profile of Horizontal Well by Downhole Pressure and Distributed Temperature Data for Waterdrive Reservoir (in English). *SPE Production & Operations* **25** (3): 296-304.

Maubeuge, F., Didek, M.P., and Beardsell, M.B. 1994a. Temperature Model for Flow in Porous Media and Wellbore. Paper presented at SPWLA Annual Logging Symposium, 19-22 June.

Maubeuge, F., Didek, M.P., Beardsell, M.B., Arquis, E., Bertrand, O., and Caltagirone, J.P. 1994b. MOTHER: A Model for Interpreting Thermometrics. Paper SPE 28588 presented at the SPE Annual Technical Conference and Exhibition, New Orleans, Louisiana, 25-28 September.

Mayerhofer, M.J., Stegent, N.A., Barth, J.O., and Ryan, K.M. 2011. Integrating Fracture Diagnostics and Engineering Data in the Marcellus Shale. Paper SPE 145463 presented at the SPE Annual Technical Conference and Exhibition, Denver, Colorado, USA, 30 October-2 November.

Meyer, B.R. 1986. Design Formulae for 2-D and 3-D Vertical Hydraulic Fractures: Model Comparison and Parametric Studies. *SPE Production Engineering* **4** (4): 423-429.

Meyer, B.R. 1989. Heat Transfer in Hydraulic Fracturing. *SPE Production Engineering* **4** (4): 423-429.

Molenaar, M.M., Fidan, E., and Hill, D.J. 2012. Real-Time Downhole Monitoring of Hydraulic Fracturing Treatments Using Fibre Optic Distributed Temperature and Acoustic Sensing. Paper SPE 152981 presented at the SPE/EAGE European Unconventional Resources Conference and Exhibition, Vienna, Austria, 20-22 March.

Nordgren, R.P. 1972. Propagation of a Vertical Hydraulic Fracture. *Society of Petroleum Engineers Journal* **12** (4): 306-314.

Ouyang, L., and Belanger, D. 2006. Flow Profiling by Distributed Temperature Sensor (DTS) System – Expectation and Reality. *SPE Production & Operations* **21** (2): 269-281.

Perkins, T.K., and Kern, L.R. 1961. Widths of Hydraulic Fractures. *Journal of Petroleum Technology* **13** (09): 937-949.

Pinzon, I.D., Davies, J.E., Mammadkhan, F., and Brown, G.A. 2007. Monitoring Production From Gravel-Packed Sand-Screen Completions on BP's Azeri Field Wells Using Permanently Installed Distributed Temperature Sensors. Paper SPE 110064 presented at the SPE Annual Technical Conference and Exhibition, Anaheim, California, 11-14 November.

Rahman, M.M., Rahman, M.K., and Rahman, S.S. 2002. Multivariate Fracture Treatment Optimization for Enhanced Gas Production From Tight Reservoirs. Paper SPE

75702 presented at the SPE Gas Technology Symposium, Calgary, Alberta, Canada, 30 April-2 May.

Ramey, H.J. 1962. Wellbore Heat Transmission (in English). *Journal of Petroleum Technology* **14** (4): 427-435.

Ribeiro, P.M., and Horne, R.N. 2013. Pressure and Temperature Transient Analysis: Hydraulic Fractured Well Application. Paper SPE 166222 presented at the SPE Annual Technical Conference and Exhibition, New Orleans, Louisiana, USA, 30 September-2 October.

Ribeiro, P.M., and Horne, R.N. 2014. Detecting Fracturing Growth Out of Zone Using Temperature Analysis. Paper SPE 170746 presented at the SPE Annual Technical Conference and Exhibition, Amsterdam, The Netherlands, 27-29 October.

Sagar, R., Doty, D.R., and Schmldt, Z. 1991. Predicting Temperature Profiles in a Flowing Well. *SPE Production Engineering* **6** (4): 441-448.

Satter, A. 1965. Heat Losses During Flow of Steam Down a Wellbore. *Journal of Petroleum Technology* **17** (7): 845-851.

Schechter, R.S. 1992. *Oil Well Stimulation*. Englewood Cliff, N.J.: Prentice Hall.

Seth, G., Reynolds, A. C., and Mahadevan, J. 2010. Numerical Model for Interpretation of Distributed-Temperature-Sensor Data During Hydraulic Fracturing. Paper SPE 135603 prepared for presentation at the 2010 SPE Annual Technical Conference and Exhibition held in Florence, Italy, 19-22 September 2010.

Settari, A., and Cleary, M.P. 1986. Development and Testing of a Pseudo-Three-Dimensional Model of Hydraulic Fracture Geometry. *SPE Production Engineering* **1** (6): 449-466.

Sierra, J., Kaura, J., Gualtieri, D., Glasbergen, G., and Sarkar, D. 2008. DTS Monitoring Data of Hydraulic Fracturing: Experiences and Lessons Learned. Paper SPE 116182 presented at the SPE Annual Technical Conference and Exhibition, Denver, Colorado, USA, 21-24 September.

Simonson, E.R., Abou-Sayed, A.S., and Clifton, R.J. 1978. Containment of Massive Hydraulic Fractures. Paper SPE 6089 presented at the SPE-IME 51st Annual Technical Conference and Exhibition, New Orleans, Louisiana, 3-6 October.

Stanojcic, M., Jaripatke, O., and Sharma, A. 2009. Pinpoint Fracturing Technologies: A Review of Successful Evolution of Multistage Fracturing in the Last Decade. Paper

SPE 130580 presented at the SPE/ICoTA Coiled Tubing and Well Intervention Conference and Exhibition, The Woodlands, Texas, USA, 31 March-1 April.

Sui, W. 2009. *Determining Multilayer Formation Properties from Transient Temperature and Pressure Measurements*. Ph.D. dissertation, Texas A&M University, College Station, Texas.

Sui, W., Zhu, D., Hill, A.D., and Ehlig-Economides C.A. 2008. Determining Multilayer Formation Properties from Transient Temperature and Pressure Measurements. Paper SPE 116270 presented at SPE Annual Technical Conference and Exhibition, Denver, Colorado, USA, 21-24 September.

Tabatabaei, M., Zhu, D. 2011. Fracture Stimulation Diagnostics in Horizontal Wells Using DTS. Paper SPE 148835 presented at the Canadian Unconventional Resources and International Petroleum Conference, Calgary, 15-17 November.

Ugueto, G.A., Ehiwario, M., Grae, A., Molenaar, M., McCoy, K., Huckabee, P., and Barree, B. 2014. Application of Integrated Advanced Diagnostics and Modeling to Improve Hydraulic Fracture Stimulation Analysis and Optimization. Paper SPE 168603 presented at Hydraulic Fracturing Technology Conference, The Woodlands, Texas, USA, 4-6 February.

Ugueto, G.A., Huckabee, P. T., and Molenaar, M.M. 2015. Challenging Assumptions About Fracture Stimulation Placement Effectiveness Using Fiber Optic Distributed Sensing Diagnostics: Diversion, Stage Isolation and Overflushing. Paper SPE 173348 presented at the SPE Hydraulic Fracturing Technology Conference, The Woodlands, Texas, USA, 3-5 February.

Valko, P., and Economides, M.J., 1995. *Hydraulic Fracturing Mechanics*. Chichester, England: John Wiley & Sons.

Warpinski, N.R., and Smith, M.B. 1989. Rock Mechanics and Fracture Geometry. *Recent Advances in Hydraulic Fracturing* (12): 57-80

Wheeler, J. A. 1969. Analytical Calculations for Heat Transfer from Fractures. Paper SPE 2494 presented at the SPE Improved Oil Recovery Symposium, Tulsa, Oklahoma, USA, 13-15 April.

Willhite, G.P. 1967. Over-all Heat Transfer Coefficients in Steam And Hot Water Injection Wells. *Journal of Petroleum Technology* **19** (5): 607-615.

Yoshida, N., Zhu, D., and Hill, A.D. 2013. Temperature Prediction Model for a Horizontal Well with Multiple Fractures in a Shale Reservoir. Paper SPE 166241 presented at the SPE Annual Technical Conference and Exhibition, New Orleans, Louisiana, USA, 30 September-2 October.

Yoshioka, K., Zhu, D., and Hill, A.D., Dawkrajai, P., and Lake, L.W. 2005. A Comprehensive Model of Temperature Behavior in a Horizontal Well. Paper SPE 95656 presented at the SPE Annual Technical Conference and Exhibition, Dallas, Texas, USA, 9-12 October.

Yoshioka, K., Zhu, D., Hill, A.D., Dawkrajai, P., and Lake, L.W. 2007. Prediction of Temperature Changes Caused by Water or Gas Entry into a Horizontal Well (in English). *SPE Production & Operations* **22** (4): 425-433.

Zhao, J., & Tso, C.P. 1993. Heat Transfer by Water Flow in Rock Fracture and the Application to Hot Dry Rock Geothermal Systems. *International Journal of Rock Mechanics and Mining Science and Geomechanics Abstracts* **30** (6): 633-641.